

**APPLICATION OF TANDEM MASS SPECTROMETRIC METHODS
BASED ON ION-MOLECULE REACTIONS FOR DRUG DEVELOPMENT
AND CHARACTERIZATION OF BORON-CENTERED RADICAL
DIANION**

by

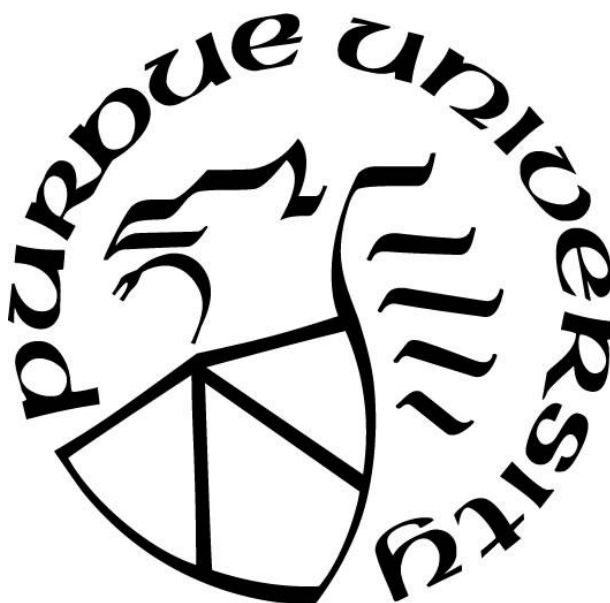
Judy Kuan-Yu Liu

A Dissertation

Submitted to the Faculty of Purdue University

In Partial Fulfillment of the Requirements for the degree of

Doctor of Philosophy



Department of Chemistry

West Lafayette, Indiana

May 2022

THE PURDUE UNIVERSITY GRADUATE SCHOOL
STATEMENT OF COMMITTEE APPROVAL

Dr. Hilkka I. Kenttämää, Chair

Department of Chemistry

Dr. Gaurav Chopra

Department of Chemistry

Dr. Mingji Dai

Department of Chemistry

Dr. Julia Laskin

Department of Chemistry

Approved by:

Dr. Christine A. Hrycyna

For my parents and husband Tom.
Thank you for the support and love they given me every step of the way.

ACKNOWLEDGMENTS

I would like to offer my immediate and sincere gratitude to my research advisor, Professor Hilkkka I. Kenttämäa. As an international student, I came to Purdue not quite knowing how my scholarly journey would take shape. At the beginning of my graduate school experience, I often felt lost in an unfamiliar environment. Professor Kenttämäa's guidance and dedication to me allowed me to slowly build the confidence necessary to become an independent research scientist. Through her constructive feedback and patience in answering my many, many questions, I was able to become the researcher I am today. Truly, this dissertation would not have become a reality without Professor Kenttämäa's wisdom, and for that I am most grateful.

In addition to Professor Kenttämäa's guidance, I would also like to acknowledge the guidance and wisdom of my other committee members: Professor Gaurav Chopra, Professor Mingji Dai, and Professor Julia Laskin. Their encouragement and support further supported my scholarly development and helped me realize my capabilities as a chemist. I am humbled that these brilliant scientists took the time to invest in my development as a chemist.

I want to offer gratitude to Professor Jonas Warneke at the Universitat Leipzig in Germany. I first met Professor Warneke when he was a post-doctoral researcher at Purdue in Professor J. Laskin's lab. His excitement, passion, and curiosity in research greatly inspired me. I consider it a great fortune to have been able to collaborate with Professor Warneke, as this experience helped me develop my own excitement, passion, and curiosity in research.

This dissertation would not have been possible without the help from the members from the Kenttämäa group, and Mark Carlsen and Dr. Hartmut Hedderich from the Jonathan Amy Facility for Chemical Instrumentation (JAFCI) at Purdue University. I would like to thank Mark Carlsen and Dr. Hartmut Hedderich for their technical advice in troubleshooting of the instruments

during my research. I would also like to thank former Kenttämaa group members, Drs Xin Ma, Edouard Niyonsaba, Jeremy Manheim, Jacob Milton, Ravikiran Yerabolu, and John Kong. They have served as great mentors who shared their advice and wisdom even after they graduated from the lab and had their own professional responsibilities. I also want to thank Dr. Kawthar Alzarieni, who was always willing to help me with my research projects.

I want to acknowledge my lab-mates: Victoria Boulos, Erlu Feng, Wanru Li, and Nancy Fu. They were always willing to let me bounce ideas and potential solutions off them. Though our brainstorming did not always reach a conclusion, we always had fun working through the problems we faced. They truly made my life in the lab enjoyable, and I will always cherish the happy memories I made with them. I also want to acknowledge the fun and happy memories that I shared with the other members of the Kenttamaa group: Yuyang Zhang, Lan Xu, Brent Modereger, Hao-Ran (Ben) Lei, Ruth Anyaeche, Jacob Guthrie, Lauren Blaudeau, Jeff Zhang, Caleb Buchman, and Caroline Rowell. I will miss being able to see them in lab and being able to take part in the various outings and get-togethers that I grew so accustomed to during my time at Purdue.

Graduate school is often a struggle of accountability and putting in the hard work each day—even when you do not want to. I want to acknowledge Kevin Wee and Anni Shi, who served as accountability partners, motivators, and fellow sufferers as we took part in long group writing sessions each evening. I was amazed by how much I could get done in two hours every night.

Finally, I want to acknowledge that none of this would have been possible without the love and support from my family. I want to acknowledge the enormous amount of love given to me by my mother, Nicole Tsai, whose sacrifices and determination allowed me to achieve things I never would have thought possible. I also want to acknowledge the deep and unfaltering love of my father, Steven Liu, who always met my accomplishments with a proud smile. I also want to

acknowledge the love and support from my husband Tom, who I met in my second year of graduate school. Tom let me know that love and family are not bound by borders. He helped inspire a belief in myself that is often necessary when graduate school becomes difficult. I also need to acknowledge my four-legged and furry companions, my cats: Grey-Grey and Pawhs. Their cuddles and cuteness always helped me wind-down for the day and appreciate the simpler joys in life.

TABLE OF CONTENTS

LIST OF TABLES	10
LIST OF FIGURES	11
ABSTRACT	16
CHAPTER 1. INTRODUCTION AND THESIS OVERVIEW	17
1.1 Introduction	17
1.2 Thesis overview	18
1.3 References	20
CHAPTER 2. THEORY, INSTRUMENTATION AND EXPERIMENTAL DETAILS FOR LINEAR QUADRUPOLE ION TRAP MASS SPECTROMETRY AND HIGH-RESOLUTION LINEAR QUADRUPOLE ION TRAP-ORBITRAP MASS SPECTROMETRY	23
2.1 Introduction	23
2.2 Ion Generation	24
2.2.1 Electrospray Ionization (ESI)	24
2.2.2 Atmospheric Pressure Chemical Ionization (APCI)	26
2.3 Linear Quadrupole Ion Trap Mass Spectrometry (LQIT MS)	28
2.3.1 Atmospheric Pressure Ionization (API) Region	29
2.3.2 Ion Optics Region	30
2.3.3 Ion Trap (Mass Analyzer) Region and Ion Detection Region	32
2.3.4 Ion Motion of the Linear Quadrupole Ion Trap	33
2.3.5 Ion Ejection for Detection	37
2.3.6 Ion Detection with Electron Multipliers	38
2.3.7 Multi-stage Tandem Mass Spectrometry	39
2.3.8 Ion Isolation	39
2.3.9 Collision-activated Dissociation	42
2.3.10 Ion/molecule Reactions	43
2.4 Orbitrap Mass Spectrometry	45
2.4.1 Ion Injection into the Orbitrap	46
2.4.2 Equations of Motion for Ions in the Orbitrap	47
2.4.3 Ion Detection	48

2.5	High-performance Liquid Chromatography/Tandem Mass Spectrometry (HPLC/MS ²)	49
2.6	References	49
CHAPTER 3. DEVELOPMENT OF A METHOD FOR THE FAST IDENTIFICATION OF THE <i>N</i> -NITROSO FUNCTIONALITY IN UNKNOWN COMPOUNDS BY USING TANDEM MASS SPECTROMETRY BASED ON DIAGNOSTIC GAS-PHASE ION-MOLECULE REACTIONS		
3.1	Introduction	55
3.2	Results and Discussion	56
3.2.1	CAD studies	57
3.2.2	Ion-molecule Reaction Studies	58
3.2.3	Ion-molecule Reactions Studies of <i>N</i> -nitroso Compounds	58
3.2.4	Ion-Molecule Reaction Studies of Compounds Containing Various Functional Groups	66
3.2.5	HPLC/MS and HPLC/MS ² experiments	73
3.3	Experimental Section	77
3.3.1	Chemicals	77
3.3.2	Synthesis procedure for <i>O</i> -nitroso compounds	78
3.3.3	Mass spectrometry	78
3.3.4	CAD experiments	79
3.3.5	Ion-molecule reactions	79
3.3.6	Computational Studies	80
3.3.7	HPLC/MS and HPLC/MS ² experiments	80
3.4	Conclusions	81
3.5	References	84
CHAPTER 4. GRAPH-BASED MACHINE LEARNING INTERPRETS AND PREDICTS DIAGNOSTIC ISOMER-SELECTIVE ION-MOLECULE REACTIONS IN TANDEM MASS SPECTROMETRY		
4.1	Introduction	87
4.2	Results and discussion	89
4.2.1	Choice of the machine learning model	89
4.2.2	Choice of neutral reagent and diagnostic ion-molecule reaction of interest	90

4.2.3	Development of machine learning model with 36 training data sets.....	90
4.2.4	Validation of the developed machine learning model	91
4.2.5	Interpretation of the chemical reactivity flowchart	96
4.2.6	Retraining the decision tree model on new reactions	99
4.3	Experimental	101
4.3.1	APCI MS method	101
4.3.2	Ion-molecule reaction conditions	101
4.4	Conclusions.....	109
4.5	References	110
CHAPTER 5. CHEMICAL CHARACTERIZATION OF THE BORON-CENTERED RADICAL DIANION $[B_{12}I_{11}]^{2\bullet}$ IN THE GAS PHASE.....		113
5.1	Introduction.....	113
5.2	Results and discussion	115
5.2.1	Reactions of $[B_{12}I_{11}]^{2\bullet}$ with allyl iodide	116
5.2.2	Reactions of $[HCB_{11}I_{10}]^{\bullet}$ and $[CB_{11}I_{11}]^{\bullet}$ with O_2 and allyl iodide	117
5.2.3	Reactions of $[B_{12}I_{11}]^{2\bullet}$ and $[HCB_{11}I_{10}]^{\bullet}$ with di- <i>tert</i> -butyl nitroxide.....	121
5.2.4	Comparing the reactivity of $[B_{12}I_{11}]^{2\bullet}$ and $[HCB_{11}I_{10}]^{\bullet}$ towards allyl iodide.....	123
5.3	Experimental	124
5.3.1	ESI MS/MS method.....	124
5.3.2	Ion molecule reactions with O_2	125
5.3.3	Ion-molecule reaction with allyl iodide	125
5.3.4	Computational studies	126
5.4	Conclusion	126
5.5	References	127
LIST OF PUBLICATIONS		129

LIST OF TABLES

Table 3.1 Product Ions (with Their Branching Ratios ^a) Observed after Short Reaction Times (30 – 1000 ms) of Protonated <i>N</i> -Nitrosamines with MOP (PA= 214 kcal/mol ^b). The structure of the product ion, [M + H + MOP - CH ₃ C(OH)=CH ₂] ⁺ , shown below was identified by using quantum chemical calculations (discussed later)	60
Table 3.2 Product Ions (with Their Branching Ratios) Observed After Short Reaction Times (30 – 1000 ms) of Protonated Analytes with Various Functional Groups with MOP (PA = 214 kcal/mol ^a)	68
Table 4.1. The probability for assignment of a correct reaction for all decision tree models	94

LIST OF FIGURES

Figure 2.1 Illustration of the generation of gas-phase ions upon (+) ESI.....	25
Figure 2.2 Illustration of the generation of gas-phase ions upon (+) APCI.....	28
Figure 2.3 Illustration of three regions of the LQIT: API region, ion optics region and the linear quadrupole ion trap and detector region.	29
Figure 2.4 Illustration of the API region: ion source max box equipped with an APCI source, sweep cone, ion transfer capillary, tube lens, and skimmer lens.	30
Figure 2.5 Schematic of the different regions and their operational pressures. A decreasing DC potential gradient was applied to the lens and multipoles within the ion optics region to facilitate axial ion transmission. The evacuation rates of the pumps are shown.	31
Figure 2.6 Illustration of the linear quadrupole ion trap.	32
Figure 2.7 The Mathieu stability diagram describing ion motion within the ion trap. Ions are represented as different colored circles with the color and size reflecting the m/z -value of the ion. If an ion has a and q parameters inside the stable region, the ion is trapped within the ion trap. If an ion has a and q parameters outside the stable region, the ion motion becomes unstable and the ion is ejected out of the ion trap.	35
Figure 2.8 A schematic of the different sections of the linear quadrupole ion trap with the DC voltages applied to each section. This resulted in the generation of a potential energy well in the z-direction that trapped ions in the z-direction. The colored circles with charges represent ions trapped in the potential energy well. The colored circles with no charges represent helium atoms.	37
Figure 2.9 Illustration of an ion detection system. Each system consisted of a conversion dynode and an electron multiplier.	39
Figure 2.10 Illustration of ion isolation in the ion trap via the Mathieu stability diagram. A) Ions whose a and q parameters reside in the stable region of the Mathieu stability diagram and that therefore have stable motions in the ion trap. B) Ions with the smallest m/z -values have been ejected from the ion trap by ramping up the RF voltage (increasing the ions q-value) until the q-value of the ion of interest reaches 0.830. C) A broadband RF excitation waveform applied to the x-electrodes caused the ejection of all remaining ions except for the ion of interest by changing their a and q values.	41
Figure 2.11 Illustration of the CAD process via the Mathieu stability diagram. A) The RF amplitude is decreased until the isolated ion (green circle) reaches a pre-set low q-value (typically 0.25). B) Tickle voltage is applied to the x-rods to increase the kinetic energy of the isolated ion (green circle). Part of the kinetic energy of the ion is converted into internal energy upon collisions with the helium buffer gas, which leads fragmentation (shown as yellow, blue, gray, and red circles).	43

Figure 2.12 A schematic of the external reagent mixing manifold for the introduction of reagents into the ion trap.	44
Figure 2.13 Schematic of the Brauman double-well potential energy surface.	45
Figure 2.14 Schematic of a LQIT coupled to a high-resolution orbitrap mass analyzer.	46
Figure 2.15 Cutaway view of the orbitrap mass analyzer.....	47
Figure 3.1 (a) CAD MS ² spectrum (collision energy 20 arbitrary units) of protonated <i>N</i> -nitrosomethyl- <i>N</i> -butylamine, indicating the loss of 1-butene. (b) CAD MS ² spectrum (collision energy 20 arbitrary units) of protonated <i>N</i> -methyl- <i>N</i> -nitrosoaniline, indicating the loss of a NO radical.....	57
Figure 3.2 (a) MS ² spectrum measured after 300 ms reactions of protonated <i>N</i> -nitrosopyrrolidine (<i>m/z</i> 101) with MOP. The observed product ions are a stable adduct, [M + H + MOP] ⁺ (<i>m/z</i> 173), a diagnostic product ion that is formed upon fragmentation of the adduct via elimination of propen-2-ol, [M + H + MOP - MW 58 Da] ⁺ (<i>m/z</i> 115), and a proton transfer product, [MOP + H] ⁺ (<i>m/z</i> 73). (b) CAD MS ³ spectrum (collision energy 10 arbitrary units) of the [M + H + MOP] ⁺ product ion (<i>m/z</i> 173).	59
Figure 3.3 Potential energy surface calculated at the M06-2X/6-311++G-(d,p) level of theory for the formation of the ions [M + H + MOP] ⁺ and [M + H + MOP - CH ₃ C(=CH ₂)OH] ⁺ upon reactions of protonated <i>N</i> -nitrosopyrrolidine with MOP provided by Erlu Feng.	64
Figure 3.4 (a) MS ² spectrum measured after 300 ms reactions of protonated <i>N</i> -nitrosornicotine with MOP, indicating the formation of an addition product [M + H + MOP] ⁺ (b) CAD MS ³ spectrum (collision energy 10 arbitrary units) of [M + H + MOP] ⁺ (<i>m/z</i> 250), indicating the regeneration of [M + H] ⁺ (<i>m/z</i> 178) (c) CAD MS ⁴ spectrum (collision energy 10 arbitrary units) of [M + H] ⁺ (<i>m/z</i> 178), indicating the diagnostic dissociation reaction via the loss of a NO radical.	66
Figure 3.5 CAD MS ² spectrum (collision energy 20 arbitrary units) of protonated 2-(pyridin-3-yl)ethyl nitrite, indicating the loss of NO radical loss.	70
Figure 3.6 Structures of the synthesized <i>O</i> -nitroso compounds, pyridine-3-ylmethyl nitrite and 2-(pyridin-3-yl)ethyl nitrite. The calculated PA (in kcal/mol) of the nitrogen atoms on the pyridine moiety of each compound is labeled in red. The PA (in kcal/mol) of the oxygen atom on the <i>O</i> -nitroso-moiety of each compound is labeled in black. PAs were calculated at the B3LYP/6-31++G(d,p) level of theory.	70
Figure 3.7 (a) MS ² spectrum measured after 1000 ms reactions of protonated 2-(pyridin-3-yl)ethyl nitrite with MOP, indicating the formation of an addition product [M + H + MOP] ⁺ (b) CAD MS ³ spectrum (collision energy 10 arbitrary units) of [M + H + MOP] ⁺ (<i>m/z</i> 239), indicating the regeneration of [M + H] ⁺ (<i>m/z</i> 167) (c) CAD MS ⁴ spectrum (collision energy 20 arbitrary units) of [M + H] ⁺ (<i>m/z</i> 167), indicating the diagnostic dissociation reaction via a loss of a NO radical and a loss of a HN=O moiety.....	72
Figure 3.8 Potential energy surfaces calculated at the M06-2X/6-311++G(d,p) level of theory for CAD of the protonated 3-((nitrosooxy)methyl)pyridine generated upon reactions of protonated pyridine-3-carboxaldehyde.	73

Figure 3.9 (a) HPLC/(+)APCI MS extracted ion chromatogram where the major peaks correspond to the five monitored protonated *N*-nitrosamines in the equal concentration 1 ppm mixture. NDMA: *N*-nitrosodimethylamine; NBMA: *N*-nitroso-*N*-methyl-4-aminobutyric; NDEA: *N*-nitrosodiethylamine; EIPNA: *N*-nitrosoethylisopropylamine; DIPNA: *N*-nitrosodiisopropylamine (b) MS² spectrum measured for protonated EIPNA (M) after reactions with MOP for 300 ms, indicating the formation of the diagnostic product ion [M + H + MOP - CH₃C(OH)=CH₂]⁺. EIPNA eluted at 12.2–13.2 min. 75

Figure 3.10 (a) HPLC/(+)APCI MS extracted ion chromatogram of protonated EIPNA at the limit of detection concentration (0.01 ppm). The chromatogram shows the analyte peak at 12.97 min. (b) Extracted ion HPLC chromatogram for the diagnostic ion-molecule reaction product ion of *m/z* 131 (generated in an MS/MS experiment) measured for EIPNA at the limit of detection concentration (0.005 ppm). The chromatogram shows the analyte peak at 12.20 min. (c) MS² spectrum measured for protonated EIPNA (M; concentration: 0.005 ppm) after reactions with MOP for 300 ms, indicating the formation of the diagnostic product ion [M + H + MOP - CH₃C(OH)=CH₂]⁺. The limit of detection measurement was performed three times. 76

Figure 3.11 Decision tree for the identification of the *N*-nitroso functionality in protonated analytes based on ion-molecule reactions with MOP and CAD experiments. 83

Figure 4.1 Chemist-made decision tree for the classification of functional groups in protonated analytes by using reactions with MOP. 92

Figure 4.2 Chemical reactivity flowchart. (a) Analytes that undergo diagnostic reaction (DR) or that do not (ND). (b) Compounds identified as having a specific functional group feature (left), such as a sulfonyl with at least one aliphatic carbon atom bound to it (right). No structure is shown when the feature (sulfonyl) is absent in a molecule that does not form a DP. (c) Flowchart for decision making based on the presence or absence of the feature (sulfonyl). (d) The decision tree model trained on a diagnostic product branching ratio cutoff of 70%. The model classifies analytes as reactive or unreactive towards MOP based on their functional groups determined by the Morgan algorithm with a radius of 1 atom. 97

Figure 4.3 The decision tree model obtained by retraining the first model by using the 70% cutoff and all 49 reactions (original 36 and new 13 test reactions). This model is similar to the one obtained via a training set of 36 reactions but has an additional check for a nitro group which was not included in the original model. The lack of any major changes from the model shown in Figure 4.2 indicates that the final model is robust and is able to incorporate new functional groups. .. 100

Figure 4.4 MS/MS spectrum measured after 500 ms reaction of protonated diisobutyl sulfoxide with MOP, indicating the formation of a diagnostic addition product (M+HMOP). 102

Figure 4.5 MS/MS spectrum measured after 3,000 ms reaction of protonated sulfonyl dimidazole with MOP, indicating the formation of a diagnostic addition product. 103

Figure 4.6 MS/MS spectrum measured after 10,000 ms reaction of protonated picoline *N*-oxide with MOP, indicating the formation of a diagnostic addition product. No proton transfer product was observed. 103

Figure 4.7 MS/MS spectrum measured after 3000 ms reaction of protonated ricobendazole with MOP, indicating the formation of a diagnostic addition product. No proton transfer product was observed.	104
Figure 4.8 MS/MS spectrum measured after 10,000 ms reaction of protonated 8-nitroquinolone with MOP, indicating that no diagnostic addition product was formed. No proton transfer product was formed, either.....	104
Figure 4.9 MS/MS spectrum measured after 3,000 ms reaction of protonated benzene sulfonic acid with MOP, indicating that a diagnostic addition product was not formed. Instead, a proton transfer product (MOP+H) was observed.	105
Figure 4.10 MS/MS spectrum measured after 10,000 ms reaction of protonated albendazole with MOP, indicating that a diagnostic addition product was not formed. No proton transfer product was observed, either.....	105
Figure 4.11 MS/MS spectrum measured after 3,000 ms reaction of protonated 4-nitroquinoline N-oxide with MOP. Although evidence of a diagnostic addition product is seen, the presence of a major proton transfer product indicates that this reaction is not suitable for diagnostic applications.	106
Figure 4.12 MS/MS spectrum measured after 3,000 ms reaction of protonated 3-methylbenzophenone with MOP, indicating that a diagnostic addition product was not formed. Instead, a proton transfer product was observed.....	106
Figure 4.13 MS/MS spectrum measured after 3,000 ms reaction of protonated 4-nitropyridine N-oxide with MOP, indicating that a diagnostic addition product was not formed. Instead, a proton transfer product was observed.	107
Figure 4.14 MS/MS spectrum measured after 10,000 ms reaction of protonated 3,5-diiodo-4-pyridine-1-acetic acid with MOP, indicating that a diagnostic addition product was not formed. No proton transfer product was observed, either.	107
Figure 4.15 MS/MS spectrum measured after 500 ms reaction of protonated 2-methoxybenzoic acid with MOP. Although evidence of a diagnostic addition product is seen, the presence of a major proton transfer product indicates that this reaction is not suitable for diagnostic applications.	108
Figure 4.16 MS/MS spectrum measured after 1000 ms reaction of protonated 4-methylpyridine N-oxide with MOP, indicating the formation of a diagnostic addition product. No proton transfer product was observed.....	108
Figure 5.1 (a) Single step fragmentation of $[B_{12}X_{12}]^{2-}$ (on the example of $X=I$) in which the ion loses a I^- and forms $[B_{12}I_{12}]^{2-}$. This pathway can be observable via CAD. (b) Pathway B requires the presence of a strong oxidizer to form the delocalized radical $[B_{12}I_{12}]^{\cdot-}$. ¹³ (c) Single step fragmentation of $[B_{12}I_{12}]^{2-}$ in which the ion loses a I^- and forms $[B_{12}I_{12}]^{2\cdot-}$. This pathway can be observable via CAD. Pink circles represent boron atoms. Purple circles represent iodine atoms. Blue shapes represent spin density.	115
Figure 5.2 MS/MS spectrum measured after 30 ms reaction of $[B_{12}I_{11}]^{2\cdot-}$ with allyl iodide, indicating that a C_3H_5 abstraction adduct with a m/z value of 783.5 was formed in high abundance.	

Iodine abstraction adduct with a m/z value of 826 and O₂ adduct with a m/z value of 779 was also observed in lower abundances compared to the C₃H₅ abstraction adduct. 117

Figure 5.3 (a) Generation of boron free radical binding site carborate [HCB₁₁I₁₀][•] from precursor ion para-[HCB₁₁I₁₀-C₄H₉][•]. (b) Generation of carbon free radical binding site carborate [HCB₁₁I₁₀][•] from precursor ion [I-Hg-CB₁₁I₁₁][•]. 118

Figure 5.4 (a) MS/MS spectrum measured after 30 ms reaction of [HCB₁₁I₁₀][•] with O₂, indicating that an O₂ adduct with a m/z value of 1433 was formed. (b) MS/MS spectrum measured after 30 ms reaction of [CB₁₁I₁₁][•] with O₂, indicating that an O₂ adduct with a m/z value of 1560 was formed. 119

Figure 5.5 (a) MS/MS spectrum measured after 30 ms reaction of [HCB₁₁I₁₀][•] with allyl iodide, indicating that a C₃H₅ abstraction adduct with a m/z value of 1442 was formed in high abundance. Iodine abstraction adduct with a m/z value of 1528 and O₂ adduct with a m/z value of 1433 was also observed in lower abundances compared to the C₃H₅ abstraction adduct. (b) MS/MS spectrum measured after 30 ms reaction of [CB₁₁I₁₁][•] with allyl iodide, indicating that a C₃H₅ abstraction adduct with a m/z value of 1569, iodine abstraction adduct with a m/z value of 1654 and O₂ adduct with a m/z value of 1560 were formed in similar abundances. 121

Figure 5.6 (a) MS/MS/MS spectrum measured after 10000 ms reaction of [B₁₂I₁₁]^{2•} with DTBN, indicating that a H abstraction adduct with a m/z value of 763.3 was formed in high abundance. O abstraction adduct (m/z = 771.3), O₂ adduct (m/z = 778.8), C₄H₈ adduct (m/z = 790.8), adduct followed by a loss of C₄H₈ moiety (m/z = 806.8) and adduct with an addition of C₄H₈ (m/z = 863.3) were observed in lower abundances compared to the H abstraction adduct. (b) MS/MS/MS spectrum measured after 10000 ms reaction of [HCB₁₁I₁₀][•] with DTBN, indicating that a H abstraction adduct with a m/z value of 1401.8 was formed in high abundance. O₂ adduct (m/z = 1433.8) and adduct (m/z = 1545.8), were observed in lower abundances compared to the H abstraction adduct. 122

Figure 5.7 (a) MS/MS spectrum measured after 30 ms reaction of [B₁₂I₁₁]^{2•} with allyl iodide, indicating that a C₃H₅ abstraction adduct with a m/z value of 783.5 was formed in high abundance. Iodine abstraction adduct with a m/z value of 826 and O₂ adduct with a m/z value of 779 was also observed in lower abundances compared to the C₃H₅ abstraction adduct. (b) MS/MS spectrum measured after 30 ms reaction of [HCB₁₁I₁₀][•] with allyl iodide, indicating that a C₃H₅ abstraction adduct with a m/z value of 1442, iodine abstraction adduct with a m/z value of 1528 and O₂ adduct with a m/z value of 1433 were formed in similar abundances. 124

ABSTRACT

Mass spectrometry (MS) is a powerful and versatile analytical tool that is extensively used for the identification and analysis of complex mixtures. The ability to couple MS to atmospheric pressure ionization techniques and high-performance liquid chromatography (HPLC) or gas chromatography (GC) provides a high degree of experimental flexibility. MS is based on the analysis of gas-phase ions. Gas-phase ions are manipulated within the mass spectrometer and separated for detection based on their *mass-to-charge* (m/z) ratio.

One of the most commonly used techniques for complex mixture analysis is tandem mass spectrometry (MS^n). MS^n involves the isolation of the desired ion and allowing it to undergo reactions, such as collision-activated dissociation (CAD) or ion-molecule reactions. Based on the generated product ions, structural information can be obtained for unknown analytes in complex mixtures. In addition, MS^n methods based on diagnostic gas-phase ion-molecule reactions have been demonstrated to provide a general and predictable tool to identify specific functional groups in unknown ionized analytes and to classify unknown analytes into different compound classes depending on their functionalities.

The research described in this dissertation mainly focuses on the development of tandem mass spectrometric methods based on gas-phase ion-molecule reactions and/or CAD for the identification of the *N*-nitroso functionality, which is present in some potentially mutagenic drug impurities. Furthermore, the dissertation discusses combining machine learning and MS^n experiments based on diagnostic ion-molecule reactions of 2-methoxypropene to predict reaction outcomes in a semiautomated fashion for protonated analytes containing specific functional groups. Lastly, chemical characterization and gas-phase reactivity of the boron-centered radical dianion $[B_{12}I_{11}]^{2-\bullet}$ toward some organic molecules are discussed.

CHAPTER 1. INTRODUCTION AND THESIS OVERVIEW

1.1 Introduction

Mass spectrometry (MS) is a powerful and versatile analytical method that is extensively used for chemical analysis. The origin of mass spectrometry was brought to dawn by J. J. Thomson in 1913.¹ During about a century, MS became one of the most popular analytical methods that was used to characterize complex mixtures of organic compounds in various fields, ranging from development of pharmaceuticals to petroleomics.²⁻⁸ The ability to be able to couple MS with atmospheric pressure ionization techniques and high-performance liquid chromatography (HPLC) or gas chromatography (GC) provides a high degree of experimental flexibility.^{9,10} To this day, MS continues to develop via improvements in specificity, sensitivity, speed and versatility to resolve new analytical challenges.

The fundamental steps of each MS experiment include transformation of the analyte into gas-phase ions, separation of the gas-phase ions based on their mass-to-charge ratios (m/z) and detection of the separated gas-phase ions.¹¹ Tandem mass spectrometry experiments (MS^n) are often carried out to obtain additional structural information for the analytes or study gas-phase ion reactions.¹²⁻¹⁴ Typical MS^n experiments begin with the isolation of the desired ion. The desired ion is then allowed to undergo reactions, such as collision-activated dissociation (CAD) or ion-molecule reactions.¹² After this, all product ions are detected in a mass-selective manner.

MS^n methods based on gas-phase ion-molecule reactions can be applied to address challenges such as characterization of unknown ions.¹² For example, the use of diagnostic gas-phase ion-molecule reactions has been demonstrated to provide a general and predictable tool for the identification of specific functional groups in unknown ionized analytes. These experiments involve isolation of the analyte ions of interest and allowing them to react with a specific gaseous

reagent. Based on the product ions formed, functional-group related information for the analyte ions of interest can be obtained.¹² In addition, gas-phase reactions of organic compounds with novel charged radicals generated within the mass spectrometer can be explored.¹⁵⁻¹⁶

1.2 Thesis overview

In this dissertation, the main focus is on the applications of MSⁿ methods based on ion-molecule reactions. First, the development of diagnostic gas-phase ion-molecule reactions for the identification of *N*-nitrosamines by using the linear quadrupole ion trap (LQIT) is discussed. After this, the coupling of machine learning methodology with MSⁿ methods to predict reaction outcomes for protonated analytes with 2-methoxypropene (MOP) is described. Finally, chemical characterization and gas-phase reactivity of the boron-centered radical dianion [B₁₂I₁₁]^{2•-} toward some organic compounds are discussed.

Chapter 2 reviews the underlying principles and experimental details of the mass spectrometers employed in this research, LQIT mass spectrometers and the high-resolution LQIT-orbitrap mass spectrometers. In addition, the fundamental aspects of MSⁿ techniques that were used, such as CAD and gas-phase ion-molecule reactions, are discussed. Lastly, experimental details of HPLC coupled with LQIT are covered.

Chapter 3 discusses the development of a MSⁿ method based on gas-phase ion-molecule reactions for the identification of the *N*-nitroso functionality. In this study, 2-methoxypropene (MOP) was found to react with protonated *N*-nitrosamines in a diagnostic manner via elimination of a 2-propenol molecule in a LQIT. A feasible mechanism for the formation of the diagnostic product ion, [M + H + MOP - CH₃C(OH)=CH₂]⁺, is proposed based on quantum chemical calculations. Three *N*-nitrosamine model compounds with an additional, strongly basic pyridine ring were found to generate false negative results upon reactions with MOP. These *N*-nitrosamines

can be identified through the above ion-molecule reactions followed by two CAD steps. Furthermore, protonated *O*-nitroso compounds with strongly basic groups were studied due to their structural similarities with protonated *N*-nitrosamines. The reactions of 42 protonated mono- and polyfunctional analytes containing different functional groups but not the *N*-nitroso-functionality were also explored, including carboxylic acids, hydroxylamines, sulfoxides, sulfones, amines and *N*-oxides.^{17,18} Two compounds producing false positive results, 2-methoxybenzoic acid and methyl phenyl sulfoxide, were identified. These compounds can be differentiated from *N*-nitrosoamines based on determination of their elemental compositions. With only two false positive cases observed for the 42 analytes studied, this methodology is considered robust for the identification of *N*-nitroso functionality in unknown analytes. Lastly, HPLC experiments were performed to obtain the detection limit for five FDA regulated *N*-nitrosamines utilizing the above method.

Chapter 4 discusses the combination of machine learning methodology with MSⁿ methods in order to be able to predict reaction outcomes with MOP for protonated analytes containing specific functionalities in a semiautomated fashion.¹⁹ As the number of explored diagnostic ion-molecule reactions continuously increases, interpretation of the experimental results becomes time-consuming and challenging. Here, a bootstrapped decision tree model based on machine learning was developed based on training on 36 known ion-molecule reactions with MOP. This chapter delineates the development of the machine learning decision tree model from a mass spectrometrists perspective. The diagnostic reaction of interest selected for this study is formation of an abundant addition product ion with MOP. The graph-based connectivity of analytes' functional groups was used as input to predict whether each protonated analyte will form an abundant addition product ion with MOP. Chemical reactivity flowchart was developed to facilitate the interpretation of the decisions made by the machine learning model methodology. In

addition to the 36 training data sets, prospective diagnostic product predictions were experimentally tested for 13 new analytes to validate the model.

Chapter 5 discusses chemical characterization of the unusual binding properties of the electrophilic boron-centered radical dianion $[\text{B}_{12}\text{I}_{11}]^{2-\bullet}$ by probing its gas-phase reactivity with reagents such as ally iodide and di-*tert*-butyl nitroxide in LQIT mass spectrometer. Remarkably, $[\text{B}_{12}\text{I}_{11}]^{2-\bullet}$ reacts efficiently with electron-rich neutral reagents, such as allyl iodide, that usually react rapidly with electrophilic cations.²⁰ In addition, $[\text{B}_{12}\text{I}_{11}]^{2-\bullet}$ reacts with *tert*-butyl nitroxide to predominately form a H atom abstraction product ion that is usually observed for electrophilic radicals.^{21,22} Furthermore, the reactivity of two singly charged carborate radicals, $[\text{HCB}_{11}\text{I}_{10}]^{\bullet}$ (with the radical site localized on a boron atom) and $[\text{CB}_{11}\text{I}_{11}]^{\bullet}$ (with the radical site localized on a carbon atom) were examined. Studies on reaction kinetics have shown consistently that the radical anion with the free binding site on boron has a greater reactivity than that with the free binding site on carbon. This finding indicates that the radical anions investigated here may be classified as electrophilic radicals, although they are anions.

1.3 References

- (1) Thomson, J. J. *Rays of Positive Electricity and Their Application to Chemical Analyses*; Longmans, Green and Co.: London, 1913.
- (2) Belas, F. J.; Blair, I. A. Mass Spectrometry in Pharmaceutical Analysis. *J. Liposome Res.* **2001**, *11* (4), 309–342. <https://doi.org/10.1081/LPR-100108611>.
- (3) Dettmer, K.; Aronov, P. A.; Hammock, B. D. Mass Spectrometry-Based Metabolomics. *Mass Spectrom. Rev.* **2007**, *26* (1), 51–78. <https://doi.org/10.1002/mas.20108>.
- (4) Castellino, S.; Lareau, N. M.; Groseclose, M. R. The Emergence of Imaging Mass Spectrometry in Drug Discovery and Development: Making a Difference by Driving Decision Making. *J. Mass Spectrom.* **2021**, *56* (8), e4717: 1-17. <https://doi.org/10.1002/jms.4717>.

- (5) Marshall, A. G.; Rodgers, R. P. Petroleomics: Chemistry of the Underworld. *Proc. Natl. Acad. Sci.* **2008**, *105* (47), 18090–18095. <https://doi.org/10.1073/pnas.0805069105>.
- (6) Richardson, S. D. Mass Spectrometry in Environmental Sciences. *Chem. Rev.* **2001**, *101* (2), 211–254. <https://doi.org/10.1021/cr990090u>.
- (7) Han, X.; Aslanian, A.; Yates, J. R. Mass Spectrometry for Proteomics. *Curr. Opin. Chem. Biol.* **2008**, *12* (5), 483–490. <https://doi.org/10.1016/j.cbpa.2008.07.024>.
- (8) Niyonsaba, E.; Manheim, J. M.; Yerabolu, R.; Kenttämää, H. I. Recent Advances in Petroleum Analysis by Mass Spectrometry. *Anal. Chem.* **2019**, *91* (1), 156–177. <https://doi.org/10.1021/acs.analchem.8b05258>.
- (9) Mas'tovska, K.; Lehotay, S. J. Practical Approaches to Fast Gas Chromatography–Mass Spectrometry. *J. Chrom. A.* **2003**, *1000* (1), 153–180. [https://doi.org/10.1016/s0021-9673\(03\)00448-5](https://doi.org/10.1016/s0021-9673(03)00448-5)
- (10) Habicht, S. C.; Duan, P.; Vinueza, N. R.; Fu, M.; Kenttämää, H. I. Liquid Chromatography/Tandem Mass Spectrometry Utilizing Ion-Molecule Reactions and Collision-Activated Dissociation for the Identification of N-Oxide Drug Metabolites. *J. Pharm. Biomed. Anal.* **2010**, *51* (4), 805–811. <https://doi.org/10.1016/j.jpba.2009.09.047>.
- (11) de Hoffmann, E.; Stroobant, V. *Mass Spectrometry: Principles and Applications.*, 3rd ed.; John Wiley & Sons Ltd: West Sussex, England, 2007.
- (12) Liu, J. K.; Niyonsaba, E.; Alzarini, K. Z.; Boulos, V. M.; Yerabolu, R.; Kenttämää, H. I. Determination of the Compound Class and Functional Groups in Protonated Analytes via Diagnostic Gas-phase Ion-molecule Reactions. *Mass Spectrom. Rev.* **2021**, e21727:1–27. <https://doi.org/10.1002/mas.21727>.
- (13) Ma, S.; Zhu, M. Recent Advances in Applications of Liquid Chromatography–Tandem Mass Spectrometry to the Analysis of Reactive Drug Metabolites. *Chem. Biol. Interact.* **2009**, *179* (1), 25–37. <https://doi.org/10.1016/j.cbi.2008.09.014>.
- (14) Boersema, P. J.; Mohammed, S.; Heck, A. J. R. Phosphopeptide Fragmentation and Analysis by Mass Spectrometry. *J. Mass Spectrom.* **2009**, *44* (6), 861–878. <https://doi.org/10.1002/jms.1599>.
- (15) Petzold, C. J.; Nelson, E. D.; Lardin, H. A.; Kenttämää, H. I. Charge-Site Effects on the Radical Reactivity of Distonic Ions. *J. Phys. Chem. A* **2002**, *106* (42), 9767–9775. <https://doi.org/10.1021/jp025521i>.
- (16) Heidbrink, J. L.; Amegayibor, F. S.; Kenttämää, H. I. Gas-Phase Radical–Radical Recombination Reactions of Nitroxides with Substituted Phenyl Radicals. *Int. J. Chem. Kinet.* **2004**, *36*, 216–229. <https://doi.org/10.1002/kin.10189>.

- (17) Sheng, H.; Williams, P. E.; Tang, W.; Zhang, M.; Kenttämä, H. I. Identification of the Sulfoxide Functionality in Protonated Analytes via Ion/Molecule Reactions in Linear Quadrupole Ion Trap Mass Spectrometry. *Analyst* **2014**, *139* (17), 4296–4302. <https://doi.org/10.1039/c4an00677a>.
- (18) Sheng, H.; Tang, W.; Yerabolu, R.; Kong, J. Y.; Williams, P. E.; Zhang, M.; Kenttämä, H. I. Mass Spectrometric Identification of the N-Monosubstituted N-Hydroxylamino Functionality in Protonated Analytes via Ion/Molecule Reactions in Tandem Mass Spectrometry. *Rapid Commun. Mass Spectrom.* **2015**, *29* (8), 730–734. <https://doi.org/10.1002/rcm.7154>.
- (19) Fine, J.; Kuan-Yu Liu, J.; Beck, A.; Alzarini, K. Z.; Ma, X.; Boulos, V. M.; Kenttämä, H. I.; Chopra, G. Graph-Based Machine Learning Interprets and Predicts Diagnostic Isomer-Selective Ion–Molecule Reactions in Tandem Mass Spectrometry. *Chem. Sci.* **2020**, *11* (43), 11849–11858. <https://doi.org/10.1039/D0SC02530E>.
- (20) Petzold, C. J.; Nelson, E. D.; Lardin, H. A.; Kenttämä, H. I. Charge-Site Effects on the Radical Reactivity of Distonic Ions. *J. Phys. Chem. A* **2002**, *106* (42), 9767–9775. <https://doi.org/10.1021/jp025521i>.
- (21) Heidbrink, J. L.; Amegayibor, F. S.; Kenttämä, H. I. Gas-Phase Radical–Radical Recombination Reactions of Nitroxides with Substituted Phenyl Radicals. *Int. J. Chem. Kinet.* **2004**, *36*, 216–229. <https://doi.org/10.1002/kin.10189>.
- (22) Singh, H.; Tedder, J. M. Interconversion of Carbocations, Free Radicals and Carbanions in Nitroxide Solutions. *J. Chem. Soc. Chem. Commun.* **1981**, No. 3, 70–71. <https://doi.org/10.1039/c39810000070>.

CHAPTER 2. THEORY, INSTRUMENTATION AND EXPERIMENTAL DETAILS FOR LINEAR QUADRUPOLE ION TRAP MASS SPECTROMETRY AND HIGH-RESOLUTION LINEAR QUADRUPOLE ION TRAP–ORBITRAP MASS SPECTROMETRY

2.1 Introduction

Tandem mass spectrometry is a powerful analytical technique that is used in various fields, ranging from development of pharmaceuticals to petroleomics, to characterize complex mixtures of organic compounds.^{2–8} The great advantages of tandem mass spectrometry include its specificity, high sensitivity, speed and versatility, and the capability of coupling it to chromatography, such as high-performance liquid chromatography and gas chromatography.^{9,10}

Although the instrumentation and methodologies of mass spectrometry are very diverse, the fundamental principles of every mass spectrometry experiment involve the same three general steps: 1) transformation of the analyte molecules into gas-phase ions, 2) separation of the gas-phase ions based on their mass-to-charge ratios (m/z) and 3) detection of the separated gas-phase ions.¹¹ Tandem mass spectrometry experiments (MS^n) are often carried out to obtain structural information for unknown analytes in complex mixtures or to study gas-phase ion reactions.^{12–14} Typical MS^n experiments involve at least two stages of mass analysis (MS^2). First, the desired ion is isolated. Then, it is allowed to undergo reactions, such as collision-activated dissociation (CAD) or ion-molecule reactions.¹² After this, all product ions are separated in a mass-selective manner in a mass analyzer and detected.

The instruments that were used to perform the experiments discussed in this dissertation were a linear quadrupole ion trap (LQIT) and a LQIT coupled with an orbitrap high-resolution mass analyzer (LQIT/Orbitrap).^{15–17} In some experiments, these instruments were coupled with high-

pressure liquid chromatography (HPLC). In this chapter, details of the theory and operation of different ion sources, LQIT, high resolution orbitrap mass analyzer and HPLC are discussed.

2.2 Ion Generation

Mass spectrometry is based on the analysis of gas-phase ions. The first step of a mass spectrometric experiment is evaporation and ionization of the analyte molecules to generate gas-phase ions. The two ionization techniques used in this dissertation were electrospray ionization (ESI) and atmospheric pressure chemical ionization (APCI). ESI and APCI are discussed in detail below.

2.2.1 Electrospray Ionization (ESI)

Electrospray ionization (ESI) was first introduced by Fenn et al. in 1989 when they successfully detected multiply charged protein ions upon ESI.¹⁸ ESI is a soft ionization method, which transfers analyte molecules or ions from solution into the gas phase as ions with minor or no fragmentation. This ionization method enabled protein and other biopolymer analysis by using mass spectrometry due to its capability of bringing large, thermally labile, and polar compounds or ions into the gas phase. ESI can be used to form multiply charged ions. Formation of multiply charged ion has enabled ESI to be used to analyze compounds with molecular weights greater than 100,000 Da.¹⁸ ESI can also be used to analyze small polar molecules.¹⁹ Polar solvents, such as acetonitrile, methanol, and water, are most commonly used as solvents in an ESI MS experiment.

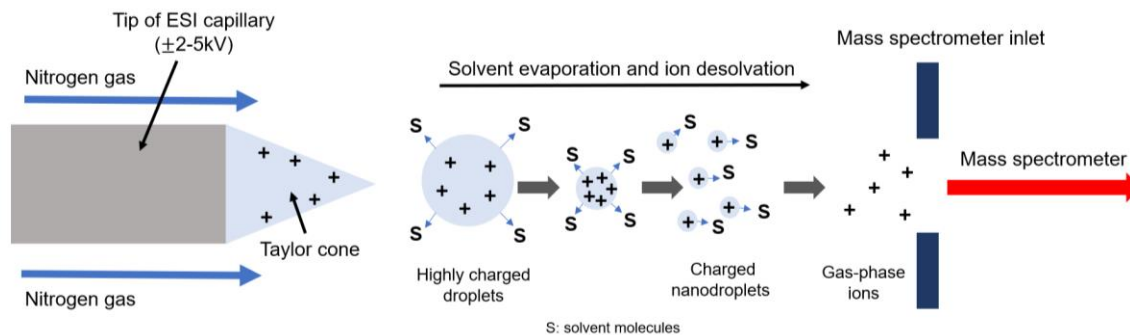


Figure 2.1 Illustration of the generation of gas-phase ions upon (+) ESI.

As shown in **Figure 2.1**, an ESI MS experiment is initiated with an analyte solution flowing through an ESI capillary to which high voltage ($\pm 2-5 \text{ kV}$) is applied.²⁰ The applied voltage generates a high electric field, which accumulates charge on the surface of the solution flowing through the tip of the ESI capillary. Charge accumulation on the solution surface induces the formation of a Taylor cone that generates a fine mist of micrometer-size charged droplets.¹¹ Nitrogen gas flowing on both sides of the ESI needle serves the purpose of nebulization and evaporation of the solvent. As the solvent molecules evaporate off the charged droplets, the electrical charge density at the surface of the droplets increases. When the electrical charge density at the surface of the droplets has increased to a critical point, also known as Rayleigh stability limit, the charged droplets burst into smaller charged droplets because the electrostatic repulsion exceeded the surface tension of the droplet. This process is repeated several times as the solvent molecules continue to evaporate from the droplets, resulting in nanometer-sized droplets.

The formation of gas-phase ions from nanometer-sized charged droplets can be explained based on three different models: ion evaporation model (IEM), charge residual model (CRM) and charge ejection model (CEM).²¹ The ion evaporation model is generally applied to explain the transformation of small singly charged ions from solution into the gas phase. In the IEM, small

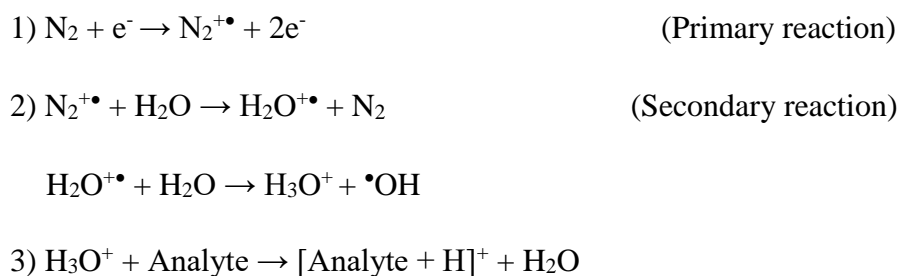
solvated ions are thought to be expelled from the droplet surface when the surface charge of the droplet is sufficiently high.²² Gas-phase ions are generated from the desorption of these small solvated ions as they travel into the mass spectrometer. CRM is used to rationalize the evaporation of large molecules, such as proteins. The CRM model assumes that the nanometer-sized charged droplets contain only one analyte molecule that is evaporated into dryness upon which the charge of the droplet is transferred to the analyte molecule to form a gas-phase ion.²³ The CRM is generally used to explain the formation multiply charged ions. CEM shares some similar elements with the ion evaporation model where analyte ions are expelled from the droplet surface. However, the CEM model is applied to unfolded proteins. The hydrophobic character of unfolded proteins makes it less favorable for them to reside in the interior of the droplet and facilitate their migration to the surface of the droplet. As the chain terminus of the unfolded protein is ejected out from the droplet surface into the gas phase, sequential ejection of the remaining protein follows.²¹

2.2.2 Atmospheric Pressure Chemical Ionization (APCI)

APCI is an ionization method that ionizes analytes via a series of gas-phase ion-molecule reactions under atmospheric pressure.^{11,24,25} The outcome greatly depends on the experimental conditions, such as vaporization temperature and choice of solvent. APCI is considered a soft ionization method but is not as soft as ESI. APCI is mostly applied for the ionization of small analyte molecules that can be non-polar or polar.²⁵ Both non-polar and polar solvents can be used in APCI depending on the solubility of the analyte.²⁶

The generation of gas-phase ions upon APCI is initiated with the sample solution (analyte dissolved in a solvent) flowing through a heated silica capillary accompanied by nebulizing gas (N₂) to create a fine mist of droplets. The evaporation of the analyte and solvent within the droplets is facilitated by the nebulizing gas and a heated ceramic tube that surrounds the tip of the silica

capillary of the APCI. Temperature of the ceramic tube is adjusted according to the volatility of the solvent used. After the analyte and solvent have been transferred into the gas-phase, a series of gas-phase ion-molecule reactions are initiated by applying high voltage (2-5 kV) on the corona discharge needle.²⁶ One possible series of ion-molecule reactions is shown in **Scheme 2.1**: 1) nebulization gas (N₂) is ionized by the corona discharge to form primary nitrogen radical cations, 2) the primary ions react with the gas-phase solvent molecules to form solvent radical cations that eventually form protonated solvent molecules, and 3) the protonated solvent molecules react with the gas-phase analyte molecules to form protonated analyte molecules.¹¹



Scheme 2.1 One possible mechanism for the generation of protonated analytes upon positive ion mode APCI with N₂ as the sheath gas and water as the solvent.

Figure 2.2 below illustrates the generation of gas-phase ions upon positive-ion mode APCI. If the solvent used contains protons, such as 50:50 water: methanol, the solvent ions tend to react with neutral solvent molecules via proton transfer to generate protonated solvent molecules (Scheme 2.1). Protonated solvent molecules react with the analyte molecules to form protonated analyte molecules.

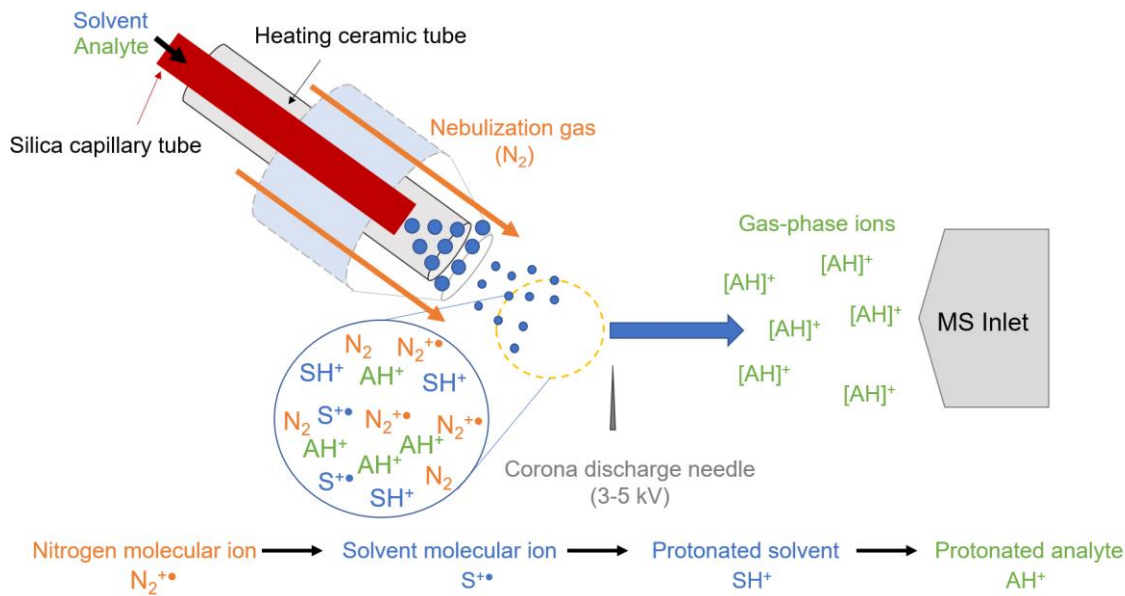


Figure 2.2 Illustration of the generation of gas-phase ions upon (+) APCI.

2.3 Linear Quadrupole Ion Trap Mass Spectrometry (LQIT MS)

The mass spectrometers utilized in this research, Thermo LQIT MS and LQIT MS coupled to an orbitrap high-resolution detector, are discussed in this chapter.^{15–17,27} The LQIT MS was composed of three differentially pumped regions as shown below with the three regions labeled as atmospheric-pressure ionization (API) region, ion optics region, and linear quadrupole ion trap and ion detection region (**Figure 2.3**). These regions are discussed in detail below.

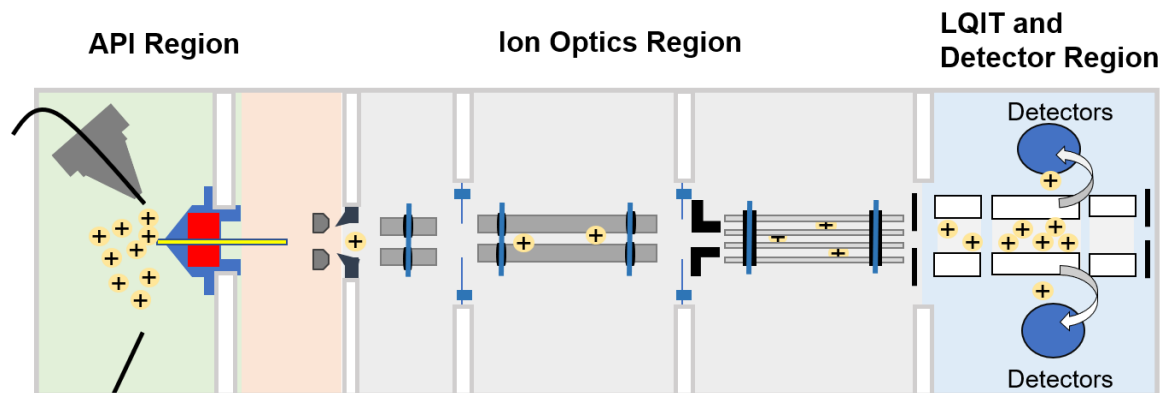


Figure 2.3 Illustration of three regions of the LQIT: API region, ion optics region and the linear quadrupole ion trap and detector region.

2.3.1 Atmospheric Pressure Ionization (API) Region

The API region consisted of the ion source max box and API stack (**Figure 2.4**). Ion source max box was operated under atmospheric pressure (~ 760 Torr) and was equipped with either an ESI or APCI source (discussed above in section 2.2), corona discharge needle and a sweep cone. The sweep cone served as a mechanical barrier to prevent large droplets from entering the MS inlet. API stack was operated at ~ 1 Torr. The low pressure of the API stack region was achieved via two mechanical pumps (Edwards E2M30) operating at an evacuation rate of 650 L/min.²⁷ The API stack was composed of an ion transfer capillary tube, tube lens and skimmer lens. Ions that were generated in the ion source were drawn into the ion transfer capillary via a pressure gradient (760 Torr to 1 Torr) and a potential gradient (ion source: 2-5 kV to API stack: 0-20 V). The typical temperature of the ion transfer capillary was 250 °C and it could be heated up to 400 °C to ensure complete desolvation of the ions before being transferred into the tube lens. A direct current (DC) voltage was applied to the tube lens to help focus the ions towards the center of the opening of the skimmer cone. This DC voltage could be adjusted to maximize the sensitivity for differently sized ions and also to filter out ions with the opposite polarity. The off-centered skimmer cone served

as a second barrier to filter out possible neutral atoms and molecules from entering the mass spectrometer.

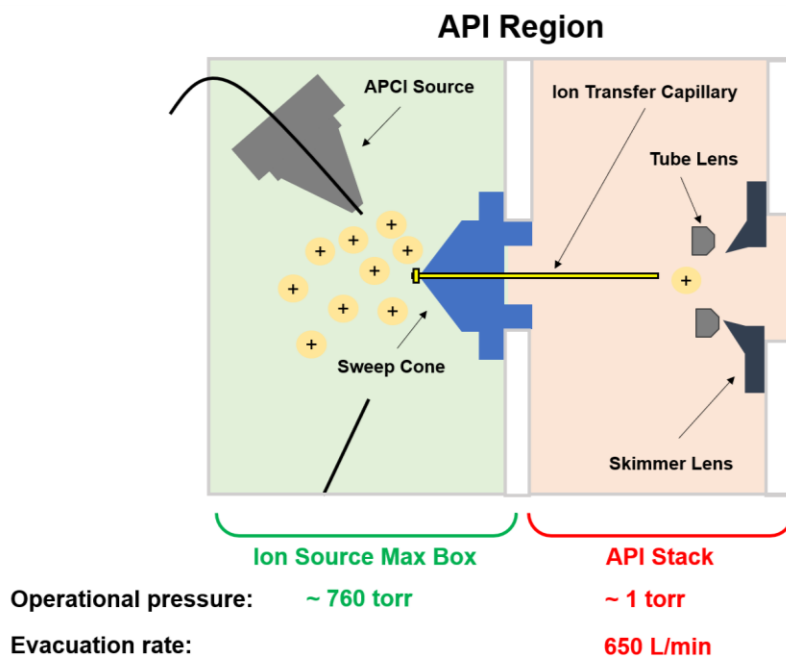


Figure 2.4 Illustration of the API region: ion source max box equipped with an APCI source, sweep cone, ion transfer capillary, tube lens, and skimmer lens.

2.3.2 Ion Optics Region

The ion optics were situated after the skimmer cone.²⁷ The main purpose of the ion optics was to focus the ions into an ion beam before entering the ion trap. The ion optics consisted of three multipoles, two quadrupoles (Q00 and Q0) and one octupole (Q1), located in areas with decreasing pressures. The two quadrupoles, Q00 and Q0, were located in areas with a pressure 0.5 Torr and 1 mTorr, respectively. The octupole, Q1, operated under the pressure of 1×10^{-5} Torr, which is also the same pressure the linear quadrupole ion trap was operated at. The different operational pressures of each ion optics region were achieved with a Leybold T220/150/15S triple-inlet turbomolecular pump. A lens was situated between each multipole to serve as a vacuum baffle.

Two different types of voltages were applied to control the trajectories of the ions when they were transmitted through the ion optics region.²⁷ A DC offset voltage was applied to both the multipole and lenses to guide the ion transmission in the axial direction (z-direction). The applied DC offset voltage was attractive based on the polarity of the ions. The decreasing DC voltage gradient shown in **Figure 2.5** facilitated the ion transmission through the ion optics region by increasing the kinetic energy of the ions. To focus the ions into the center of the multipoles within the ion optics region, a radio frequency (RF) voltage was applied to the multipoles to control the trajectories of the ions in the radial direction (x- and y-plane). The RF voltage applied to the opposing rods in the multipoles had the same amplitude and phase but voltages with the same amplitude but 180° out of phase were applied to the adjacent rods. The generated electric field caused the ions to travel in a circular manner within the multipole in the radial direction.

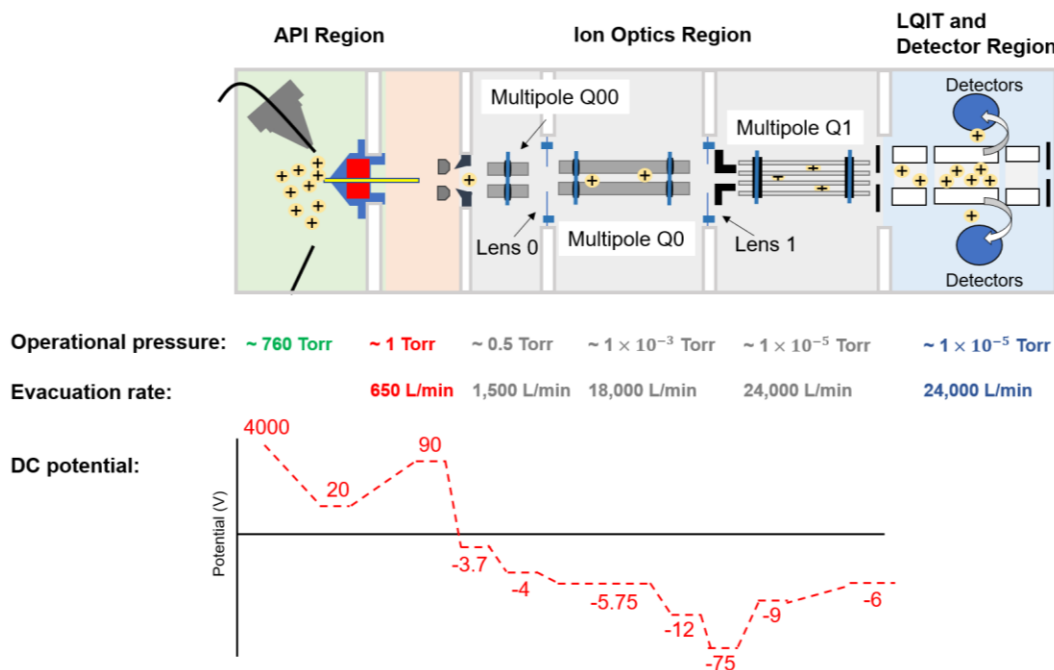


Figure 2.5 Schematic of the different regions and their operational pressures. A decreasing DC potential gradient was applied to the lens and multipoles within the ion optics region to facilitate axial ion transmission. The evacuation rates of the pumps are shown.

2.3.3 Ion Trap (Mass Analyzer) Region and Ion Detection Region

The linear quadrupole ion trap consisted of four parallel hyperbolic rods shown in **Figure 2.6**.¹⁶ The ion trap was filled with helium buffer gas at 1 mTorr and its pressure was monitored by the ion gauge. The ion gauge measurement was generally between $0.4 - 2.0 \times 10^{-5}$ Torr when conducting MS experiments. The rods were divided into front, center, and back sections. DC potentials applied to the front and back sections of the rods were greater than that applied to the center section to create a potential well for ion trapping in the axial direction. For the radial direction, an RF voltage was applied to all the four rods, with the adjacent rods having potentials with opposite phases. The two rods in the x-plane in the center section had exit slits through which the ions were ejected out of the ion trap for detection. To eject out the ions through the exit slits for detection, an additional RF potential was applied to the two rods in the x-plane. After the ions were ejected out of the ion trap, they were detected in the ion detection systems that were situated on both sides of the rods in the x-plane. The following sections will describe the scan function of the ion trap and ion detection.

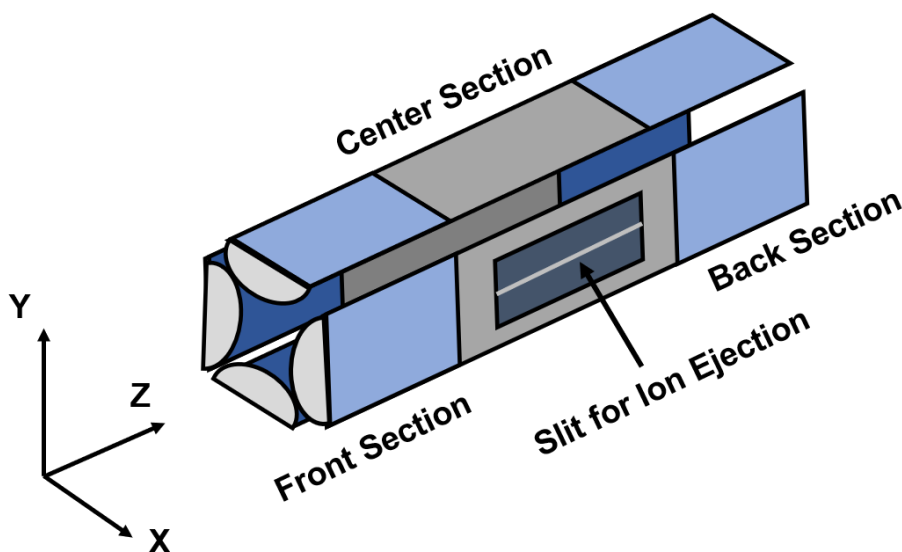


Figure 2.6 Illustration of the linear quadrupole ion trap.

2.3.4 Ion Motion of the Linear Quadrupole Ion Trap

A combination of radio frequency (RF) and direct current (DC) potentials were applied to the four parallel hyperbolic rods of the linear quadrupole ion trap to confine ions in the radial direction. To trap ions in the axial direction, only DC potentials were used. The underlying equations to describe ion motions of the LQIT are discussed in detail in the following sections.

2.3.4.1 Trapping of Ions in the Radial (xy) Plane

To confine the ions within the center sections of the rods in the linear quadrupole ion trap, a combination of RF and DC voltages were applied to the four rods of the ion trap to create a quadrupolar RF-field. The potential Φ_0 applied to the rods of the ion trap is described by Equation 2.1. The same potential amplitude but opposite phase are applied to the adjacent rods.¹⁵

$$\pm\Phi_0 = \pm(U - V\cos\Omega t) \quad \text{Equation 2.1}$$

where U is the amplitude of the DC voltage, V is the maximum amplitude of the RF voltage, Ω is the angular frequency of the RF-field and t is time. Equation 2.2 can be further used to describe the potential in the x and y directions (Φ_{xy}).

$$\Phi_{xy} = \frac{(x^2 - y^2)}{r_0^2} \Phi_0 = \frac{(x^2 - y^2)}{r_0^2} (U - V\cos\Omega t) \quad \text{Equation 2.2}$$

where r_0 is the radius of the inscribed circle of the quadruple rods.

The electric field in the x direction can be described as shown in Equation 2.3.

$$\frac{\partial\Phi(x,y,t)}{\partial x} = \frac{2x}{r_0^2} (U - V\cos\Omega t) \quad \text{Equation 2.3}$$

The electric field in the y direction can be described as shown in Equation 2.4.

$$\frac{\partial \Phi(x,y,t)}{\partial y} = \frac{2y}{r_0^2} (U - V \cos \Omega t) \quad \text{Equation 2.4}$$

The force that the ions experience in the x- and y-directions, F_x and F_y , respectively, is determined through the Newton law shown in Equations 2.5 and 2.6

$$F_x = m \frac{\partial^2 x}{\partial t^2} = -ze \frac{\partial \Phi}{\partial x} = -\frac{2zex}{r_0^2} (U - V \cos \Omega t) \quad \text{Equation 2.5}$$

$$F_y = m \frac{\partial^2 y}{\partial t^2} = -ze \frac{\partial \Phi}{\partial y} = -\frac{2zey}{r_0^2} (U - V \cos \Omega t) \quad \text{Equation 2.6}$$

where m is the mass of the ion, z is the number of charges of the ion and e is the elementary charge (1.602×10^{-19} Coulombs). <what is zex?

The ion motion in the x- and y-directions can be expressed as shown in Equations 2.7 and 2.8 which are derived from Equations 2.5 and 2.6 respectively:

$$\frac{\partial^2 x}{\partial t^2} + \frac{2zex}{mr_0^2} (U - V \cos \Omega t) \quad \text{Equation 2.7}$$

$$\frac{\partial^2 y}{\partial t^2} + \frac{2zey}{mr_0^2} (U - V \cos \Omega t) \quad \text{Equation 2.8}$$

The Mathieu equation (Equation 2.9) that describes the ion trajectory has similarities to the ion motion equations, Equations 2.7 and 2.8: you should use a instead of a everywhere for the a -parameter

$$\frac{\partial^2 u}{\partial \xi^2} + (a_u + 2q_u \cos 2\xi)u = 0 \quad \text{Equation 2.9}$$

The Mathieu equation can also be expressed as the follows:

$$\xi = \frac{\Omega t}{2} \quad \text{Equation 2.10}$$

$$a_u = a_x = (-)a_y = \frac{8zeU}{mr_0^2\Omega^2} \quad \text{Equation 2.11}$$

$$q_u = q_x = (-)q_y = \frac{4zeV}{mr_0^2\Omega^2} \quad \text{Equation 2.12}$$

wherein a_x , q_x , a_y , and q_y are known as the parameters describing the ion motion in the x- and y-directions, respectively, and a_u and q_u are known as the Mathieu stability parameters. These Mathieu stability parameters describe the stability of the ion trajectories within the ion trap. In order to trap ions within the trap, the values a_u and q_u must be within the stable region of the Mathieu stability diagram shown in **Figure 2.7**.

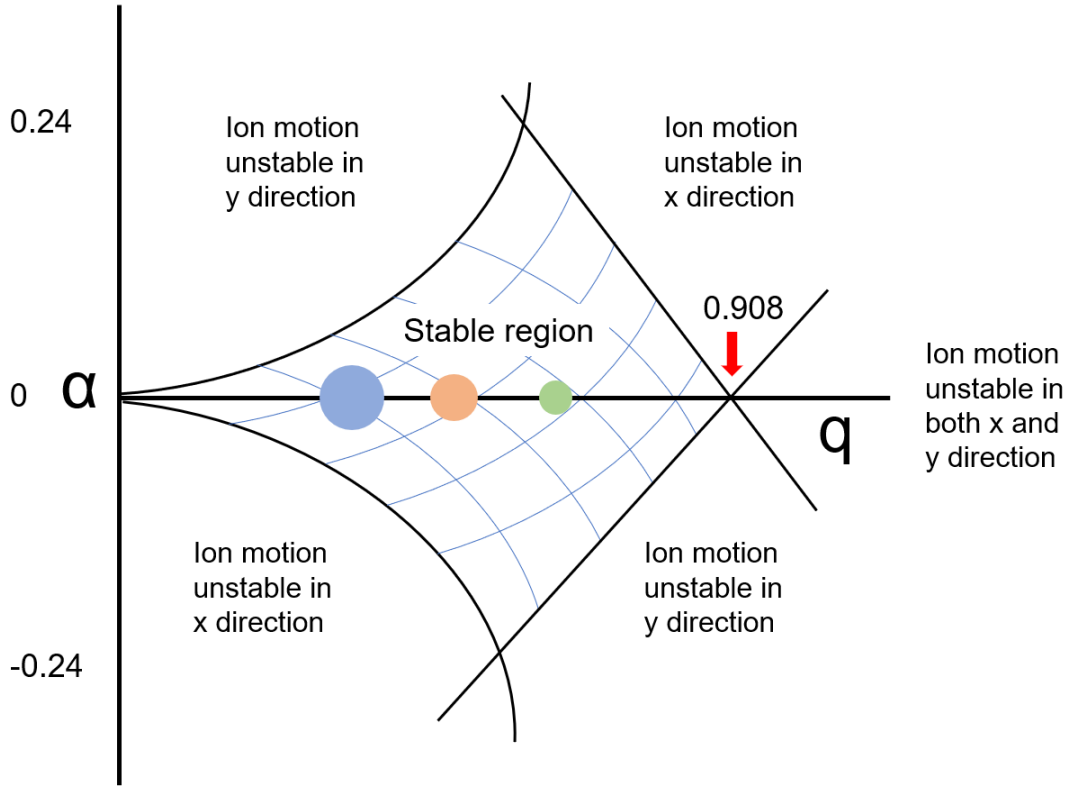


Figure 2.7 The Mathieu stability diagram describing ion motion within the ion trap. Ions are represented as different colored circles with the color and size reflecting the m/z -value of the ion. If an ion has a and q parameters inside the stable region, the ion is trapped within the ion trap. If an ion has a and q parameters outside the stable region, the ion motion becomes unstable and the ion is ejected out of the ion trap.

2.3.4.2 Trapping of Ions in the Axial (z) Direction

To trap ions within the ion trap in the axial direction, different DC voltages were applied to the different sections of the four rods. The DC voltages applied to the front and back sections were designed to be slightly greater than the DC voltage applied to the center section. The differences in the DC voltages created a potential energy well which confined the ions into the center section of the ion trap. For trapping of positively charged ions, the typical DC voltages applied were -9, -12 and -7 for the front, center and back sections, respectively (**Figure 2.8**). For negative ion mode, the polarity of the DC voltages were reversed.²⁷ Helium gas was used as a buffer gas to cool down the ions through frictional collisions (without inducing fragmentation) to confine the ions as tight packets in the center of the ion trap.²⁸ Formation of tight ion packets helped to increase the efficiency of ion ejection, which improved the mass accuracy, sensitivity, and mass resolution.²⁹

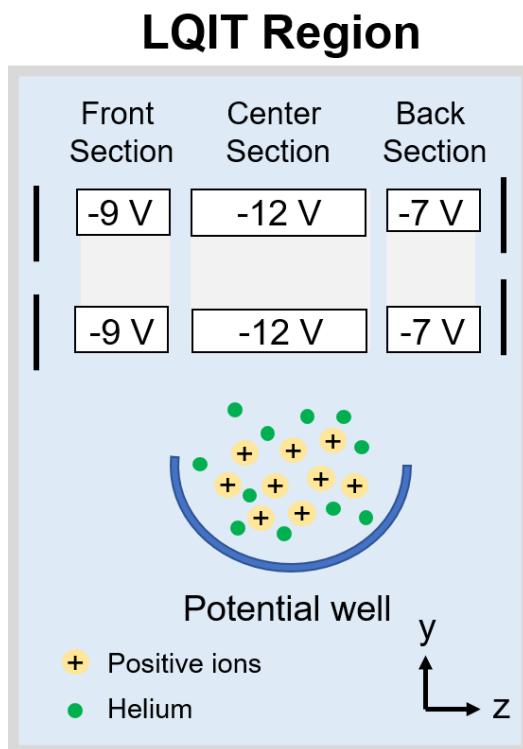


Figure 2.8 A schematic of the different sections of the linear quadrupole ion trap with the DC voltages applied to each section. This resulted in the generation of a potential energy well in the z-direction that trapped ions in the z-direction. The colored circles with charges represent ions trapped in the potential energy well. The colored circles with no charges represent helium atoms.

2.3.5 Ion Ejection for Detection

To eject ions out of the ion trap for detection, an axial instability scan method was employed. The q value of the trapped ions was increased by increasing the RF amplitude applied to the electrodes until it reached 0.908, at which point the ion trajectories become unstable in the x-direction and the ions were ejected through the slits in the exit electrodes (x electrodes) in a mass selective manner (smaller ion ejected first).³⁰ Unfortunately, the above ion ejection method suffers from several limitations. Therefore, an alternative, x-electrode bipolar resonance ejection method was employed.

When adopting the x-electrode bipolar resonance ejection method, the ions were ejected at a lower q -value, 0.88, by applying a supplemental RF voltage to the x-electrodes. When the ions

reached the q -value of 0.88, the oscillatory frequency of these ions came into resonance with the applied supplementary RF voltage, which caused the ions to gain additional kinetic energy.^{30,31} This gain in kinetic energy caused the oscillation amplitude of the ions to increase rapidly to an extent that the ions were ejected out of the ion trap through the slits in the x electrodes. Adoption of the x -electrode bipolar resonance ejection method minimized ion scattering and improved sensitivity.

2.3.6 Ion Detection with Electron Multipliers

After the ions were ejected from the linear quadrupole ion trap through the exit rods (x electrodes), the ions were detected by two off-axis ion detection systems.²⁷ These ion detection systems were situated on both sides of the two x electrodes and consisted of a conversion dynode and an electron multiplier (**Figure 2.9**). A potential +15 kV was applied to the conversion dynodes when detecting negative ions and -15 kV when detecting positive ions. The ion beam first struck the conversion dynode and produced secondary particles.²⁷ When positive ion beam struck the negative conversion dynode, the secondary particles included negative ions and electrons. When negative ion beam struck the positive conversion dynode, the secondary particles are positive ions. The conversion dynode focused and directed the secondary particles into the electron multiplier. A voltage gradient between the conversion dynode and the electron multiplier accelerated the secondary particles into the electron multiplier. The electron multipliers consisted of a cathode and an anode. The secondary particles struck the inner walls of the funnel-shaped cathode to eject electrons when entering the electron multiplier. The funnel-shaped cathode then directed the ejected electrons to hit the wall multiple times before reaching the end of the cathode. This process caused the emission of many electrons before they were collected at the anode. The number of secondary particles eventually striking the cathode was proportional to the ion current measured.

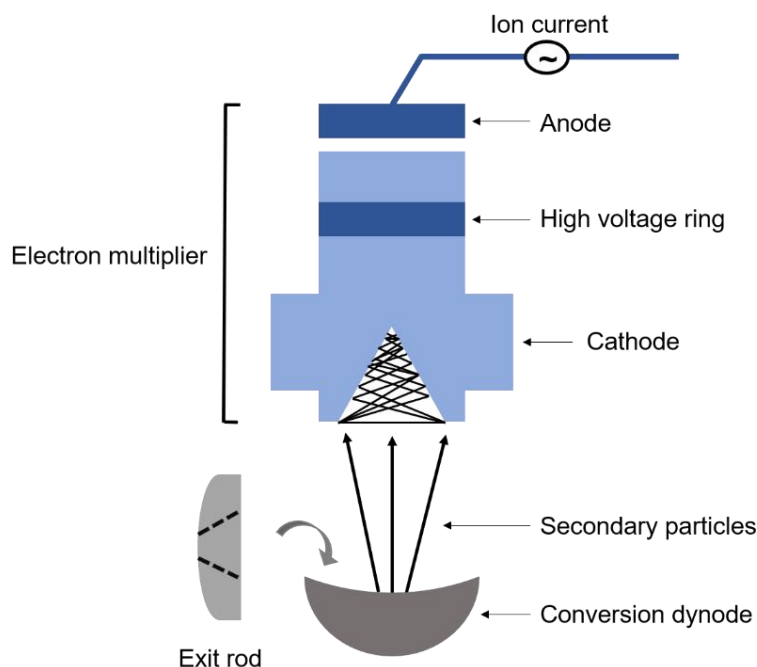


Figure 2.9 Illustration of an ion detection system. Each system consisted of a conversion dynode and an electron multiplier.

2.3.7 Multi-stage Tandem Mass Spectrometry

Multi-stage tandem mass spectrometry experiments involved several events of ion isolation followed by reactions before the final mass analysis.³² The final step of the experiment was the mass-selective detection of the generated product or fragment ions. . In this chapter, ion isolation, gas-phase ion-molecule reactions and collision-activated dissociation (CAD) reactions will be discussed.

2.3.8 Ion Isolation

Prior to isolation of the ions of interest, all ions trapped within the ion trap must have m/z and q values that are within the stable region of the Mathieu stability diagram. The ions with lower m/z -values have greater q -values than the ions with higher m/z -values based on Equation 2.12 (**Figure 2.10a**).²⁷ To isolate an ion of interest (green colored circle), the RF voltage applied on the

x-rods of the linear quadrupole ion trap was ramped up to increase the q values of all ions. The ramping of the RF voltage was terminated when the q value of the ion of interest reached 0.83. This process allowed most of the small ions to be ejected out of the ion trap (**Figure 2.10b**).²⁷ To eject the other ions remaining in the trap, with the exception of the ion of interest a broadband excitation waveform was applied to the x-rods (**Figure 2.10c**). The applied broadband excitation waveform had frequencies 5-500 kHz except for the frequency of the ion of interest. Therefore, after ramping the RF voltage followed by the application of the broadband excitation waveform on the x-rods, only the ions of interest remained in the ion trap.

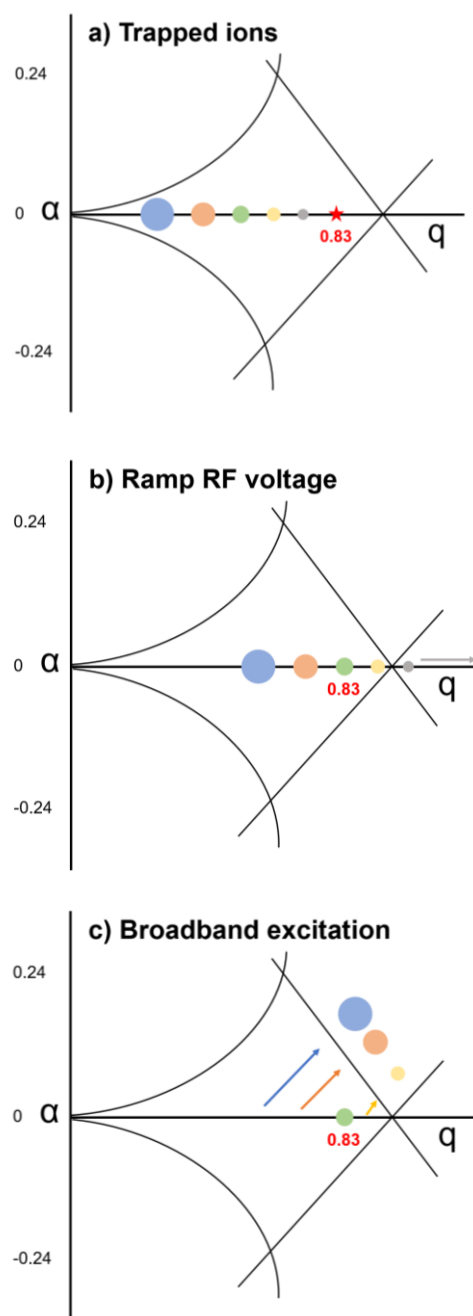


Figure 2.10 Illustration of ion isolation in the ion trap via the Mathieu stability diagram. A) Ions whose a and q parameters reside in the stable region of the Mathieu stability diagram and that therefore have stable motions in the ion trap. B) Ions with the smallest m/z -values have been ejected from the ion trap by ramping up the RF voltage (increasing the ions q -value) until the q -value of the ion of interest reaches 0.830. C) A broadband RF excitation waveform applied to the x -electrodes caused the ejection of all remaining ions except for the ion of interest by changing their a and q values.

2.3.9 Collision-activated Dissociation

CAD experiments carried out in a LQIT involved accelerating the isolated ions and subjecting them to multiple low-energy collisions with the helium buffer gas within the ion trap. Upon collisions with the helium buffer gas, part of the kinetic energy of the accelerated ions was converted into their internal energy, which caused their fragmentation.^{33,34}

CAD experiments began with lowering the RF amplitude and thereby reducing the q -value of the isolated ions until it reached 0.25. A supplemental RF voltage (tickle voltage) with a frequency equal to the resonance frequency of the isolated ion was then applied to the x -electrodes to accelerate the ions via a process called dipolar resonance excitation. This acceleration increased the kinetic energy of the isolated ions in the radial direction without ejecting them out of the ion trap. Upon collisions with the helium buffer gas, part of the kinetic energy of the isolated ions was converted into internal energy. After multiple collisions, the ions had accumulated enough internal energy to dissociate.

The q value selected for CAD experiments is crucial as it determines the low mass cut-off of the fragment ions that can be trapped and the kinetic energy that the accelerated ions can achieve. Ions activated at a greater q -value gain more kinetic energy, which can lead to more extensive fragmentation. However, selection of a greater q value results in a decrease in the observable mass range for the fragment ions. Typically, a q value of 0.25 was used for the CAD experiments in this thesis research.

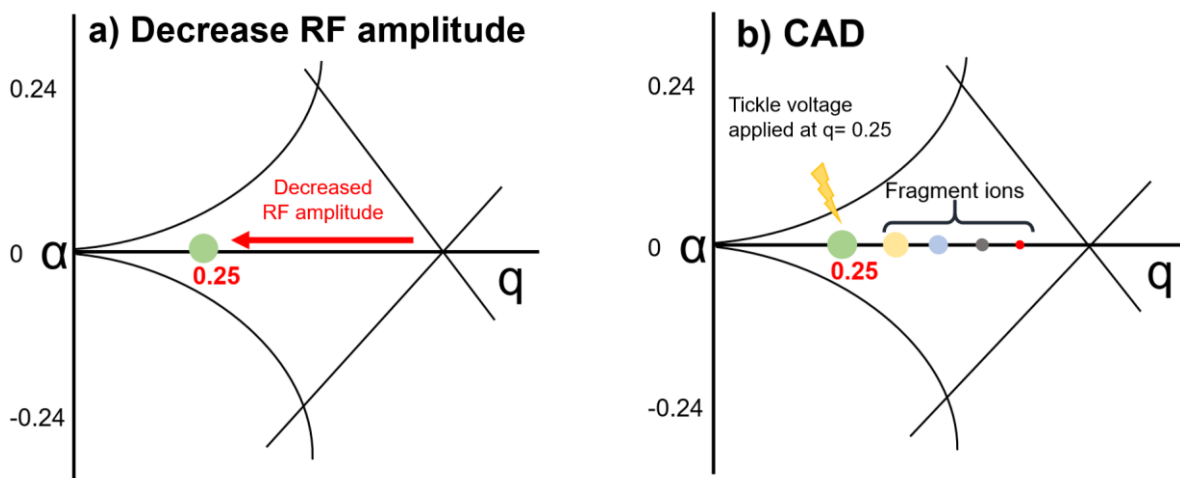


Figure 2.11 Illustration of the CAD process via the Mathieu stability diagram. A) The RF amplitude is decreased until the isolated ion (green circle) reaches a pre-set low q -value (typically 0.25). B) Tickle voltage is applied to the x-roads to increase the kinetic energy of the isolated ion (green circle). Part of the kinetic energy of the ion is converted into internal energy upon collisions with the helium buffer gas, which leads fragmentation (shown as yellow, blue, gray, and red circles).

2.3.10 Ion/molecule Reactions

Tandem mass spectrometry based on gas-phase ion-molecule reactions serves as a powerful alternative method to CAD for structural elucidation of gas-phase ions.¹² In this research, gas-phase ion molecule reaction experiments were conducted using a Thermo LTQ mass spectrometer equipped with a home-built external reagent mixing manifold (**Figure 2.12**).^{35,36} The reagent was introduced into the external reagent mixing manifold via a 500 μL Hamilton syringe at a flow rate of $\sim 5 \mu\text{L/h}$. The areas surrounding the syringe port were heated to ensure complete evaporation of the reagent. The external reagent mixing manifold was also connected to a helium tank and equipped with an exhaust to control the flow of the helium gas within the manifold. The injected reagent was then diluted with helium gas and directed into the ion trap by a constant flow of helium gas, controlled by a Granville-Phillips 203 variable leak valve. The isolated analyte ion discussed in section 2.3.8 was allowed to react with the reagent within the ion trap for a chosen period of time, ranging from 30 ms up to 10 s. All ions were then ejected out the ion trap for

detection as discussed in section 2.3.5. A vacuum pump was attached to the external reagent mixing manifold to pump out any residues of the reagents after each experiment.

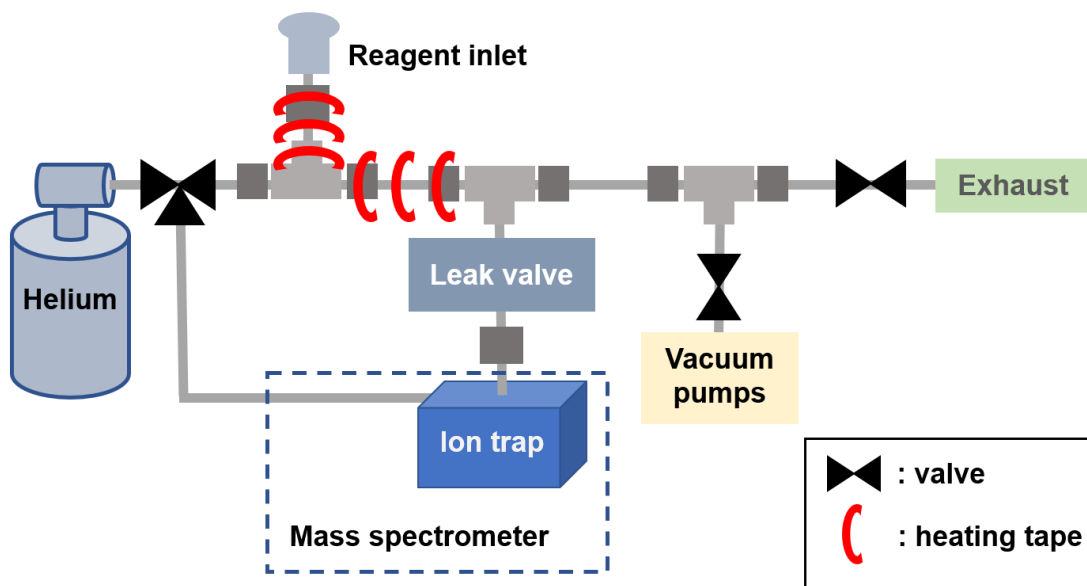


Figure 2.12 A schematic of the external reagent mixing manifold for the introduction of reagents into the ion trap.

For ion-molecule reactions to occur rapidly in vacuum (in the ion trap), the reactions must be exothermic with all barriers below the total energy level of the system. The energetics and kinetics of gas-phase ion-molecule reactions can be rationalized through the Brauman double-well potential energy surface (**Figure 2.13**).^{37,38} According to this model, upon a collision of an ion with a neutral reagent molecule in the gas phase, a long-lived reactant complex may be formed. This complex can be stabilized through ion-dipole or ion-induced dipole forces between the ion and the neutral reagent, which provides solvation energy to stabilize the ion. The long-lived reactant complex may proceed to form a product complex by utilizing the solvation energy to overcome any central barriers (transition states (TS)) that lie below the total energy level of the

system. The height of the highest central barrier usually correlates with the rate of the overall reaction.

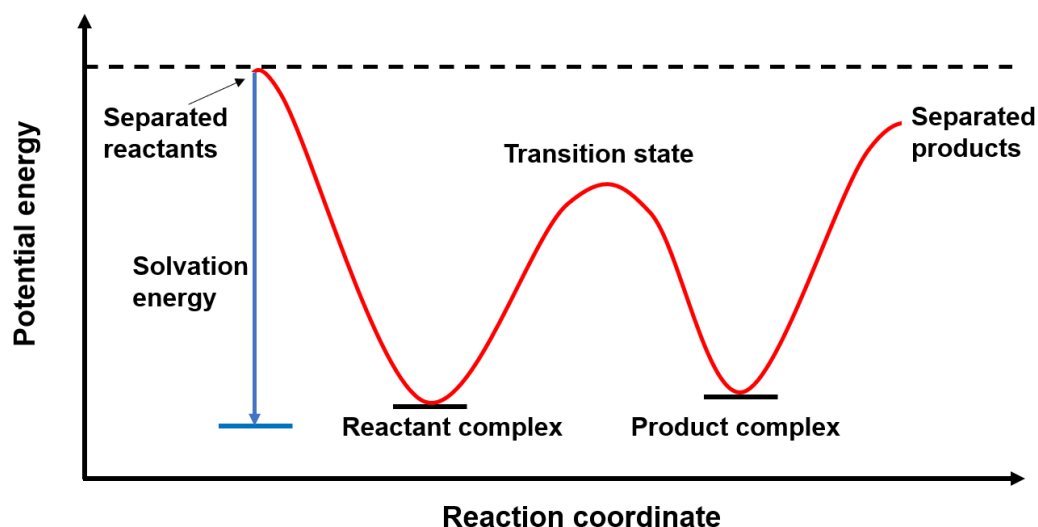


Figure 2.13 Schematic of the Brauman double-well potential energy surface.

However, in many cases, the dissociation of the reactant complex back to the separated reactants is entropically favored compared to overcoming the transition state for the formation of the reaction products. In these cases, the reaction may not occur fast even if it was exothermic and the solvation energy was large enough to overcome the barrier.

2.4 Orbitrap Mass Spectrometry

High-resolution experiments were conducted by using a LQIT coupled to an orbitrap mass analyzer. The orbitrap mass spectrometer was first introduced in 2000 by Alexander Makarov.³⁹ The design of the orbitrap mass spectrometer adopted the fundamental concepts of trapping ions in an orbital motion, which was first proposed by K.H. Kingdom in 1923.⁴⁰

Figure 2.14 illustrates a LQIT-orbitrap mass spectrometer. High resolution measurements were performed when the ion detection was performed in the orbitrap. The additional components of the LQIT-orbitrap mass spectrometer when compared to a LQIT mass spectrometer were an ion transfer octupole, a C-trap, and an orbitrap analyzer. For high resolution measurements, ions were first injected into the C-trap to form a tight ion packet that was transferred into the orbitrap mass analyzer for detection. Ion injection, ion motion, and ion detection in the orbitrap mass analyzer are discussed in the following sections. The MCAD cell was not used in this research, and therefore, it will not be discussed.

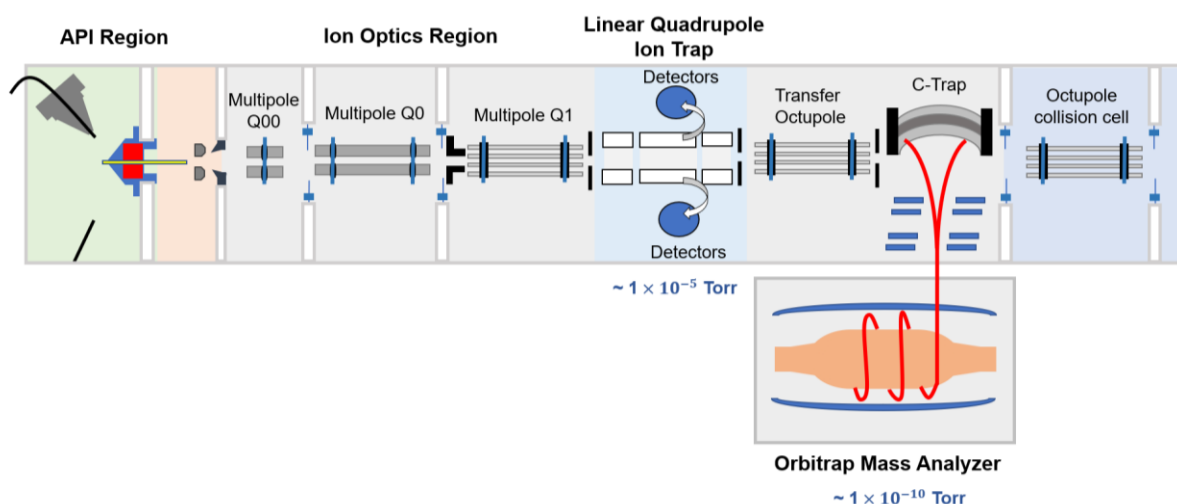


Figure 2.14 Schematic of a LQIT coupled to a high-resolution orbitrap mass analyzer.

2.4.1 Ion Injection into the Orbitrap

After ions exited the linear quadrupole ion trap, they traveled through an octupole into a C-trap. The purpose of the C-trap was to form a tight packet of the ions before they were injected into the orbitrap.⁴¹ A DC potential difference of 2-10 V between the back section of the linear quadrupole ion trap and the transfer octupole was applied to accelerate the ions from the linear quadrupole ion trap into the octupole. The ions were then transferred into the C-trap to which a

DC potential of 0 V was applied. C-trap was filled with nitrogen gas at ~1 mTorr, which served as a damping gas to cool down the ions before they were transferred into the orbitrap analyzer. Prior to ejection out of the C-trap, the ions were compressed in the z-direction by applying 200 V to the electrodes located at both ends of the C-trap. Ions were then ejected out of the exit electrode, which was situated at the curvature center of the C-trap. The ions were injected at high kinetic energies as a tight ion packet into the z-direction off-center of the orbitrap (Figure 2.15) which was operated under ultrahigh vacuum of 1×10^{-10} Torr.⁴¹

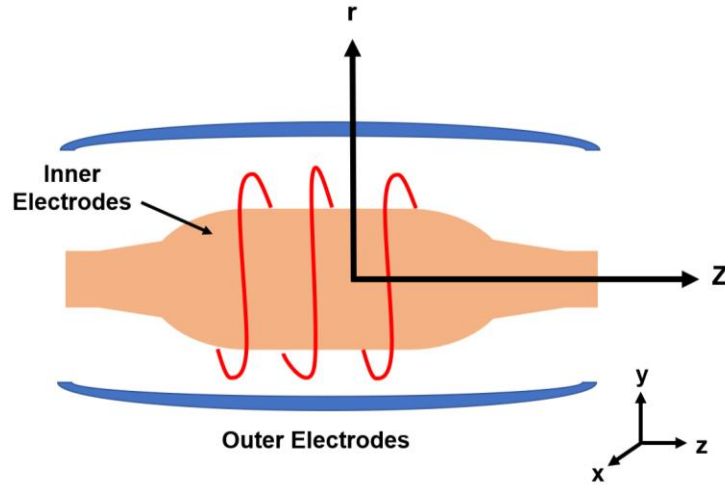


Figure 2.15 Cutaway view of the orbitrap mass analyzer

2.4.2 Equations of Motion for Ions in the Orbitrap

The orbitrap was composed of two electrodes: an inner spindle-like electrode and an outer barrel-like electrode. Between these two electrodes, a DC potential was applied, which resulted in ion trapping via an electrostatic field (U) that can be described as shown in Equation 2.13.³⁹

$$U(r,z) = \frac{k}{2}(z^2 - \frac{r^2}{2}) + \frac{k}{2}(R_m)^2 \ln \left[\frac{r}{R_m} \right] + C \quad \text{Equation 2.13}$$

where r corresponds to the angular coordinates of the field and z to the axial coordinates of the field, k is the field curvature, R_m is the characteristic radius of ion motion, and C is a constant.

In the field within the orbitrap, the stable trajectories of the ions involve rotation around the central electrode and oscillation along the z -axis (**Figure 2.15**). The ions with stable trajectories experience three types of motion, each with a unique frequency: rotational motion around the inner electrode (ω_ϕ), radial motion (ω_r) and oscillation motion along the axial direction (ω_z). Equations for each type of ion motion can be expressed in terms of the mass to charge ratio of the ions (m/q) in polar coordinates (r, ϕ, z) as shown below.

$$\frac{\partial^2 r}{\partial t^2} - \left(\frac{\partial \phi}{\partial t}\right)^2 = -\frac{q}{m} \frac{k}{2} \left[\frac{R_m^2}{r} - r\right] \quad \text{Equation 2.14}$$

$$\frac{d}{dt} \left(r^2 \frac{\partial \phi}{\partial t} \right) = 0 \quad \text{Equation 2.15}$$

$$\frac{\partial^2 z}{\partial t^2} = -kz \frac{q}{m} \quad \text{Equation 2.16}$$

Since the equation of motion along the axial direction (Equation 2.16) describes an oscillation frequency which is independent of the positions of the ions, the axial frequency of the ions can be used to derive the following equation to determine the m/z value of ions:

$$\omega = \sqrt{\left(\frac{q}{m}\right)k} \quad \text{Equation 2.17}$$

where m and q are the mass and the charge of the ion, respectively, and k is a constant that is proportional to the DC voltage applied between the two electrodes.

2.4.3 Ion Detection

The tight ion packets were rapidly injected into the z -direction off-center of the orbitrap (Figure 2.15) to ensure that the ions oscillate axially in a coherent manner. The coherent motion

of the ions along the z-axis induced an image current on the outer electrode. The image current was amplified and transformed into a frequency spectrum by fast Fourier transformation. The frequency spectrum was converted into a mass spectrum based on Equation 2.17.⁴¹ The orbitrap analyzer was operated at the resolution of 60,000 (full width at half maximum).

2.5 High-performance Liquid Chromatography/Tandem Mass Spectrometry (HPLC/MS²)

MSⁿ can be coupled to high-performance liquid chromatography (HPLC) to achieve separation and obtain structural information for components of complex mixtures in a single experiment.¹⁰ The HPLC/MSⁿ experiments discussed in this dissertation were performed using a Thermo Scientific LQIT mass spectrometer. A Thermo Scientific Surveyor Plus high-performance liquid chromatograph equipped with an autosampler, a quaternary pump, a column compartment, and a photodiode array (PDA) detector were used for the HPLC experiments. The mobile phases used were water (A) and methanol (B), both containing 0.1% formic acid. The column used was an Agilent ZORBAX SB-C18 (5 μ m, 4.6 \times 250 mm). A flow rate of 600 μ L/min of the mobile phase was used for the HPLC/MSⁿ experiments. The gradient of the mobile phases will be further discussed in the experimental section of Chapter 3. The ion source chosen for the HPLC/MSⁿ experiments was APCI operated in the positive-ion mode.

2.6 References

- (1) Petzold, C. J.; Nelson, E. D.; Lardin, H. A.; Kenttämä, H. I. Charge-Site Effects on the Radical Reactivity of Distonic Ions. *J. Phys. Chem. A* **2002**, *106* (42), 9767–9775. <https://doi.org/10.1021/jp025521i>.
- (2) Belas, F. J.; Blair, I. A. Mass Spectrometry in Pharmaceutical Analysis. *J. Liposome Res.* **2001**, *11* (4), 309–342. <https://doi.org/10.1081/LPR-100108611>.
- (3) Dettmer, K.; Aronov, P. A.; Hammock, B. D. Mass Spectrometry-Based Metabolomics. *Mass Spectrom. Rev.* **2007**, *26* (1), 51–78. <https://doi.org/10.1002/mas.20108>.

- (4) Castellino, S.; Lareau, N. M.; Groseclose, M. R. The Emergence of Imaging Mass Spectrometry in Drug Discovery and Development: Making a Difference by Driving Decision Making. *J. Mass Spectrom.* **2021**, *56* (8). e4717: 1-17 <https://doi.org/10.1002/jms.4717>.
- (5) Marshall, A. G.; Rodgers, R. P. Petroleomics: Chemistry of the Underworld. *Proc. Natl. Acad. Sci.* **2008**, *105* (47), 18090–18095. <https://doi.org/10.1073/pnas.0805069105>.
- (6) Richardson, S. D. Mass Spectrometry in Environmental Sciences. *Chem. Rev.* **2001**, *101* (2), 211–254. <https://doi.org/10.1021/cr990090u>.
- (7) Han, X.; Aslanian, A.; Yates, J. R. Mass Spectrometry for Proteomics. *Curr. Opin. Chem. Biol.* **2008**, *12* (5), 483–490. <https://doi.org/10.1016/j.cbpa.2008.07.024>.
- (8) Niyonsaba, E.; Manheim, J. M.; Yerabolu, R.; Kenttämä, H. I. Recent Advances in Petroleum Analysis by Mass Spectrometry. *Anal. Chem.* **2019**, *91* (1), 156–177. <https://doi.org/10.1021/acs.analchem.8b05258>.
- (9) Mas̆tovska, K.; Lehotay, S. J. Practical approaches to fast gas chromatography-mass spectrometry. *J. Chromatogr. A.* **2003**, *1000*(1-2), 153-180. doi:10.1016/s0021-9673(03)00448-5
- (10) Habicht, S. C.; Duan, P.; Vinueza, N. R.; Fu, M.; Kenttämä, H. I. Liquid Chromatography/Tandem Mass Spectrometry Utilizing Ion-Molecule Reactions and Collision-Activated Dissociation for the Identification of N-Oxide Drug Metabolites. *J. Pharm. Biomed. Anal.* **2010**, *51* (4), 805–811. <https://doi.org/10.1016/j.jpba.2009.09.047>.
- (11) de Hoffmann, E.; Stroobant, V. *Mass Spectrometry: Principles and Applications.*, 3rd ed.; John Wiley & Sons Ltd: West Sussex, England, 2007.
- (12) Liu, J. K.; Niyonsaba, E.; Alzarini, K. Z.; Boulos, V. M.; Yerabolu, R.; Kenttämä, H. I. Determination of the Compound Class and Functional Groups in Protonated Analytes via Diagnostic Gas-phase Ion-molecule Reactions. *Mass Spectrom. Rev.* **2021**, mas.21727: 1-17. <https://doi.org/10.1002/mas.21727>.
- (13) Ma, S.; Zhu, M. Recent Advances in Applications of Liquid Chromatography–Tandem Mass Spectrometry to the Analysis of Reactive Drug Metabolites. *Chem. Biol. Interact.* **2009**, *179* (1), 25–37. <https://doi.org/10.1016/j.cbi.2008.09.014>.
- (14) Boersema, P. J.; Mohammed, S.; Heck, A. J. R. Phosphopeptide Fragmentation and Analysis by Mass Spectrometry. *J. Mass Spectrom.* **2009**, *44* (6), 861–878. <https://doi.org/10.1002/jms.1599>.
- (15) Douglas, D. J. Linear Quadrupoles in Mass Spectrometry. *Mass Spectrom. Rev.* **2009**, *28* (6), 937–960. <https://doi.org/10.1002/mas.20249>.
- (16) Douglas, D. J.; Frank, A. J.; Mao, D. Linear Ion Traps in Mass Spectrometry. *Mass Spectrom. Rev.* **2005**, *24* (1), 1–29. <https://doi.org/10.1002/mas.20004>.

- (17) Makarov, A.; Denisov, E.; Kholomeev, A.; Balschun, W.; Lange, O.; Strupat, K.; Horning, S. Performance Evaluation of a Hybrid Linear Ion Trap/Orbitrap Mass Spectrometer. *Anal. Chem.* **2006**, 78 (7), 2113–2120. <https://doi.org/10.1021/ac0518811>.
- (18) Kebarle, P.; Verkerk, U. H. Electrospray: From Ions in Solution to Ions in the Gas Phase, What We Know Now. *Mass Spectrom. Rev.* **2009**, 28 (6), 898–917. <https://doi.org/10.1002/mas.20247>.
- (19) De Vijlder, T.; Valkenburg, D.; Lemi re, F.; Romijn, E. P.; Laukens, K.; Cuyckens, F. A Tutorial in Small Molecule Identification via Electrospray Ionization-Mass Spectrometry: The Practical Art of Structural Elucidation. *Mass Spectrom. Rev.* **2018**, 37 (5), 607–629. <https://doi.org/10.1002/mas.21551>.
- (20) Cech, N. B.; Enke, C. G. Practical Implications of Some Recent Studies in Electrospray Ionization Fundamentals. *Mass Spectrom. Rev.* **2001**, 20 (6), 362–387. <https://doi.org/10.1002/mas.10008>.
- (21) Konermann, L.; Ahadi, E.; Rodriguez, A. D.; Vahidi, S. Unraveling the Mechanism of Electrospray Ionization. *Anal. Chem.* **2013**, 85 (1), 2–9. <https://doi.org/10.1021/ac302789c>.
- (22) Iribarne, J. V. On the Evaporation of Small Ions from Charged Droplets. *J. Chem. Phys.* **1976**, 64 (6), 2287–2294. <https://doi.org/10.1063/1.432536>.
- (23) Wilm, M. Principles of Electrospray Ionization. *Mol Cell Proteomics* **2011**, 10 (7), 1–8. <https://doi.org/10.1074/mcp.M111.009407>.
- (24) Carroll, D. I.; Dzidic, I.; Stillwell, R. N.; Haegele, K. D.; Horning, E. C. Atmospheric Pressure Ionization Mass Spectrometry. Corona Discharge Ion Source for Use in a Liquid Chromatograph-Mass Spectrometer-Computer Analytical System. *Anal. Chem.* **1975**, 47 (14), 2369–2373. <https://doi.org/10.1021/ac60364a031>.
- (25) Weston, D. J. Ambient Ionization Mass Spectrometry: Current Understanding of Mechanistic Theory; Analytical Performance and Application Areas. *The Analyst* **2010**, 135 (4), 661–668. <https://doi.org/10.1039/b925579f>.
- (26) Kostianen, R.; Kauppila, T. J. Effect of Eluent on the Ionization Process in Liquid Chromatography–Mass Spectrometry. *J. Chromatogr. A* **2009**, 1216 (4), 685–699. <https://doi.org/10.1016/j.chroma.2008.08.095>.
- (27) Schwartz, J. C.; Senko, M. W.; Syka, J. E. P. A Two-Dimensional Quadrupole Ion Trap Mass Spectrometer. *J. Am. Soc. Mass Spectrom.* **2002**, 13 (6), 659–669. [https://doi.org/10.1016/S1044-0305\(02\)00384-7](https://doi.org/10.1016/S1044-0305(02)00384-7).
- (28) Stafford, G. C.; Kelley, P. E.; Syka, J. E. P.; Reynolds, W. E.; Todd, J. F. J. Recent Improvements in and Analytical Applications of Advanced Ion Trap Technology. *Int. J. Mass Spectrom. Ion Process.* **1984**, 60 (1), 85–98. [https://doi.org/10.1016/0168-1176\(84\)80077-4](https://doi.org/10.1016/0168-1176(84)80077-4).

- (29) Xu, W.; Song, Q.; Smith, S. A.; Chappell, W. J.; Ouyang, Z. Ion Trap Mass Analysis at High Pressure: A Theoretical View. *J. Am. Soc. Mass Spectrom.* **2009**, *20* (11), 2144–2153. <https://doi.org/10.1016/j.jasms.2009.06.019>.
- (30) Kaiser, R. E.; Graham Cooks, R.; Stafford, G. C.; Syka, J. E. P.; Hemberger, P. H. Operation of a Quadrupole Ion Trap Mass Spectrometer to Achieve High Mass/Charge Ratios. *Int. J. Mass Spectrom. Ion Process.* **1991**, *106*, 79–115. [https://doi.org/10.1016/0168-1176\(91\)85013-C](https://doi.org/10.1016/0168-1176(91)85013-C).
- (31) Schwartz, J. C.; Syka, J. E. P.; Jardine, I. High Resolution on a Quadrupole Ion Trap Mass Spectrometer. *J. Am. Soc. Mass Spectrom.* **1991**, *2* (3), 198–204. [https://doi.org/10.1016/1044-0305\(91\)80044-8](https://doi.org/10.1016/1044-0305(91)80044-8).
- (32) de Hoffmann, E. Tandem Mass Spectrometry: A Primer. *J. Mass Spectrom.* **1996**, *31* (2), 129–137. [https://doi.org/10.1002/\(SICI\)1096-9888\(199602\)31:2<129::AID-JMS305>3.0.CO;2-T](https://doi.org/10.1002/(SICI)1096-9888(199602)31:2<129::AID-JMS305>3.0.CO;2-T).
- (33) McLuckey, S. A. Principles of Collisional Activation in Analytical Mass Spectrometry. *J. Am. Soc. Mass Spectrom.* **1992**, *3* (6), 599–614. [https://doi.org/10.1016/1044-0305\(92\)85001-Z](https://doi.org/10.1016/1044-0305(92)85001-Z).
- (34) Mayer, P. M.; Poon, C. The Mechanisms of Collisional Activation of Ions in Mass Spectrometry. *Mass Spectrom. Rev.* **2009**, *28* (4), 608–639. <https://doi.org/10.1002/mas.20225>.
- (35) Gronert, S. Estimation of Effective Ion Temperatures in a Quadrupole Ion Trap. *J. Am. Soc. Mass Spectrom.* **1998**, *9* (8), 845–848. [https://doi.org/10.1016/S1044-0305\(98\)00055-5](https://doi.org/10.1016/S1044-0305(98)00055-5).
- (36) Habicht, S. C.; Vinueza, N. R.; Archibold, E. F.; Duan, P.; Kenttämä, H. I. Identification of the Carboxylic Acid Functionality by Using Electrospray Ionization and Ion–Molecule Reactions in a Modified Linear Quadrupole Ion Trap Mass Spectrometer. *Anal. Chem.* **2008**, *80* (9), 3416–3421. <https://doi.org/10.1021/ac800002h>.
- (37) Pellerite, M. J.; Brauman, J. I. Intrinsic Barriers in Nucleophilic Displacements. *J. Am. Chem. Soc.* **1980**, *102* (19), 5993–5999. <https://doi.org/10.1021/ja00539a003>.
- (38) Olmstead, W. N.; Brauman, J. I. Gas-Phase Nucleophilic Displacement Reactions. *J. Am. Chem. Soc.* **1977**, *10*.
- (39) Makarov, A. Electrostatic Axially Harmonic Orbital Trapping: A High-Performance Technique of Mass Analysis. *Anal. Chem.* **2000**, *72* (6), 1156–1162. <https://doi.org/10.1021/ac991131p>.
- (40) Kingdon, K. H. A Method for the Neutralization of Electron Space Charge by Positive Ionization at Very Low Gas Pressures. *Phys. Rev.* **1923**, *21* (4), 408–418. <https://doi.org/10.1103/PhysRev.21.408>.

- (41) Makarov, A.; Denisov, E.; Kholomeev, A.; Balschun, W.; Lange, O.; Strupat, K.; Horning, S. Performance Evaluation of a Hybrid Linear Ion Trap/Orbitrap Mass Spectrometer. *Anal. Chem.* **2006**, 78 (7), 2113–2120. <https://doi.org/10.1021/ac0518811>.
- (42) Kong, J. Y.; Yu, Z.; Easton, M. W.; Niyonsaba, E.; Ma, X.; Yerabolu, R.; Sheng, H.; Jarrell, T. M.; Zhang, Z.; Ghosh, A. K.; Kenttämä, H. I. Differentiating Isomeric Deprotonated Glucuronide Drug Metabolites via Ion/Molecule Reactions in Tandem Mass Spectrometry. *Anal. Chem.* **2018**, 90 (15), 9426–9433. <https://doi.org/10.1021/acs.analchem.8b02083>.
- (43) Zhang, M.; Eismin, R.; Kenttämä, H.; Xiong, H.; Wu, Y.; Burdette, D.; Urbanek, R. Identification of 2-Aminothiazolobenzazepine Metabolites in Human, Rat, Dog, and Monkey Microsomes by Ion-Molecule Reactions in Linear Quadrupole Ion Trap Mass Spectrometry. *Drug Metab. Dispos.* **2015**, 43 (3), 358–366. <https://doi.org/10.1124/dmd.114.061978>.
- (44) Sheng, H.; Williams, P. E.; Tang, W.; Zhang, M.; Kenttämä, H. I. Identification of the Sulfoxide Functionality in Protonated Analytes via Ion/Molecule Reactions in Linear Quadrupole Ion Trap Mass Spectrometry. *The Analyst* **2014**, 139 (17), 4296–4302. <https://doi.org/10.1039/C4AN00677A>.
- (45) Sheng, H.; Tang, W.; Yerabolu, R.; Kong, J. Y.; Williams, P. E.; Zhang, M.; Kenttämä, H. I. Mass Spectrometric Identification of the N-Monosubstituted N-Hydroxylamino Functionality in Protonated Analytes via Ion/Molecule Reactions in Tandem Mass Spectrometry. *Rapid Commun. Mass Spectrom.* **2015**, 29 (8), 730–734. <https://doi.org/10.1002/rcm.7154>.
- (46) Wei, J. N.; Duvenaud, D.; Aspuru-Guzik, A. Neural Networks for the Prediction of Organic Chemistry Reactions. *ACS Cent. Sci.* **2016**, 2 (10), 725–732. <https://doi.org/10.1021/acscentsci.6b00219>.
- (47) Gómez-Bombarelli, R.; Wei, J. N.; Duvenaud, D.; Hernández-Lobato, J. M.; Sánchez-Lengeling, B.; Sheberla, D.; Aguilera-Iparraguirre, J.; Hirzel, T. D.; Adams, R. P.; Aspuru-Guzik, A. Automatic Chemical Design Using a Data-Driven Continuous Representation of Molecules. *ACS Cent. Sci.* **2018**, 4 (2), 268–276. <https://doi.org/10.1021/acscentsci.7b00572>.
- (48) Müller, A. T.; Hiss, J. A.; Schneider, G. Recurrent Neural Network Model for Constructive Peptide Design. *J. Chem. Inf. Model.* **2018**, 58 (2), 472–479. <https://doi.org/10.1021/acs.jcim.7b00414>.
- (49) Liu, B.; Ramsundar, B.; Kawthekar, P.; Shi, J.; Gomes, J.; Luu Nguyen, Q.; Ho, S.; Sloane, J.; Wender, P.; Pande, V. Retrosynthetic Reaction Prediction Using Neural Sequence-to-Sequence Models. *ACS Cent. Sci.* **2017**, 3 (10), 1103–1113. <https://doi.org/10.1021/acscentsci.7b00303>.

- (50) Engkvist, O.; Norrby, P.-O.; Selmi, N.; Lam, Y.; Peng, Z.; Sherer, E. C.; Amberg, W.; Erhard, T.; Smyth, L. A. Computational Prediction of Chemical Reactions: Current Status and Outlook. *Drug Discov. Today* **2018**, *23* (6), 1203–1218. <https://doi.org/10.1016/j.drudis.2018.02.014>.
- (51) Coley, C. W.; Barzilay, R.; Green, W. H.; Jaakkola, T. S.; Jensen, K. F. Convolutional Embedding of Attributed Molecular Graphs for Physical Property Prediction. *J. Chem. Inf. Model.* **2017**, *57* (8), 1757–1772. <https://doi.org/10.1021/acs.jcim.6b00601>.
- (52) Coley, C. W.; Green, W. H.; Jensen, K. F. Machine Learning in Computer-Aided Synthesis Planning. *Acc. Chem. Res.* **2018**, *51* (5), 1281–1289. <https://doi.org/10.1021/acs.accounts.8b00087>.
- (53) Kearnes, S.; McCloskey, K.; Berndl, M.; Pande, V.; Riley, P. Molecular Graph Convolutions: Moving beyond Fingerprints. *J. Comput. Aided Mol. Des.* **2016**, *30* (8), 595–608. <https://doi.org/10.1007/s10822-016-9938-8>.
- (54) Fine, J.; Kuan-Yu Liu, J.; Beck, A.; Alzarieni, K. Z.; Ma, X.; Boulos, V. M.; Kenttämä, H. I.; Chopra, G. Graph-Based Machine Learning Interprets and Predicts Diagnostic Isomer-Selective Ion–Molecule Reactions in Tandem Mass Spectrometry. *Chem. Sci.* **2020**, *11* (43), 11849–11858. <https://doi.org/10.1039/D0SC02530E>.
- (55) Kong, J. Y.; Hilger, R. T.; Jin, C.; Yerabolu, R.; Zimmerman, J. R.; Replogle, R. W.; Jarrell, T. M.; Easterling, L.; Kumar, R.; Kenttämä, H. I. Integration of a Multichannel Pulsed-Valve Inlet System to a Linear Quadrupole Ion Trap Mass Spectrometer for the Rapid Consecutive Introduction of Nine Reagents for Diagnostic Ion/Molecule Reactions. *Anal. Chem.* **2019**, *91* (24), 15652–15660. <https://doi.org/10.1021/acs.analchem.9b03768>.

CHAPTER 3. DEVELOPMENT OF A METHOD FOR THE FAST IDENTIFICATION OF THE *N*-NITROSO FUNCTIONALITY IN UNKNOWN COMPOUNDS BY USING TANDEM MASS SPECTROMETRY BASED ON DIAGNOSTIC GAS-PHASE ION-MOLECULE REACTIONS

3.1 Introduction

N-Nitrosamines are potentially genotoxic and carcinogenic compounds¹ that are commonly found in air, water, food, packing materials, cosmetics and drugs.²⁻⁷ Over the past few years, the *N*-nitroso functionality was found to be present in some potentially mutagenic impurities (PMIs) that can be formed during the generation of pharmaceutical products.⁸ As a result, several drugs containing PMIs with a *N*-nitroso-group has been recalled from the market.⁹ Furthermore, new guidelines have been established by several agencies, such as the European Medicines Agency (EMA) and the United States Food and Drug Administration (FDA), to regulate the acceptable intake of some commonly detected *N*-nitrosamines.¹⁰ Therefore, a rapid and reliable method to identify *N*-nitroso functional groups in unknown analytes in complex mixtures are desired.

In previous studies, various analytical methods such as high-performance liquid chromatography with electrospray ionization mass spectrometry (HPLC/ESI MS) or atmospheric chemical ionization mass spectrometry (HPLC/ APCI MS), gas chromatography coupled to detectors including thermal energy analyzer (TEA), nitrogen–phosphorus detector, nitrogen chemiluminescence detector, and gas chromatography with chemical ionization mass spectrometry (GC/CI MS) have been developed for the detection of *N*-nitrosamines in air, water and food.^{2-4,11-18} Unfortunately, most of these methods target only a few specific *N*-nitrosamines, such as *N*-nitrosodimethylamine (NDMA) and *N*-nitrosodiethylamine (NDEA), and cannot be applied to the detection of many different *N*-nitrosamines.^{15,16} Therefore, a rapid, reliable, and generally

applicable method for the identification of the *N*-nitroso functional group in unknown analytes in complex mixtures needs to be developed.

Tandem mass spectrometry (MS²) based on collision-activated dissociation (CAD) has been extensively used in pharmaceutical industries to detect PMIs in complex mixtures.¹⁹ However, ionized *N*-nitrosamines, in general, do not fragment in a diagnostic manner upon CAD and hence, cannot be unambiguously detected using CAD (examples are provided in the Results and Discussion part).

In the past, several MS² methods based on diagnostic gas-phase ion-molecule reactions have been introduced for the successful identification of many different functional groups in previously unknown, protonated analytes that are difficult to identify based on CAD, including *N*-oxide, carbamate, sulfone and sulfoxide functional groups.²⁰ Therefore, in this study, a MS² method based on both CAD and diagnostic gas-phase ion-molecule reactions was developed for the identification of protonated *N*-nitrosamines. Quantum chemical calculations were employed to explore feasible mechanisms of the observed reactions in this study.

3.2 Results and Discussion

All model compounds in this study were protonated via APCI, isolated and subjected to CAD or gas-phase ion-molecule reactions in a linear quadrupole ion trap (LQIT) mass spectrometer. The CAD studies were conducted first to explore the utility of this approach to identify protonated *N*-nitrosamines and will be discussed first. Then the studies of ion-molecule reactions of protonated *N*-nitrosamines and protonated compounds containing functionalities will be discussed. Lastly, the detection limits for five FDA regulated *N*-nitrosamine will be determined through the HPLC/MS² experiments.

3.2.1 CAD studies

Upon CAD, protonated aliphatic *N*-nitrosamines were observed to fragment through a loss of an alkene, whereas protonated aromatic and cyclic *N*-nitrosamines fragmented via a NO radical loss and sometimes along with other losses. **Figure 3.1** illustrates this difference in fragmentation of the aromatic and aliphatic protonated *N*-nitrosamine via a comparison of the CAD mass spectra of an aliphatic protonated *N*-nitrosamine, *N*-nitrosomethyl-*N*-butylamine and an aromatic protonated *N*-nitrosamine, *N*-methyl-*N*-nitrosoaniline. Therefore, CAD experiments cannot be used to identify *N*-nitroso functionality unambiguously.

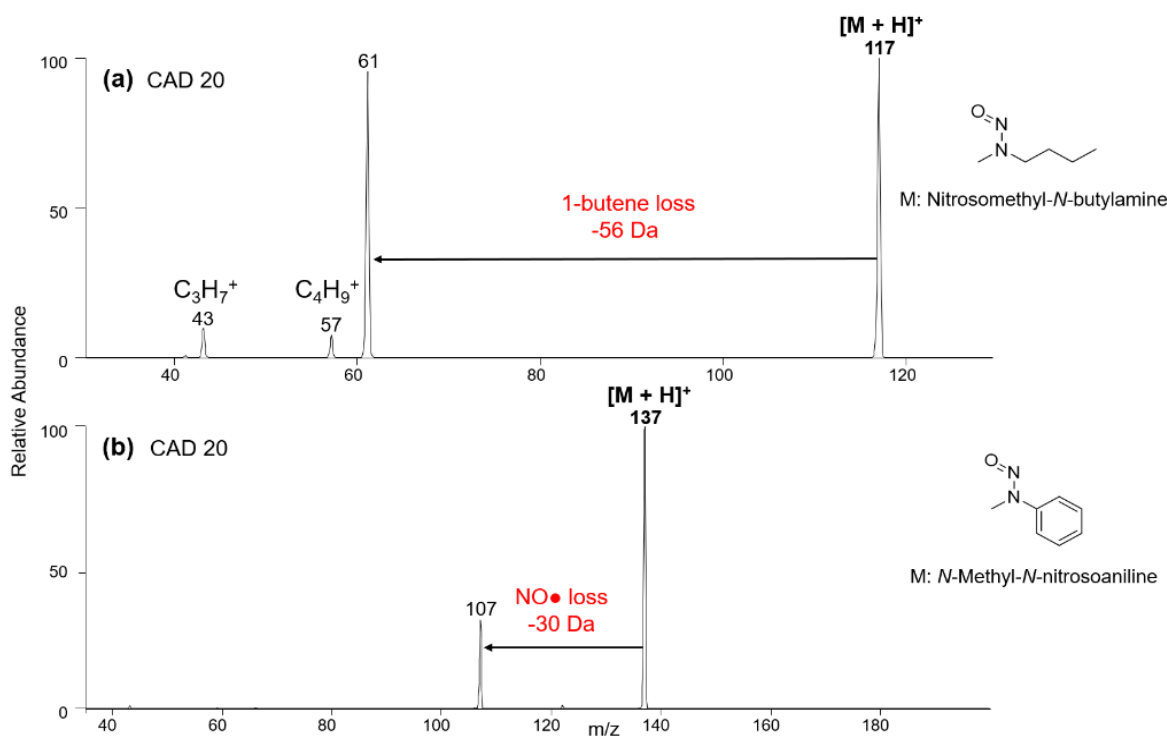


Figure 3.1 (a) CAD MS² spectrum (collision energy 20 arbitrary units) of protonated *N*-nitrosomethyl-*N*-butylamine, indicating the loss of 1-butene. (b) CAD MS² spectrum (collision energy 20 arbitrary units) of protonated *N*-methyl-*N*-nitrosoaniline, indicating the loss of a NO radical.

3.2.2 Ion-molecule Reaction Studies

Above results demonstrate that tandem mass spectrometry based on CAD is not a reliable method to identify *N*-nitroso compounds. Therefore, tandem mass spectrometry based on gas-phase ion-molecule reactions were explored. Most *N*-nitrosamines, upon protonation, lead to the formation a hydroxyl group which makes the nitroso moiety electrophilic and susceptible to nucleophilic attack.¹ 2-Methoxypropene (MOP) serves as a potential nucleophile for this study. The proton affinity (PA) of MOP (214 kcal/mol) is similar to most of the calculated PA values of the *N*-nitrosamines model compounds studied here (Table 1). Furthermore, MOP and its reactions with a wide variety of protonated analytes have been already examined previously.^{25,26} Therefore, the gas-phase reactivity of protonated *N*-nitrosamines towards MOP was examined. The experimental results are first discussed, followed by the computational results used to delineate a likely reaction mechanism for the diagnostic reaction. The selectivity of this method is then tested by examining protonated analytes with a variety of different functional groups. The CAD experiments results to address the false negative results obtained in the ion-molecule reactions are discussed.

3.2.3 Ion-molecule Reactions Studies of *N*-nitroso Compounds

Several mono- and polyfunctional *N*-nitrosamine model compounds were protonated via positive mode APCI, isolated, and allowed to react with MOP in a linear quadrupole ion trap (LQIT) mass spectrometer. As shown in **Table 3.1**, all protonated analytes containing *N*-nitroso functionality with three exceptions reacted with MOP to form a proton transfer product ion $[\text{MOP} + \text{H}]^+$ and a diagnostic product ion $[\text{M} + \text{H} + \text{MOP} - \text{MW } 58 \text{ Da}]^+$ which is 14 units greater in m/z -value than that of the protonated analyte. An example reaction mass spectrum of protonated *N*-

nitrosopyrrolidine with MOP is shown in **Figure 3.2a**. Protonated *N*-nitrosopyrrolidine (m/z 101) reacted with MOP (MW 72 Da) to yield a stable adduct ion, $[M + H + MOP]^+$ (m/z 173), and a diagnostic ion which has an m/z 115. To test whether the stable adduct, $[M + H + MOP]^+$ (m/z 173), is a precursor of the diagnostic product (m/z 115), the stable adduct ion was isolated and subjected to CAD (collision energy 10 arbitrary units) (**Figure 2b**). In **Figure 3.2b**, the ion of m/z 115 was observed in high abundance which ensures that the diagnostic product is generated from the stable adduct.

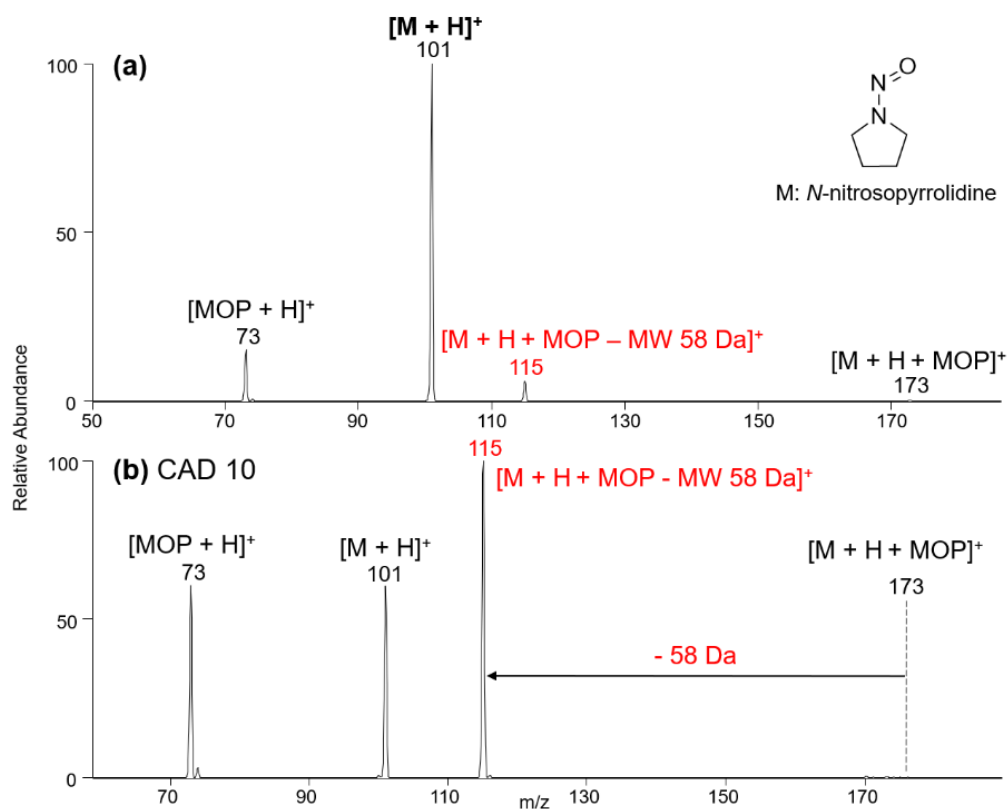


Figure 3.2 (a) MS² spectrum measured after 300 ms reactions of protonated *N*-nitrosopyrrolidine (m/z 101) with MOP. The observed product ions are a stable adduct, $[M + H + MOP]^+$ (m/z 173), a diagnostic product ion that is formed upon fragmentation of the adduct via elimination of propen-2-ol, $[M + H + MOP - MW\ 58\ Da]^+$ (m/z 115), and a proton transfer product, $[MOP + H]^+$ (m/z 73). (b) CAD MS³ spectrum (collision energy 10 arbitrary units) of the $[M + H + MOP]^+$ product ion (m/z 173).

Table 3.1 Product Ions (with Their Branching Ratios^a) Observed after Short Reaction Times (30 – 1000 ms) of Protonated *N*-Nitrosamines with MOP (PA= 214 kcal/mol^b). The structure of the product ion, $[M + H + MOP - CH_3C(OH)=CH_2]^+$, shown below was identified by using quantum chemical calculations (discussed later)

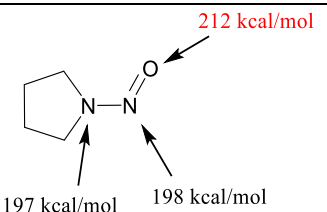
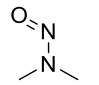
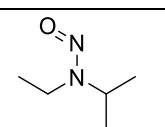
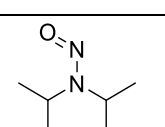
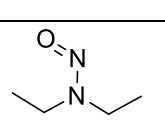
Analyte Structure (M) (<i>m/z</i> of $[M + H]^+$ ion)	Calculated PA (kcal/mol) ^c	Product ions (<i>m/z</i>) and their branching ratios (%) Diagnostic products in red	
 <i>N</i> -Nitrosopyrrolidine (101)	212	$[MOP + H]^+ (73)$ 66% $[M + H + MOP - CH_3C(OH)=CH_2]^+ (115)$ 29% $[M + H + MOP]^+ (173)$ 5%	
 <i>N</i> -nitrosodimethylamine (75)	206	$[MOP + H]^+ (73)$ 99% $[M + H + MOP - CH_3C(OH)=CH_2]^+ (89)$ 1%	
 <i>N</i> -Nitrosoethylisopropylamine (117)	215	$[MOP + H]^+ (73)$ 83% $[M + H + MOP - CH_3C(OH)=CH_2]^+ (131)$ 11% $[M + H + MOP]^+ (189)$ 6%	
 <i>N</i> -Nitrosodiisopropylamine (131)	215	$[MOP + H]^+ (73)$ 18% $[M + H + MOP - CH_3C(OH)=CH_2]^+ (145)$ 10% $[M + H + MOP]^+ (203)$ 72%	
 <i>N</i> -Nitrosodiethylamine (103)	214	$[MOP + H]^+ (73)$ 85% $[M + H + MOP - CH_3C(OH)=CH_2]^+ (117)$ 11% $[M + H + MOP]^+ (175)$ 4%	

Table 3.1 Continued

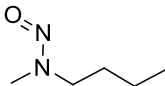
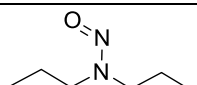
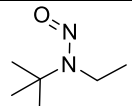
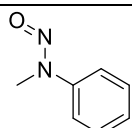
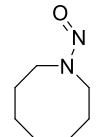
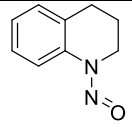
 Nitrosomethyl- <i>N</i> -butylamine (117)	211	[MOP + H] ⁺ (73)	88%
		[M + H + MOP - CH ₃ C(OH)=CH ₂] ⁺ (131)	10%
		[M + H + MOP] ⁺ (189)	2%
 <i>N</i> -Nitrosodipropylamine (131)	215	[MOP + H] ⁺ (73)	56%
		[M + H + MOP] ⁺ (203)	27%
		[M + H + MOP - CH ₃ C(OH)=CH ₂] ⁺ (145)	17%
 <i>N</i> -Ethyl- <i>N</i> - <i>tert</i> -butyl nitrosamine (131)	216	[M + H + MOP] ⁺ (203)	81%
		[MOP + H] ⁺ (73)	13%
		[M + H + MOP - CH ₃ C(OH)=CH ₂] ⁺ (145)	6%
 <i>N</i> -Methyl- <i>N</i> -nitrosoaniline (137)	210	[MOP + H] ⁺ (73)	99%
		[M + H + MOP - CH ₃ C(OH)=CH ₂] ⁺ (151)	1%
 <i>N</i> -Nitrosoazocane (143)	203	[MOP + H] ⁺ (73)	48%
		[M + H + MOP - CH ₃ C(OH)=CH ₂] ⁺ (157)	27%
		[M + H + MOP] ⁺ (215)	25%
 1-Nitroso-1,2,3,4-tetrahydroquinoline (163)	216	[MOP + H] ⁺ (73)	84%
		[M + H + MOP] ⁺ (235)	11%
		[M + H + MOP - CH ₃ C(OH)=CH ₂] ⁺ (177)	5%

Table 3.1 Continued

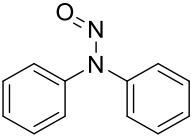
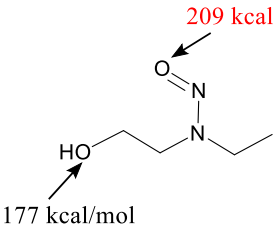
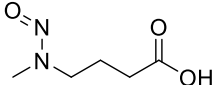
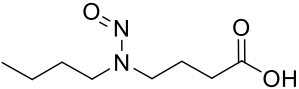
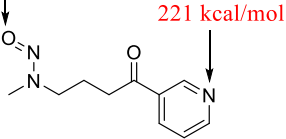
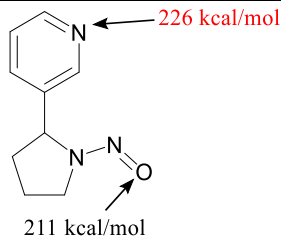
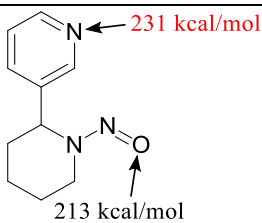
 <p><i>N</i>-Nitrosodiphenylamine (199)</p>	214	<p>$[MOP + H]^+ (73)$ 90%</p> <p>$[M + H + MOP]^+ (270)$ 7%</p> <p>$[M + H + MOP - CH_3C(OH)=CH_2]^+ (213)$ 3%</p>
 <p><i>N</i>-ethyl-<i>N</i>-(2-hydroxyethyl)nitrosamine (119)</p>	206	<p>$[MOP + H]^+ (73)$ 60%</p> <p>$[M + H + MOP - MeOH]^+ (159)$ 23%</p> <p>$[M + H + MOP - MeOH - Me_2CO]^+ (101)$ 12%</p> <p>$[M + H + MOP - CH_3C(OH)=CH_2]^+ (133)$ 7%</p>
 <p><i>N</i>-nitroso-<i>N</i>-methyl-4-aminobutyric acid (147)</p>	210	<p>$[MOP + H]^+ (73)$ 67%</p> <p>$[M + H + MOP]^+ (219)$ 16%</p> <p>$[M + H + MOP - CH_3C(OH)=CH_2]^+ (161)$ 12%</p> <p>$[M + H + CH_3C(OH)=CH_2]^+ (205)$ 5%</p>
 <p>4-(<i>N</i>-Butyl-<i>N</i>-nitrosamino) butyric acid (189)</p>	209	<p>$[M + H + MOP]^+ (261)$ 80%</p> <p>$[MOP + H]^+ (73)$ 13%</p> <p>$[M + H + MOP - CH_3C(OH)=CH_2]^+ (203)$ 7%</p>
 <p><i>N</i>-methyl-<i>N</i>-(4-oxo-4-(pyridin-3-yl)butyl)nitrous amide (208)</p>	221	<p>$[M + H + MOP]^+ (280)$ 100%</p>

Table 3.1 Continued

 <p>211 kcal/mol</p> <p><i>N</i>-Nitrosornicotine (178)</p>	226	[M + H + MOP] ⁺ (250)	100%
 <p>213 kcal/mol</p> <p><i>N</i>-Nitrosoanabasine (192)</p>	231	[M + H + MOP] ⁺ (264)	100%

^a Branching ratios were measured at several reaction times and found to be constant with time as no secondary reactions took place. The average branching ratios were obtained by calculating the mean of the branching ratios of each product ion tested in different days. ^b Ref. 25. ^c Also shown are the proton affinities (PA) in kcal/mol for different atoms in two of the analytes. PAs were calculated at the B3LYP/6-31++G(d,p) level of theory.

As mentioned above, this diagnostic product ion, ([M + H + MOP – MW 58 Da]⁺), was not observed for three protonated *N*-nitrosamines, *N*-methyl-*N*-(4-oxo-4-(pyridin-3-yl)butyl)nitrous amide, *N*-nitrosornicotine and *N*-nitrosoanabasine, upon reactions with MOP (Table 1). Three of these *N*-nitrosamines have substantially greater PAs (221, 226 and 231 kcal/mol, respectively) than MOP (214 kcal/mol) due to the presence of a strongly basic functionality, a pyridine moiety which explains the lack of diagnostic product ion formation. All the other *N*-nitrosamines studied have PAs either lower than MOP or within 2 kcal/mol from MOP (Table 1).

To better understand this behavior, quantum chemical calculations were carried out to delineate a likely mechanism for the diagnostic product ion formation. Erlu Feng provided the quantum chemical calculations to probe the mechanisms leading to the elimination of a molecule

with MW of 58 Da upon reaction of protonated *N*-nitrosopyrrolidine with MOP which was performed at the M06-2X/6-311++G(d,p) level of theory. Based on the proton affinity calculated for *N*-nitrosopyrrolidine (**Table 3.1**), the protonation site resides on the most basic atom, oxygen, of the compound with a proton affinity of 212 kcal/mol.

The CAD experiment discussed above demonstrates that the diagnostic product ion is formed from an initially formed adduct. Therefore, a feasible mechanism must begin by formation of an adduct. Based on calculations, the adduct, $[M + H + MOP]^+$, is formed upon nucleophilic addition of MOP to the positively charged and therefore electrophilic N=N double bond in protonated *N*-nitrosopyrrolidine (**Figure 3.3**). This is followed by transfer of a hydroxyl group from the N atom to a carbon atom in the MOP moiety. Upon transfer of the methoxyl group to the N atom, elimination a propen-2-ol molecule (58 Da) can take place to form the diagnostic ion, $[M + H + MOP - CH_3C(OH)=CH_2]^+$. This reaction is calculated to be exothermic by 14.6 kcal/mol.

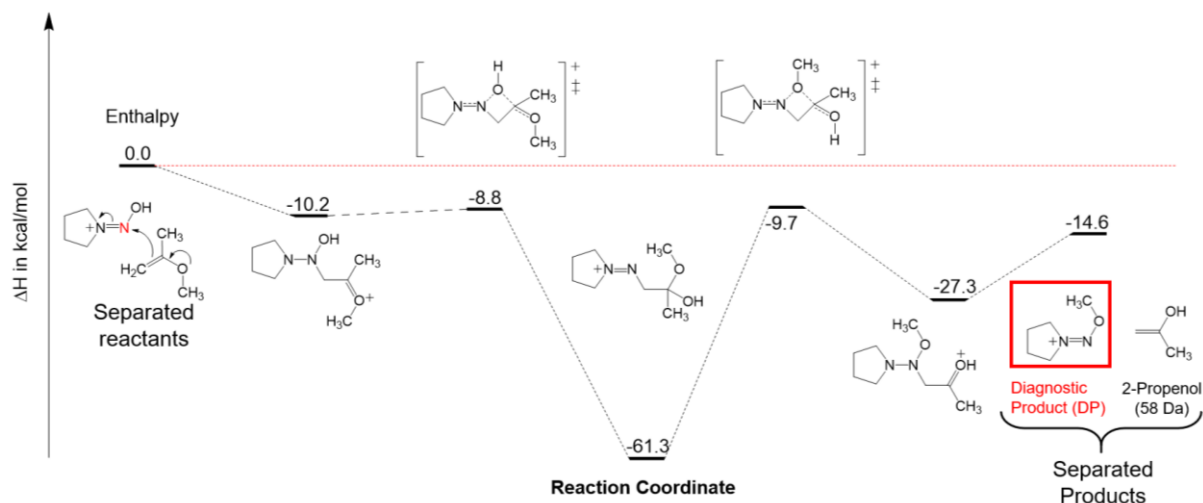


Figure 3.3 Potential energy surface calculated at the M06-2X/6-311++G-(d,p) level of theory for the formation of the ions $[M + H + MOP]^+$ and $[M + H + MOP - CH_3C(=CH_2)OH]^+$ upon reactions of protonated *N*-nitrosopyrrolidine with MOP provided by Erlu Feng.

Protonated *N*-methyl-*N*-(4-oxo-4-(pyridin-3-yl)butyl)nitrous amide, *N*-nitrosonornicotine and *N*-nitrosoanabasine were the only three *N*-nitrosamines that did not react with MOP to form the diagnostic ion, $[M + H + MOP - CH_3C(OH)=CH_2]^+$. This observation can be rationalized by the protonation sites of three *N*-nitrosamines residing on the more basic pyridine moiety, discussed earlier. A proton-bound dimer (adduct) is likely to form with MOP and the protonated pyridine instead of a nucleophilic addition of MOP to the N=N bond of the *N*-nitroso functionality. This is not surprising as based on literature, compounds with PAs much greater than that of MOP are more likely to form a stable adduct.²⁵ To explore other ways to identify these *N*-nitrosamine compounds, stable adducts formed from all three *N*-nitrosamines were isolated and subjected to CAD.

Upon CAD, all three adducts fragment via a loss of MOP to regenerate the protonated *N*-nitrosamine. The regeneration of MOP does not provide information of the presence of the *N*-nitroso functionality. Therefore, the regenerated protonated *N*-nitrosamines were isolated and subjected to CAD. In the second CAD event, a common loss of a NO radical was observed for these three protonated *N*-nitrosamines. An example of this reaction sequence is shown in **Figure 3.4**. Protonated *N*-nitrosonornicotine was allowed to react with MOP for 300 ms to form a stable adduct (**Figure 3.4a**). The stable adduct was isolated and subjected to CAD to regenerate the protonated *N*-nitrosonornicotine (**Figure 3.4b**). The regenerated protonated *N*-nitrosonornicotine was further isolated and fragmented via a loss of a NO radical (**Figure 3.4c**). Combining the above three observations, (1) only stable adduct formation upon reactions with MOP, (2) regeneration of the protonated *N*-nitroso compound upon CAD, and (3) diagnostic dissociation via NO loss, enables the identification of protonated *N*-nitrosamines containing a strongly basic functionality.

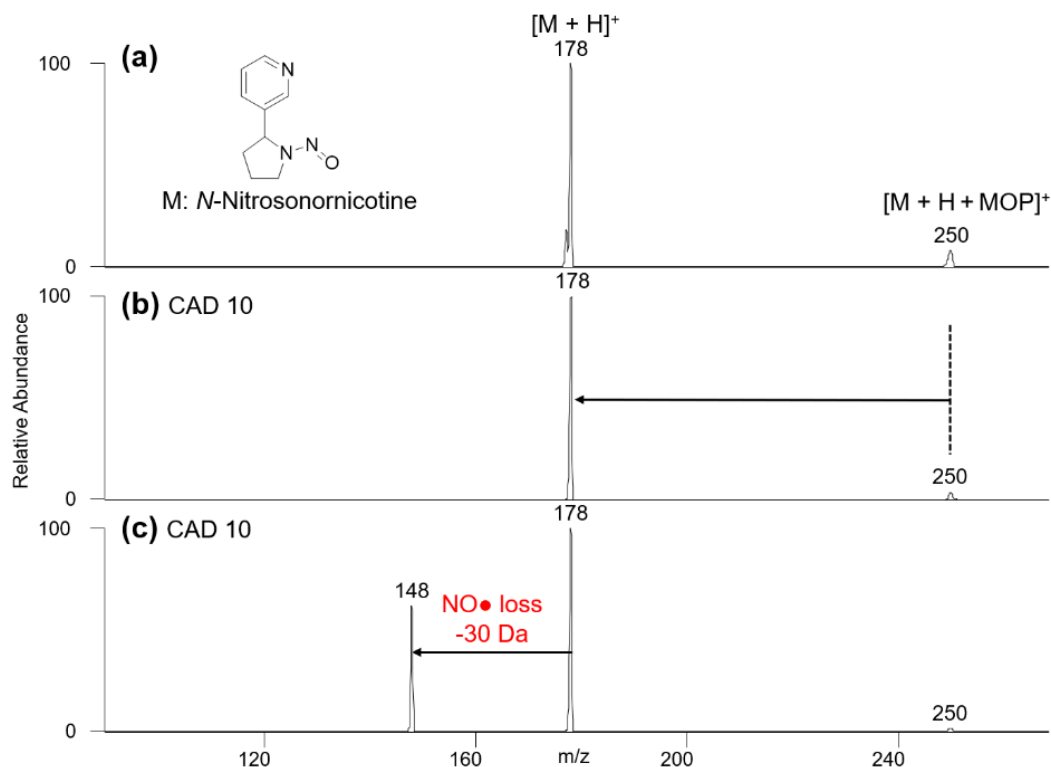


Figure 3.4 (a) MS² spectrum measured after 300 ms reactions of protonated *N*-nitrososornicotine with MOP, indicating the formation of an addition product $[M + H + MOP]^+$ (b) CAD MS³ spectrum (collision energy 10 arbitrary units) of $[M + H + MOP]^+$ (m/z 250), indicating the regeneration of $[M + H]^+$ (m/z 178) (c) CAD MS⁴ spectrum (collision energy 10 arbitrary units) of $[M + H]^+$ (m/z 178), indicating the diagnostic dissociation reaction via the loss of a NO radical.

3.2.4 Ion-Molecule Reaction Studies of Compounds Containing Various Functional Groups

The diagnostic ion, $[M + H + MOP - CH_3C(OH)=CH_2]^+$ has not been previously reported for reactions of MOP with 29 protonated compounds containing other functionalities such as hydroxylamines, sulfones, amines and *N*-oxides.^{25,26} To probe whether above methodology could differentiate *N*-nitroso functionality from other functional groups, reactions of 13 compounds with different functional groups were examined (**Table 3.2**). None of these protonated analytes reacted with MOP to form the diagnostic ion, $[M + H + MOP - CH_3C(OH)=CH_2]^+$, except for protonated

2-methoxycarboxylic acid and methyl phenyl sulfoxide. However, the other carboxylic acids and sulfoxides did not yield the diagnostic product ion. To conclude, with only two false positives cases observed for the 42 analytes studied, this methodology is considered to be robust for the identification of *N*-nitroso functionality in unknown analytes.

Differentiation of 2-methoxybenzoic acid from *N*-nitroso functionality can be achieved via ion-molecule reactions with (isopropenoxy)trimethylsilane (ITS) and/or trimethoxymethylsilane reagents.²⁷ For example, protonated carboxylic acids were observed to form a primary product [adduct-acetone]⁺. Furthermore, a secondary product 2° [adduct - acetone]⁺ is formed upon reactions of the [adduct - acetone]⁺ primary product with a second ITS molecule via addition and elimination of an acetone molecule.²⁷ This secondary product is not formed for protonated bifunctional *N*-nitroso compounds. To differentiate methyl phenyl sulfoxide functionality with *N*-nitroso functionality, reactions with a higher PA reagent can be used such as tris(dimethylamino)borane (TDMAB) with a PA value of 230 kcal/mol.²⁸ TDMAB was reported to react with protonated analytes with a sulfoxide functionality to predominately form an adduct followed by a loss of dimethylamine.²⁸ Since most *N*-nitrosamines have PA values around 210 ~ 215 kcal/mol which is much lower than that of TDMAB, upon reactions of protonated *N*-nitrosamines with TDMAB, proton transfer is a more preferred reaction.

Table 3.2 Product Ions (with Their Branching Ratios) Observed After Short Reaction Times (30 – 1000 ms) of Protonated Analytes with Various Functional Groups with MOP (PA = 214 kcal/mol^a)

Analyte Structure (M) (<i>m/z</i> of [M + H] ⁺ ion)	Calculated PA ^b (kcal/mol)	Product ions (<i>m/z</i>) and their branching ratios (%) Diagnostic product ions in red
Benzoic acid (123)	196	[MOP + H] ⁺ (73) 98% [M + H + 58 Da] ⁺ (181) 2%
4-Aminobenzoic acid (138)	207	[MOP + H] ⁺ (73) 100%
2-Methoxybenzoic acid (153)		[MOP + H] ⁺ (73) 77% [M + H + MOP - 58 Da] ⁺ (167) 9% [M + H + 58 Da] ⁺ (211) 3% [M + H + MOP] ⁺ (225) 11%
Methyl phenyl sulfoxide ^c (141)	220	[MOP + H] ⁺ (73) 59% [M + H + MOP] ⁺ (213) 32% [M + H + MOP - 58 Da] ⁺ (155) 5% [M + H + 58 Da] ⁺ (199) 6%
Diphenyl sulfoxide (203)	222	[M + H + MOP] ⁺ (275) 100%
Dodecyl methyl sulfoxide (233)		[M + H + MOP] ⁺ (305) 83% [M + H + CH ₃ C(=CH ₂)OH] ⁺ (291) 14% [MOP + H] ⁺ (73) 3%
<i>tert</i> -butylhydroxylamine (90)	213	[MOP + H] ⁺ (73) 100%
Phenylhydroxylamine (111)	204 ^d	[MOP + H] ⁺ (73) 89% [M + H + MOP] ⁺ (183) 8% [M + H + MOP - MeOH] ⁺ (151) 3%
Nitrosobenzene (108)		[MOP + H] ⁺ (73) 92% [M + H + MOP] ⁺ (180) 5% [M + H + MOP - MeOH] ⁺ (148) 3%
<i>N,N</i> -Dimethyl-4-nitrosoaniline (151)		No reaction

Table 3.2 Continued

1,3,5-tri-tert-Butyl-2-nitrosobenzene (276)	No reaction		
Aniline (94)	211 ^e	[MOP + H] ⁺ (73)	100%
Methyl phenyl sulfone (157)	201 ^e	[MOP + H] ⁺ (73)	87%
		[M + H + 58 Da] ⁺ (215)	12%
		[M + H + MOP] ⁺ (229)	1%

^a Ref. 25. ^b PAs were calculated at the B3LYP/6-31++G(d,p) level of theory. ^c False negative results were observed after 1000 ms reaction ^d Ref. 26. ^e Ref. 25.

Compounds with an *O*-nitroso functionality, even though not carcinogenic, are structurally similar to *N*-nitrosamines and are prone to lose a NO radical upon CAD (**Figure 3.5**). Therefore, to examine whether the proposed reaction sequence described above could differentiate protonated *N*-nitrosamines with strongly basic group from protonated *O*-nitroso compounds with strongly basic groups, two such compounds were proposed (structures shown in **Figure 3.6**), synthesized with the help of Yue Fu and tested.

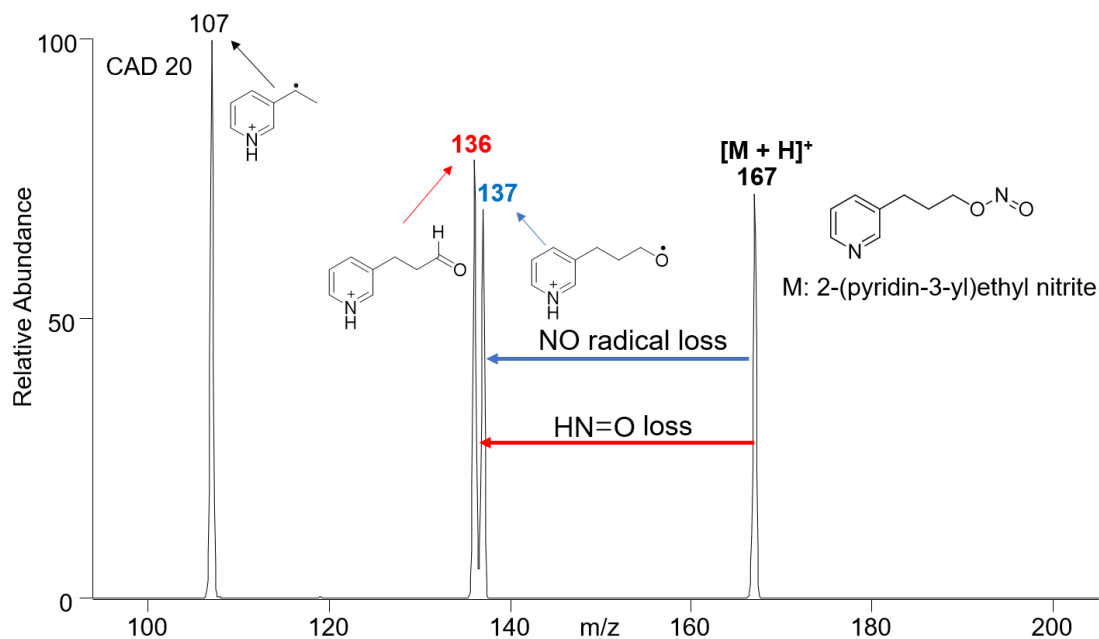


Figure 3.5 CAD MS² spectrum (collision energy 20 arbitrary units) of protonated 2-(pyridin-3-yl)ethyl nitrite, indicating the loss of NO radical loss.

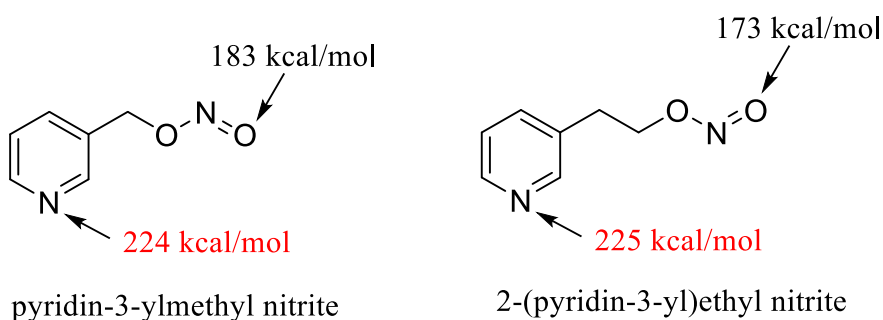


Figure 3.6 Structures of the synthesized *O*-nitroso compounds, pyridine-3-ylmethyl nitrite and 2-(pyridin-3-yl)ethyl nitrite. The calculated PA (in kcal/mol) of the nitrogen atoms on the pyridine moiety of each compound is labeled in red. The PA (in kcal/mol) of the oxygen atom on the *O*-nitroso-moiety of each compound is labeled in black. PAs were calculated at the B3LYP/6-31++G(d,p) level of theory.

As an example of the behavior of a protonated *O*-nitroso compound, 2-(pyridin-3-yl)ethyl nitrite, tested towards this reaction sequence is shown in **Figure 3.7**. A slow adduct formation was observed for the first step of the reaction sequence which was expected due to the presence of the strongly basic pyridine moiety within the compound (**Figure 3.7a**). Furthermore, the protonated 2-(pyridin-3-yl)ethyl nitrite was regenerated by isolating the adduct and subjecting to CAD (**Figure 3.7b**). In the last step of the sequence (**Figure 3.7c**), upon CAD of the regenerated protonated 2-(pyridin-3-yl)ethyl nitrite, an NO radical loss was observed, just like the protonated *N*-nitroso compounds with strongly basic functionality. However, an additional loss of an HN=O was observed for these protonated *O*-nitroso compounds upon the second CAD experiments (**Figure 3.7c**). Quantum chemical calculations of this dissociation reaction mechanism revealed that an aldehyde was formed upon elimination of the HN=O from the protonated *O*-nitroso model compounds (**Figure 3.8**). Therefore, HN=O loss reaction could be used to differentiate protonated *O*-nitroso compounds from protonated *N*-nitrosamine compounds with strongly basic functionality.

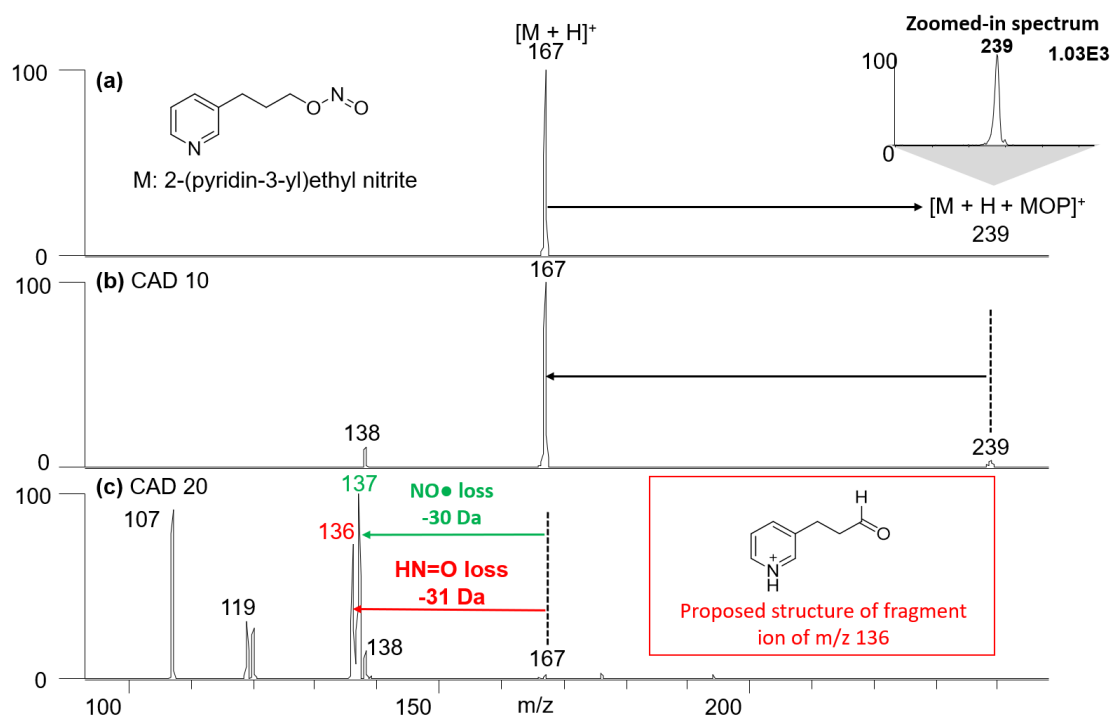


Figure 3.7 (a) MS^2 spectrum measured after 1000 ms reactions of protonated 2-(pyridin-3-yl)ethyl nitrite with MOP, indicating the formation of an addition product $[M + H + MOP]^+$ (b) CAD MS^3 spectrum (collision energy 10 arbitrary units) of $[M + H + MOP]^+$ (m/z 239), indicating the regeneration of $[M + H]^+$ (m/z 167) (c) CAD MS^4 spectrum (collision energy 20 arbitrary units) of $[M + H]^+$ (m/z 167), indicating the diagnostic dissociation reaction via a loss of a NO radical and a loss of a HN=O moiety.

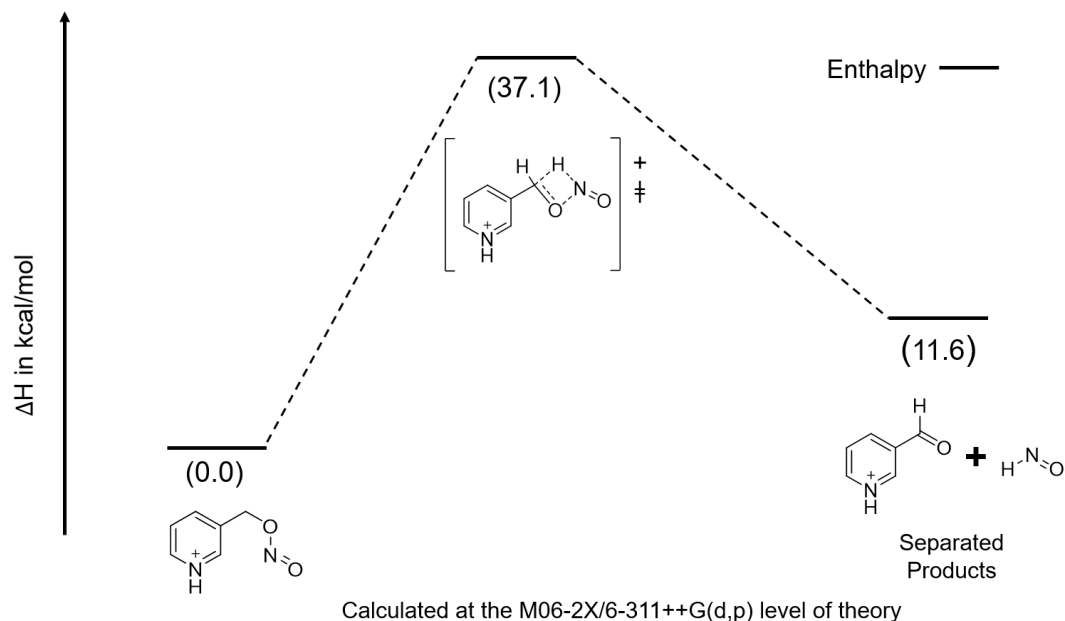


Figure 3.8 Potential energy surfaces calculated at the M06-2X/6-311++G(d,p) level of theory for CAD of the protonated 3-((nitrosooxy)methyl)pyridine generated upon reactions of protonated pyridine-3-carboxaldehyde.

3.2.5 HPLC/MS and HPLC/MS² experiments

In most cases, *N*-nitrosamine impurities are generated in trace levels during drug synthetic processes.²⁹ MS and MS² experiments involving ion-molecule reactions coupled with high-performance liquid chromatography (HPLC) were carried out to test the practicality of utilizing the proposed method to detect trace impurities containing *N*-nitroso functionality in mixtures. Five FDA-regulated *N*-nitrosamine compounds were made into an equimolar mixture and separated via reversed phase HPLC chromatography (**Figure 3.9**). These *N*-nitrosamines compounds were protonated via positive mode APCI as they eluted from the HPLC column and transferred into the ion trap. **Figure 3.9a** shows an extracted ion chromatogram obtained for the five protonated *N*-nitrosamines. Each protonated *N*-nitrosamine was isolated and allowed to react with MOP for 300 ms in the ion trap. Based on the observation of the diagnostic product ion $[M + H + MOP -$

$\text{CH}_3\text{C}(\text{OH})=\text{CH}_2]^+$ in the MS^2 spectra shown in **Figure 3.9b**, the compounds can be unambiguously identified as *N*-nitrosamines. The limits of detection for the diagnostic ion-molecule reaction product ion in, $[\text{M} + \text{H} + \text{MOP} - \text{CH}_3\text{C}(\text{OH})=\text{CH}_2]^+$, HPLC/ MS^2 experiments were determined to be 0.5, 0.5, 0.0025, 0.005, and 0.005 ppm for NDMA, NMBA, NDEA, EIPNA and DIPNA respectively, whereas the limits of detection for the analyte ion in simple HPLC/MS experiments were determined to be 0.1, 0.05, 0.005, 0.01, and 0.01 ppm for NDMA, NMBA, NDEA, EIPNA and DIPNA respectively. **Figure 3.10** shows an example of the LOD measured for EIPNA via HPLC/ MS^2 experiments based on ion-molecule reactions and HPLC/MS experiments. The poorer LOD values for NDMA and NBMA can be contributed to their low ion ionization efficiency via positive mode APCI.

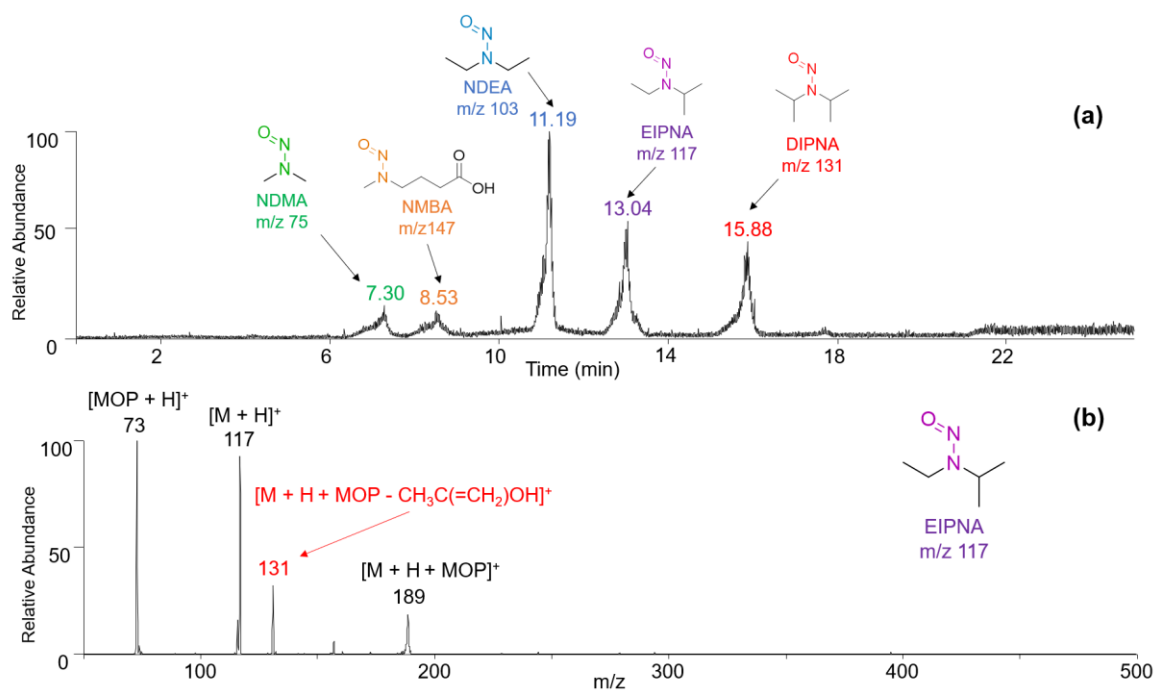


Figure 3.9 (a) HPLC/(+)APCI MS extracted ion chromatogram where the major peaks correspond to the five monitored protonated *N*-nitrosamines in the equal concentration 1 ppm mixture. NDMA: *N*-nitrosodimethylamine; NBMA: *N*-nitroso-*N*-methyl-4-aminobutyric; NDEA: *N*-nitrosodiethylamine; EIPNA: *N*-nitrosoethylisopropylamine; DIPNA: *N*-nitrosodiisopropylamine (b) MS² spectrum measured for protonated EIPNA (M) after reactions with MOP for 300 ms, indicating the formation of the diagnostic product ion [M + H + MOP - CH₃C(OH)=CH₂]⁺. EIPNA eluted at 12.2–13.2 min.

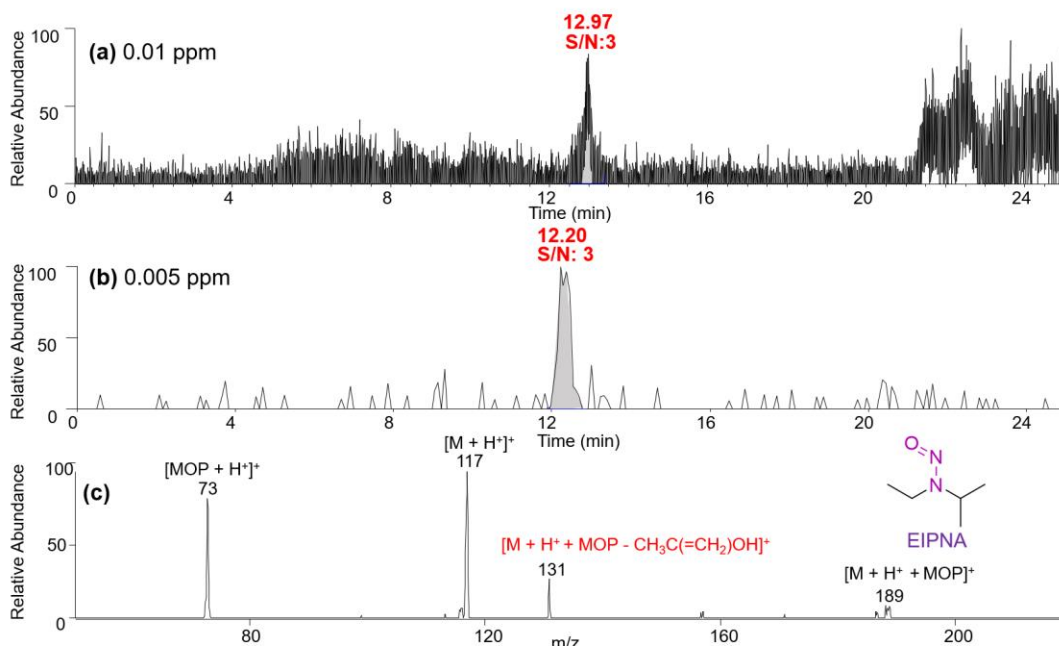


Figure 3.10 (a) HPLC/(+)APCI MS extracted ion chromatogram of protonated EIPNA at the limit of detection concentration (0.01ppm). The chromatogram shows the analyte peak at 12.97 min. (b) Extracted ion HPLC chromatogram for the diagnostic ion-molecule reaction product ion of m/z 131 (generated in an MS/MS experiment) measured for EIPNA at the limit of detection concentration (0.005 ppm). The chromatogram shows the analyte peak at 12.20 min. (c) MS² spectrum measured for protonated EIPNA (M; concentration: 0.005 ppm) after reactions with MOP for 300 ms, indicating the formation of the diagnostic product ion $[M + H + MOP - CH_3C(OH)=CH_2]^+$. The limit of detection measurement was performed three times.

3.3 Experimental Section

3.3.1 Chemicals

2-Methoxypropene (MOP; 99% purity) was purchased from Sigma-Aldrich and used without purification. Water (LC/MS grade, $\geq 99.9\%$) and methanol (LC/MS grade, $\geq 99.9\%$) were purchased from Fisher Scientific. *N*-nitrosopyrrolidine (Sigma Aldrich, 99%), *N*-nitrosodimethylamine (Sigma Aldrich, $\geq 99\%$), *N*-nitrosoethylisopropylamine (Enamine, 95%), *N*-Nitrosodiisopropylamine (Enamine, 95%), *N*-nitrosodiethylamine (Enamine, 95%), nitrosomethyl-*N*-butylamine (Sigma-Aldrich, $\sim 99.9\%$), *N*-nitrosodipropylamine (Sigma Aldrich, 99%), *N*-ethyl-*N*-*tert*-butylnitrosamine (Asta Tech, 98%), *N*-methyl-*N*-nitrosoaniline (Enamine, 95%), *N*-nitrosoazocane (Tokyo Chemical Industry, 99%), 1-nitroso-1,2,3,4-tetrahydroquinoline (Enamine, 95%), *N*-nitrosodiphenylamine (Sigma Aldrich, $\geq 97\%$), *N*-ethyl-*N*-(2-hydroxyethyl)nitrosamine (Tokyo Chemicals Industry, $>97\%$), *N*-nitroso-*N*-methyl-4-aminobutyric acid (Enamine, 95%), 4-(*N*-Butyl-*N*-nitrosamino) butyric acid (Tokyo Chemical Industry, $>98\%$), *N*-methyl-*N*-(4-oxo-4-(pyridin-3-yl)butyl)nitrous amide (Asta Tech, 95%), *N*-nitrosornicotine (Sigma Aldrich, $\geq 99\%$), *N*-nitrosoanabasine (Sigma-Aldrich, $\geq 99\%$), benzoic acid (Sigma Aldrich, $\geq 99.5\%$), 4-aminobenzoic acid (Sigma Aldrich, 99%), 2-methoxybenzoic acid (Sigma Aldrich, 99%), methyl phenyl sulfoxide (Sigma Aldrich, $\geq 97\%$), diphenyl sulfoxide (Sigma Aldrich, 96%), dodecyl methyl sulfoxide (Sigma Aldrich, 98%), *tert*-butylhydroxylamine (Sigma Aldrich, 98%), phenylhydroxylamine (Sigma Aldrich, $\geq 95\%$), nitrosobenzene (Sigma Aldrich, $\geq 97\%$), *N,N*-dimethyl-4-nitrosoaniline (Sigma Aldrich, 97%), 1,3,5-tri-*tert*-butyl-2-nitrosobenzene (Tokyo Chemical Industry, $>98\%$), aniline (Sigma Aldrich, $\geq 99.5\%$), methyl phenyl sulfone (Sigma Aldrich, $\geq 98\%$), All purchased chemicals were used as received. Yue Fu

and I synthesized the two *O*-nitroso model compounds studied, pyridine-3-ylmethyl nitrite and 2-(pyridin-3-yl)ethyl nitrite using procedures provided by MERCK (Section 3.2.2).

3.3.2 Synthesis procedure for *O*-nitroso compounds

3.2.2.1 Synthesis of pyridine-3-ylmethyl nitrite.

3-Pyridinemethanol (13.4 μ L, 0.200 mmol) was added into 2 mL of tert-butyl nitrite in a 10-mL round-bottom flask at 40 °C. The mixture was stirred using a stirring bar at 500 rpm for 12 h while the temperature remained 40 °C. The reaction mixture was diluted in methanol, and then analyzed by (+)ESI high-resolution MS. HRMS (ESI): m/z Calc. for $C_6H_7O_2N_2$ $[M + H]^+$: 139.0502, found: 139.0501.

3.2.2.2 Synthesis of 2-(pyridin-3-yl)ethyl nitrite.

3-Pyridinepropanol (25.8 μ L, 0.200 mmol) was added into 2 mL of tert-butyl nitrite in a 10-mL round-bottom flask at 40 °C. The mixture was stirred using a stirring bar at 500 rpm for 12 h while the temperature remained 40 °C. The reaction mixture was diluted in methanol, and then analyzed by (+)ESI high-resolution MS. HRMS (ESI): m/z Calc. for $C_6H_7O_2N_2$ $[M + H]^+$: 167.0815, found: 167.0811.

3.3.3 Mass spectrometry

All experiments were performed using a Thermo Scientific linear quadrupole ion trap mass spectrometer (LQIT) equipped with an atmospheric pressure chemical ionization (APCI) source, operated in positive ion mode. Samples were dissolved in methanol at concentrations ranging from 0.01 to 1 mg/mL. These sample solutions were injected into the APCI source by using a syringe

pump and a 500 μL Hamilton syringe at a flow rate of 15 $\mu\text{L}/\text{min}$. Typical flow rates of sheath and auxiliary gases (N_2) into the APCI source were 30 and 10 (arbitrary units), respectively. The vaporizer and capillary temperatures were set at 300 $^\circ\text{C}$ and 275 $^\circ\text{C}$, respectively. The analytes were protonated upon APCI. The ions were transferred into the linear quadrupole ion trap for reactions. The ion optic voltages were optimized through the tune feature of the LTQ Tune Plus interface for each analyte. Protonated *N*-nitrosamine model compounds were isolated in the quadrupole ion trap by ejecting all unwanted ions from the trap before examining their reactions. Isolation of the analyte ions was conducted under these conditions: an ion isolation width of two m/z units and 0.25 q value.

3.3.4 CAD experiments

For typical CAD experiments, the ions of interest were isolated using an isolation width of two m/z units. The activation q value was set to 0.25 when the isolated ions were subjected to CAD (collision energy ranging from 10 to 30 arbitrary units) for 30 ms. Helium was used as the collision gas for these CAD experiments.

3.3.5 Ion-molecule reactions

The reagent, MOP, was introduced into the helium buffer gas line of an external reagent mixing manifold^{21,22} via 500 μL Hamilton syringe at a flow rate of 5 $\mu\text{L}/\text{h}$. The areas surrounding the syringe port were heated to about 70 $^\circ\text{C}$ to ensure that MOP evaporated completely. MOP was then diluted with helium gas and directed into the ion trap by a constant flow of helium gas, controlled by a Granville-Phillips 203 variable leak valve. The q -value of the isolated analyte ion

was 0.25 when conducting ion-molecule reaction experiments. Reaction times used in this study were 300, 500 and 1000 ms.

3.3.6 Computational Studies

Geometry optimizations and single point energy calculations were carried out with Gaussian 16 Program.^{23,24} Calculation of proton affinities was performed at the B3LYP/6-31++G(d,p) level of theory. Erlu Feng provided quantum calculations results for the potential energy surface shown in Figure 3.3. He calculated the optimized molecular structures and their energies using the M06-2X/6-311++G(d,p) level of theory. Stationary points were characterized by frequency calculations to confirm a correct number of imaginary frequencies. All transition state structures were determined to contain exactly one negative frequency. Intrinsic reaction coordinate (IRC) calculations were performed for all transition states to ensure that the optimized structure connected the correct reactants and products.

3.3.7 HPLC/MS and HPLC/MS² experiments

Samples of five FDA-regulated *N*-nitrosamine compounds, *N*-nitrosodimethylamine (NDMA), *N*-nitroso-*N*-methyl-4-aminobutyric (NBMA), *N*-nitrosodiethylamine (NDEA), *N*-nitrosoethylisopropylamine (EIPNA), and *N*-nitrosodiisopropylamine (DIPNA) were injected into Thermo Fisher HPLC via an autosampler with full-loop injection (25 μ L). The column used was an Agilent ZORBAX SB-C18 (5 μ m, 4.6 \times 250 mm). The mobile phases used were water (A) and methanol (B), both containing 0.1% formic acid. The gradient was as follows: 0–1.5 min isocratic elution at 10% B; 0.5–7 min linear increase to 55% B; 7–17 min isocratic hold at 55% B; 17.0–17.1 min linear increase to 90% B; 17.1–20 min isocratic hold at 90% B 20.0–20.1 min return to 10%

B; 20.1–25 min isocratic hold at 10% B. Gradient conditions are expressed in terms of mobile phase B, assuming that the remainder of the composition is mobile phase A. The flow rate and gradient of the mobile phases used was based on previously published literature.¹⁶

3.4 Conclusions

Gas-phase ion–molecule reactions of MOP with eighteen protonated *N*-nitrosamines examined in a LQIT, except for *N*-methyl-*N*-(4-oxo-4-(pyridin-3-yl)butyl)nitrous amide, *N*-nitrosonornicotine and *N*-nitrosoanabasine, are demonstrated to yield a diagnostic product ion, $[M + H + MOP - CH_3C(OH)=CH_2]^+$. Only two false positives, 2-methoxycarboxylic acid and methyl phenyl sulfoxide out of 42 compounds, were observed in this study which demonstrates the robustness of the developed method. These specific compounds can be differentiated from *N*-nitroso functionality by reactions with other neutral reagents such as TDMAB and ITS.

In addition to address the false negative cases, a sequence of ion-molecule reaction with MOP and two CAD experiments was adopted to identify protonated *N*-nitrosamine compounds containing strongly basic pyridine moiety. Protonated *N*-nitrosamine compounds containing strongly basic groups was observed to only form an adduct with MOP. When this adduct is isolated and subjected to CAD, it regenerated the protonated compound. The protonated compound upon a second CAD loses a NO radical. These three experiments enable the identification of *N*-nitrosamine with a pyridine functionality. To ensure the proposed reaction sequence could differentiate protonated *N*-nitrosamines with a pyridine functionality from protonated *O*-nitroso compounds with a pyridine functionality, two such *O*-nitroso compounds were proposed, synthesized, and tested. An additional HN=O loss was observed for protonated *O*-nitroso compounds in the MS⁴ experiments which can be used to differentiate *O*-nitroso compounds from *N*-nitrosamines.

Finally, HPLC/MS and HPLC/MS² experiments (based on ion-molecule reactions) were carried out to determine the LOD of the two methods for five FDA-regulated *N*-nitrosamines. The LOD for the simple HPLC/MS experiments ranged from 0.005 up to 0.1 ppm while that for the HPLC/MS² experiments ranged from 0.0025 up to 0.5 ppm.

A decision tree for this developed method is shown in **Figure 3.11**. Three false negative cases were observed due to these *N*-nitrosamine model compounds containing a pyridine moiety. When examining a large set of compounds containing functionalities other than the *N*-nitroso group, only two false positive results, 2-methoxycarboxylic acid and methyl phenyl sulfoxide, were found. All these findings demonstrate the robustness of the developed method.

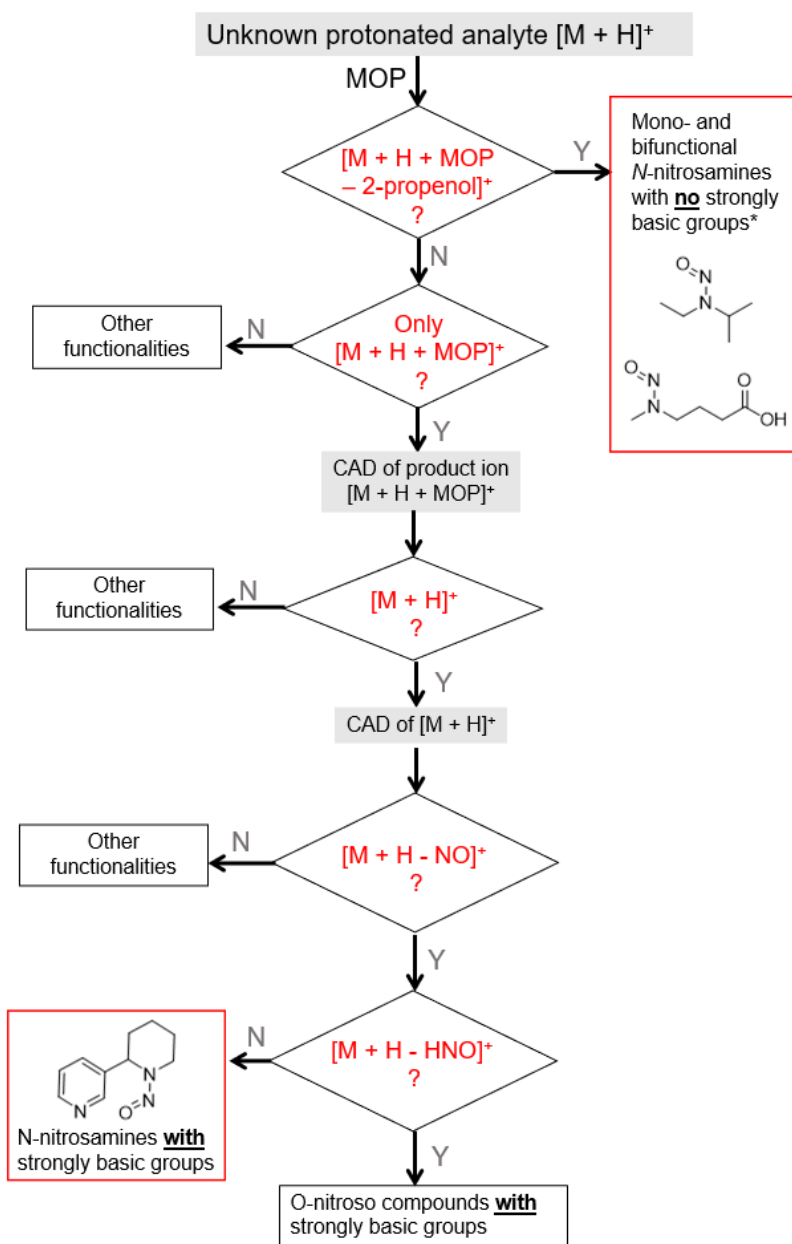


Figure 3.11 Decision tree for the identification of the *N*-nitroso functionality in protonated analytes based on ion-molecule reactions with MOP and CAD experiments.

3.5 References

- (1) Beard, J. C.; Swager, T. M. An Organic Chemist's Guide to *N*-Nitrosamines: Their Structure, Reactivity, and Role as Contaminants. *J. Org. Chem.* **2021**, *86* (3), 2037–2057.
- (2) Farren, N. J.; Ramírez, N.; Lee, J. D.; Finessi, E.; Lewis, A. C.; Hamilton, J. F. Estimated Exposure Risks from Carcinogenic Nitrosamines in Urban Airborne Particulate Matter. *Environ. Sci. Technol.* **2015**, *49* (16), 9648–9656.
- (3) Zhao, Y. Y.; Boyd, J.; Hrudey, S. E.; Li, X. F. Characterization of New Nitrosamines in Drinking Water Using Liquid Chromatography Tandem Mass Spectrometry. *Environ. Sci. Technol.* **2006**, *40* (24), 7636–7641.
- (4) Charrois, J. W. A.; Arend, M. W.; Froese, K. L.; Hrudey, S. E. Detecting *N*-Nitrosamines in Drinking Water at Nanogram per Liter Levels Using Ammonia Positive Chemical Ionization. *Environ. Sci. Technol.* **2004**, *38* (18), 4835–4841.
- (5) Sen, N. P.; Baddoo, P. A.; Seaman, S. W. Nitrosamines in Cured Pork Products Packaged in Elastic Rubber Nettings: An Update. *Food Chem.* **1993**, *47* (4), 387–390.
- (6) Ikeda, K.; Migliorese, K. G. Analysis of Nitrosamines in Cosmetics. *J. Soc. Cosmet. Chem.* **1990**, *41* (5), 283–333.
- (7) Park, J. E.; Seo, J. E.; Lee, J. Y.; Kwon, H. Distribution of Seven *N*-Nitrosamines in Food. *Toxicol. Res.* **2015**, *31* (3), 279–288.
- (8) Raillard, S. P. Control of Genotoxic Impurities: In Active Pharmaceutical Ingredients. *Chim. Oggi* **2012**, *30* (1), 28–30.
- (9) Krietsch Boerner, L. NDMA, a Contaminant Found in Multiple Drugs, Has Industry Seeking Sources and Solutions. *C&EN* **2020**, *98* (15).
- (10) U.S. Food and Drug Administration. Control of Nitrosamine Impurities in Human Drugs. Guidance for Industry *USFDA* **2020**.
- (11) Raoul, S.; Gremaud, E.; Biaudet, H.; Turesky, R. J. Rapid Solid-Phase Extraction Method for the Detection of Volatile Nitrosamines in Food. *J. Agric. Food Chem.* **1997**, *45* (12), 4706–4713.
- (12) Grebel, J. E.; (Mel) Suffet, I. H. Nitrogen-Phosphorus Detection and Nitrogen Chemiluminescence Detection of Volatile Nitrosamines in Water Matrices: Optimization and Performance Comparison. *J. Chromatogr. A* **2007**, *1175* (1), 141–144.
- (13) Breider, F.; Von Gunten, U. Quantification of Total *N*-Nitrosamine Concentrations in Aqueous Samples via UV-Photolysis and Chemiluminescence Detection of Nitric Oxide. *Anal. Chem.* **2017**, *89* (3), 1574–1582.

- (14) Kodamatani, H.; Yamazaki, S.; Saito, K.; Amponsaa-Karikari, A.; Kishikawa, N.; Kuroda, N.; Tomiyasu, T.; Komatsu, Y. Highly Sensitive Method for Determination of *N*-Nitrosamines Using High-Performance Liquid Chromatography with Online UV Irradiation and Luminol Chemiluminescence Detection. *J. Chromatogr. A* **2009**, *1216* (1), 92–98.
- (15) Telling, G. M. The Determination of *N*-Nitrosamines in Foods and Cosmetics. *TrAC Trends Anal. Chem.* **1982**, *1* (12), 277–280.
- (16) Liquid Chromatography-High Resolution Mass Spectrometry (LC-HRMS) Method for the Determination of Six Nitrosamine Impurities in ARB Drugs. *USFDA* **2019**.
- (17) Fine, D. H.; Ruff, F.; Lieb, D.; Rounbehler, D. P. Description of the Thermal Energy Analyzer (TEA) for Trace Determination of Volatile and Nonvolatile *N*-Nitroso Compounds. *Anal. Chem.* **1975**, *47* (7), 1188–1191.
- (18) Parr, M. K.; Joseph, J. F. NDMA Impurity in Valsartan and Other Pharmaceutical Products: Analytical Methods for the Determination of *N*-Nitrosamines. *J. Pharm. Biomed. Anal.* **2019**, *164*, 536–549.
- (19) Busch, K. L.; Glush, G. L.; McLuckey, S. A. Mass Spectrometry/Mass Spectrometry: Techniques and Applications of Tandem Mass Spectrometry. Wiley-VCH. New Jersey. **1989**.
- (20) Liu, J. K.; Alzarini, K. Z.; Niyonsaba, E.; Boulos, V. M.; Yerabolu, R.; Kenttämä, H. I. Determination of the Compound Class and Functional Groups in Protonated Analytes via Diagnostic Gas-Phase Ion-Molecule Reactions. *Mass Spectrom. Rev.* **2021**. Epub ahead of print. PMID: 34435381.
- (21) Gronert, S. Quadrupole Ion Trap Studies of Fundamental Organic Reactions. *Mass Spectrom. Rev.* **2005**, *24* (1), 100–120.
- (22) Habicht, S. C.; Vinuesa, N. R.; Archibold, E. F.; Duan, P.; Kenttämä, H. I. Identification of the Carboxylic Acid Functionality by Using Electrospray Ionization and Ion - Molecule Reactions in a Modified Linear Quadrupole Ion Trap Mass Spectrometer. *Anal. Chem.* **2008**, *80* (9), 3416–3421.
- (23) Gronert, S. Estimation of Effective Ion Temperatures in a Quadrupole Ion Trap. *J. Am. Soc. Mass Spectrom.* **1998**, *9* (8), 845–848.
- (24) Zhao, Y.; Truhlar, D. G. Density Functionals with Broad Applicability in Chemistry. *Acc. Chem. Res.* **2008**, *41* (2), 157–167.
- (25) Sheng, H.; Williams, P. E.; Tang, W.; Zhang, M.; Kenttämä, H. I. Identification of the Sulfoxide Functionality in Protonated Analytes via Ion/Molecule Reactions in Linear Quadrupole Ion Trap Mass Spectrometry. *Analyst* **2014**, *139* (17), 4296–4302.

- (26) Sheng, H.; Tang, W.; Yerabolu, R.; Kong, J. Y.; Williams, P. E.; Zhang, M.; Kenttämä, H. I. Mass Spectrometric Identification of the *N*-Monosubstituted *N*-Hydroxylamino Functionality in Protonated Analytes via Ion/Molecule Reactions in Tandem Mass Spectrometry. *Rapid Commun. Mass Spectrom.* **2015**, 29 (8), 730–734.
- (27) Alzarini, K. Z.; Max, J. P.; Easton, M.; Milton, J. R.; Ma, X.; Dong, X.; Gu, C.; Kenttämä, H. I. Identification of the carboxylic acid functionality in protonated drug metabolite model compounds by using tandem mass spectrometry based on ion-molecule reactions coupled with high performance liquid chromatography. *Int. J. Mass Spectrom.* **2021**, 463, 116551–116561.
- (28) Sheng, H.; Tang, W.; Yerabolu, R.; Max, J.; Kotha, R. R.; Riedeman, J.; Nash, J.; Zhang, M.; Kenttämä, H. I. Identification of N-Oxide and Sulfoxide Functionalities in Protonated Drug Metabolites by Using Ion–Molecule Reactions Followed by Collisionally Activated Dissociation in a Linear Quadrupole Ion Trap Mass Spectrometer. *J. Org. Chem.* **2016**, 81, 575–586.
- (29) Bharate, S. S. Critical Analysis of Drug Product Recalls Due to Nitrosamine Impurities. *J. Med. Chem.* **2021**, 64 (6), 2923–2936.

CHAPTER 4. GRAPH-BASED MACHINE LEARNING INTERPRETS AND PREDICTS DIAGNOSTIC ISOMER-SELECTIVE ION–MOLECULE REACTIONS IN TANDEM MASS SPECTROMETRY

Adapted with permission from Fine, J.; Kuan-Yu Liu, J.; Beck, A.; Alzarieni, K. Z.; Ma, X.; Boulos, V. M.; Kenttämä, H. I.; Chopra, G. *Chem. Sci.* 2020, 11 (43), 11849–11858. Copyright 2019 Chemical Science.

4.1 Introduction

Tandem mass spectrometry (MS^2) based on collision-activated dissociation (CAD) is a common analytical tool that is used to characterize complex mixtures in various fields, such as drug discovery, proteomics, and petroleomics.^{1–4} In these types of experiments, the ionized compounds in the complex mixture are isolated, accelerated and allowed to collide with inert gas, such as helium, within an ion trap or a reaction chamber of the mass spectrometer. A linear quadrupole ion trap mass spectrometer was used in to conduct experiments in this study. Upon multiple collisions within the ion traps, the ions generate fragment ions that can be used for structural elucidation. However, in many cases, identical fragmentation patterns are observed for isomeric ions.^{5,6} A MS^2 approach based on diagnostic, reliable and predictable gas-phase ion–molecule reactions can serve as an alternative to address this issue. In the past, tandem mass spectrometric methods based on diagnostic gas-phase ion-molecule reactions have been adopted to successfully identify different functional groups, including N-oxide, carbamate, sulfone and sulfinyl, in protonated analytes without the need of reference compounds.⁷ To carry out these types of experiments, a commercial ion trap with minor modifications (e.g., addition of an additional reagent inlet system) can be used.^{8,9} Previously, reactions with 2-methoxypropene (MOP) were used to classify several compound classes, including sulfoxides, *N*-oxides and *N,N*-disubstituted hydroxylamines.^{10,11} In these experiments, analytes were protonated via atmospheric pressure

chemical ionization (APCI) in a linear quadrupole ion trap mass spectrometer. The protonated analytes were transferred into the ion trap, isolated and allowed to react with MOP for a specific time period. MOP was continuously introduced into the ion trap via a home-built external reagent inlet system. All ions were ejected in a mass-selective manner from the ion trap into external detectors to determine their m/z values and relative abundances. Branching ratios of the product ions were measured at several different reaction times and were found to be constant over time. Protonated analytes, such as sulfoxides, *N*-oxides and *N,N*-disubstituted hydroxylamines, were classified based on the abundances of the formation of a diagnostic, stable addition product with MOP.^{10,11} As straightforward as this method may seem, with the increase in the number of protonated model compounds whose reactivity is tested towards MOP, interpretation of the data obtained can be challenging and tedious. Therefore, a chemical graph based interpretable machine learning methodology was developed to facilitate data interpretation and the prediction of whether a given protonated analyte will form an abundant diagnostic product ion upon reactions with MOP.

Currently, only a relatively small set of known reactions with MOP exists. Therefore, machine learning approaches that require a large number of known reactions for predicting reaction outcomes, such as multilayer perceptron,^{12,13} Long-Short Term Memory (LSTM)^{14,15} and Graph Convolution Networks (GCN),^{16–19} are not suitable for this study. In addition, results obtained using these machine learning approaches are difficult to interpret and do not provide additional chemical insights. Therefore, a graph-based machine learning methodology, also known as chemical reactivity flowchart, was developed in a collaboration with Dr. Chopra's research group at Purdue University. Chemical reactivity flowcharts can be easily interpreted by humans and do not require large sets of data for prediction.

Prior to the adoption of machine learning approaches, human prediction of the reactivity between the protonated analyte and MOP is usually based on the proton affinity (PA) difference between the analyte and MOP.¹⁰ A proton transfer reaction is usually the dominant reaction if the PA of the analyte is lower than that of MOP. On the other hand, formation of an abundant diagnostic adduct can be observed when the PA of MOP is greater than that of the analyte. However, the PA of MOP being greater than that of the analyte can also lead to the possibility of observing no reactivity between MOP and the protonated analyte. Therefore, graph-based machine learning methodology for accurate prediction of the reactivity between MOP and the analyte is desired and may provide more chemical insights that may not be intuitive to chemists. Nevertheless, PA values still retain their value as a potential source for additional input features or baseline for benchmarking machine learning methods.

4.2 Results and discussion

4.2.1 Choice of the machine learning model

Professor Chopra's group chose the decision tree-based machine learning model for this study as it yields a flowchart of logical decisions that one can use to evaluate the decisions made by the model and as it can be trained successfully based on relatively small data sets. The decision tree-based machine learning model represents analytes as an input bit vector of functional groups, which results in a flow chart diagram that can be interpreted by chemists. Jonathan Fine (Professor Chopra's group) utilized bootstrapping of several decision tree-based machine learning models to ensure robustness of the developed model for prospective experimental validation (see the Methods section in the original publication for details of the development of the model).²⁰

4.2.2 Choice of neutral reagent and diagnostic ion-molecule reaction of interest

The main advantage of selecting MOP as the reagent of interest is that reactions of various protonated analytes containing different functional groups with MOP have been studied previously.^{10,11} Furthermore, identification of specific functional groups via diagnostic reactions with MOP does not require any additional dissociation reaction steps. Diagnostic gas-phase ion-molecule reactions are preferred as training data sets for machine learning models due to their more predictable nature.⁷

The reactivity of 36 protonated analytes towards MOP have been previously studied and published.^{10,11} Experimental outcome of these 36 known reactions was either proton transfer, no reaction, formation of addition product ion followed by the loss of a methanol moiety or the formation of a stable addition product ion. The diagnostic reaction of interest for this study is the formation of a stable addition product ion with MOP. Protonated analytes containing sulfinyl, *N*-oxide and *N,N*-disubstituted hydroxylamino functionalities yielded a stable addition product ion in high abundance with MOP. The abundance of the addition product was expressed via the branching ratio of the adduct, which corresponds to the fraction of the product ions that correspond to the stable adduct. For this study, the set of 36 protonated analytes, the reaction products of the protonated analytes with MOP, and their product branching ratios were used as a training data sets for the decision tree-based machine learning model.

4.2.3 Development of machine learning model with 36 training data sets

36 training data sets are considered a relatively small sets of know reactions with MOP. Therefore, a binary classifier approach was chosen over other machine learning approaches. The definition of binary classification is a task of classifying objects where the output is restricted to two groups. Jonathan Fine generated several decision tree-based machine learning models by

utilizing different diagnostic product branching ratio cutoffs (10%, 20%, 30%, 40%, 50%, 60%, 70% and 90%) as the binary classifier to train these models. Furthermore, each cutoff model was trained utilizing a bootstrapped method to account for inter-model reliability.

4.2.4 Validation of the developed machine learning model

The main objective of this study was to develop a decision tree-based machine learning model that achieves high prediction accuracy based on chemist's criteria of a diagnostic reaction. In previous studies, Sheng et al. utilized gas-phase ion-molecule reactions of MOP to classify compounds into different compound classes, such as sulfoxide, *N*-oxide and *N,N*-disubstituted hydroxylamine.^{10,11} Figure 1 shows a decision tree made from a chemist perspective to classify functional groups based on reactions observed with MOP. Protonated analytes with sulfinyl, *N*-oxide and *N,N*-disubstituted hydroxylamino functional groups reacted with MOP to yield an abundant addition product (branching ratio 37–99%), which was accompanied by a much slower proton transfer reaction. This can be explained via the PA difference between the analytes and MOP. For example, compounds with greater PAs than MOP, such as sulfoxides, showed mainly MOP adduct formation whereas compounds with lower PAs, such as sulfones, showed more proton transfer product.

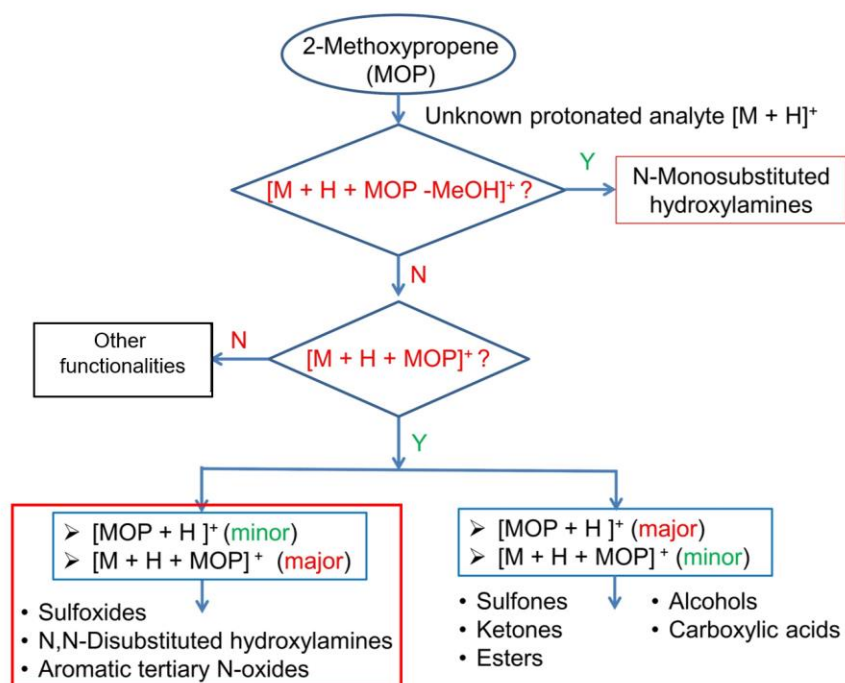


Figure 4.1 Chemist-made decision tree for the classification of functional groups in protonated analytes by using reactions with MOP.

Each cutoff model using different binary classifiers generated by Jonathan Fine was validated using 13 external analytes of unknown experimental outcomes to evaluate its performance. The reaction outcome of each of these analytes was predicted by the different cutoff models. After this task, these 13 analytes were protonated and allowed to react with MOP in the linear quadrupole ion trap mass spectrometer. Replicate measurements were completed with the help of Kawthar Alzarini. The decision of whether the 13 reactions with MOP are diagnostic or not was determined based on the criteria given in the publications of Sheng et al.^{10,11} The experimental results and the predicted reaction outcomes from the cutoff models were compared to evaluate the performance of each model. The decision tree-based model trained using the 70% cutoff as the binary classifier

outperformed the other models. This model correctly predicted the reactivity for 11 of the 13 analytes. Table 1 shows the comparison of the experiment result and the reaction outcome prediction made from all the different decision tree models based on their cutoffs. Further discussion about the performance of the different models from a machine learning perspective can be found in the Results and Discussion section of the original publication.²⁰

Table 4.1. The probability for assignment of a correct reaction for all decision tree models

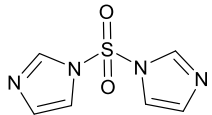
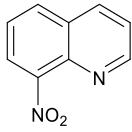
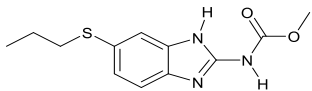
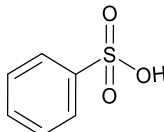
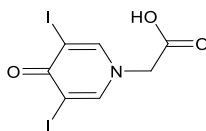
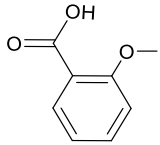
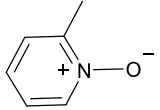
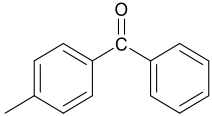
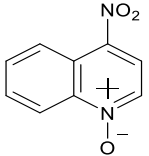
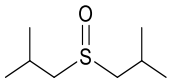
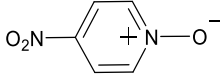
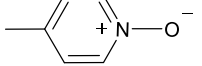
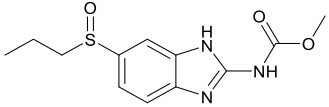
#	Test compound	Formation of Diagnostic product ^a	20%	30%	40%	50%	60%	70%	Proton affinity (kcal/mol)
1		Yes	51%	54%	50%	47%	100%	100%	214.43 ^b
2		No	0%	8%	0%	0%	0%	0%	225.23 ^b
3		No	0%	8%	0%	0%	33%	0%	229.51 ^b
4		No	0%	0%	0%	0%	0%	0%	188.57 ^b
5		No	59%	58%	50%	44%	4%	0%	222.71 ^b

Table 4.1 continued

6		No	0%	0%	0%	0%	33%	0%	195.01 ^b
7		Yes	100%	100%	100%	94%	100%	100%	224.15 ^b
8		No	0%	0%	0%	0%	33%	0%	214.36 ^b
9		No	100%	100%	100%	100%	100%	100%	213.07 ^b
10		Yes	100%	100%	100%	100%	100%	100%	228.46 ^b
11		No	100%	100%	100%	94%	100%	100%	205.64 ^b
12		Yes	100%	100%	100%	88%	100%	100%	226.38 ^b
13		Yes	100%	100%	100%	100%	100%	100%	232.58 ^b
Kappa value		-	0.59	0.59	0.59	0.57	0.72	0.72	0.44

^a See **Figures S2-S14** for assignment of diagnostic production formation ^b Ref. 20

4.2.5 Interpretation of the chemical reactivity flowchart

For interpretability, chemical reactivity flowchart is introduced to rationalize the reasoning behind the selection of the 70% model for making predictions. Figure 2 shows a chemical reactivity flowchart that was automatically generated by the decision tree-based machine learning model with a 70% cutoff as the binary classifier. This flowchart gives features derived from the model based on the connectivity of the atoms in the analytes that enable it to be easily interpreted by chemists and provide the possibility of identifying non-traditional features that are not usually considered by chemists. Furthermore, these derived features can be cross-compared between future machine learning models for different neutral reagents to identify functionalities in unknown analytes.

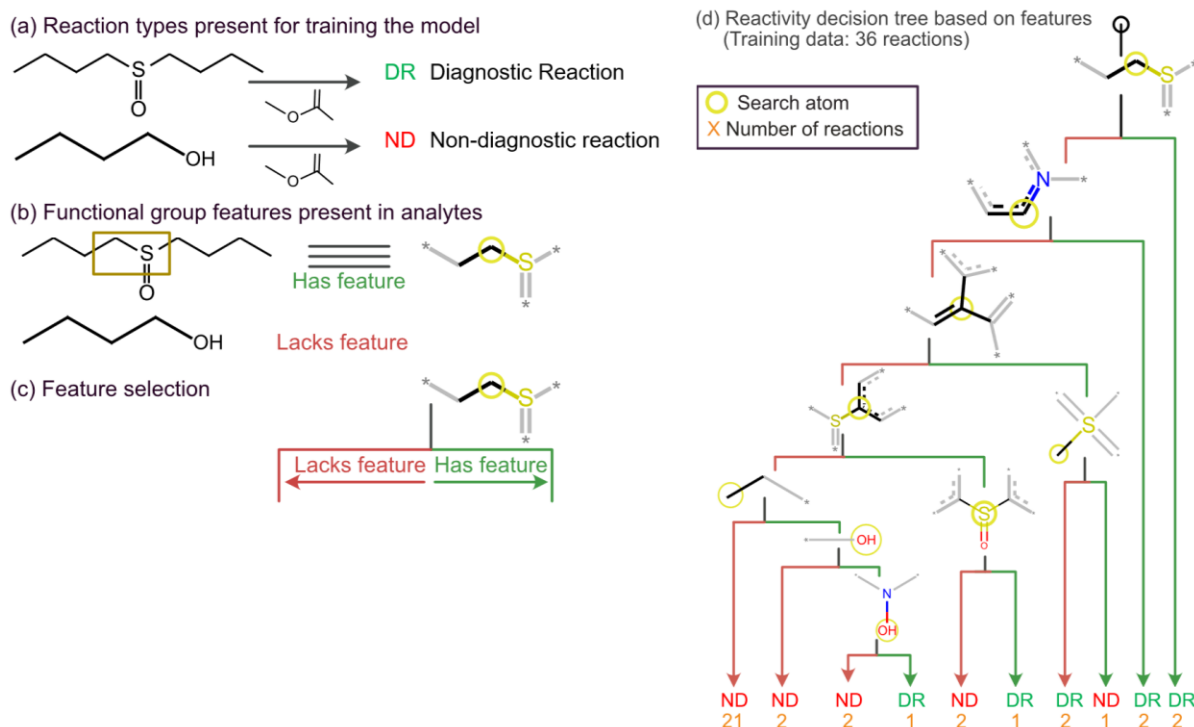


Figure 4.2 Chemical reactivity flowchart. (a) Analytes that undergo diagnostic reaction (DR) or that do not (ND). (b) Compounds identified as having a specific functional group feature (left), such as a sulfonyl with at least one aliphatic carbon atom bound to it (right). No structure is shown when the feature (sulfonyl) is absent in a molecule that does not form a DP. (c) Flowchart for decision making based on the presence or absence of the feature (sulfonyl). (d) The decision tree model trained on a diagnostic product branching ratio cutoff of 70%. The model classifies analytes as reactive or unreactive towards MOP based on their functional groups determined by the Morgan algorithm with a radius of 1 atom.

The decision presented in the chemical reactivity flowchart is the determination of a presence of a sulfinyl functionality with at least one aliphatic carbon atom bound to it in the analyte and, if present, the analyte is assigned as undergoing “diagnostic reaction” (DR) with MOP (see Fig. 4d). Then, if the sulfinyl functionality is not present, the second decision of the flowchart is the determination of a presence the second feature which contains a nitrogen atom with three substituents in a heteroaromatic ring (note that dashed lines indicate an aromatic bond) and assigns the analyte as undergoing “DR” with MOP if such an atom is present. If neither feature is present in the analyte, the following decision of the flowchart is the determination of a presence of a

junction between sp^2 hybridized atoms and assigns analytes containing this feature as undergoing “DR” with MOP. To note here, the feature representing a junction between sp^2 hybridized atoms is a non-traditional feature that chemists do not usually consider as a functional group due to the lack of heteroatoms. This non-traditional feature showcases the ability of machine learning to provide chemical insights. If this feature is not present, the model checks for a sulfinyl group located next to one or more aromatic rings and assigns the analyte as undergoing “DR” with MOP if the sulfinyl group is between two aromatic rings. After this, the following decision of the flowchart is the determination of a presence of a terminal carbon bound to any atom and assigns all analytes lacking this functionality as undergoing “non-diagnostic reaction” with MOP. Those analytes that contain this functionality are checked for terminal oxygens or carbonyl groups and compounds lacking these functionalities are checked for a hydroxylamino group for final “diagnostic reactivity” assignment. It should be noted that some of the features in the chemical reactivity flowchart generated by the model shows certain resemblance to the chemist-made decision tree shown in Figure 1. As mentioned above, a fast diagnostic addition reaction with MOP is observed for sulfoxides, *N*-oxides and *N,N*-disubstituted hydroxylamines. In the chemical reactivity flowchart, which was automatically generated by the machine learning model, we can also observe similar features as in sulfoxides, *N*-oxides and hydroxylamines.

Regarding the validation performance, the model correctly predicted the two test sulfoxide compounds (#10 and #13 in Table 1) in the test set to undergo “diagnostic reaction” with MOP. Similarly, the model predicted that analytes containing an *N*-oxide functionality undergo “diagnostic reaction” with MOP (#7, #9, #11, and #12). However, experimental results show that compounds containing nitro groups (#9 and #11) do not undergo a diagnostic reaction with MOP. These two compounds represented the only two errors made by the 70% cutoff model and these

failures may be due to a nitro group not being present in the analytes in the training set. From a chemists' perspective, even though protonated *N*-oxides have been reported to undergo the diagnostic reaction with MOP, the addition of the nitro group, an electron withdrawing substituent, at the *para*-position lowers the proton affinity of the analyte. When the PA of the analyte is lower than that of MOP, a proton transfer reaction is usually the dominant reaction. If the reactivity prediction had utilized proton affinities, these two nitro compounds would have been correctly predicted as “non-diagnostic reaction”. This finding suggests that when new functional groups are added into the model, a proton affinity verification step would be useful to ensure that the new reaction predictions are correct.

4.2.6 Retraining the decision tree model on new reactions

One of the advantages of utilizing a machine learning methodology is that the models have the capability of being retrained and improved by the incorporation of new data. A new model that was trained with the addition of 13 analytes to the initial 36 analytes in the training set is shown in Fig. 3. The introduction of new data did not cause extensive changes to the chemical features in the decision tree model, which indicates that the initial model was robust. Further, the new 49-analyte training set introduced four additional features, three of which are related to the nitro group present in two of the new analytes, 4-nitropyridine *N*-oxide and 4-nitroquinoline *N*-oxide. Therefore, one can deduce that the model has added an additional comparison to prevent these compounds from being predicted as undergoing “DR” with MOP. As more protonated analytes with known reactivities towards MOP are identified, this model can be retrained to incorporate these new analytes, yielding improved predictions in the future while retaining baseline performance and simplicity.

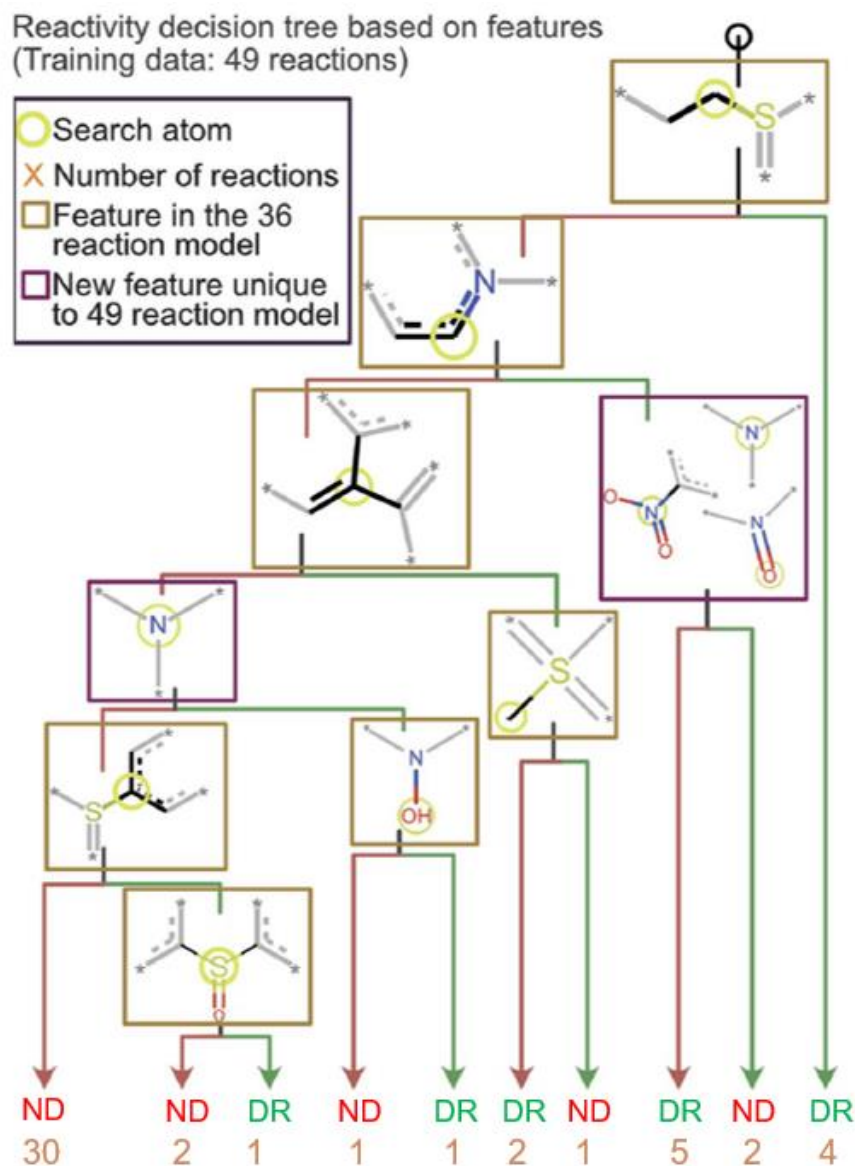


Figure 4.3 The decision tree model obtained by retraining the first model by using the 70% cutoff and all 49 reactions (original 36 and new 13 test reactions). This model is similar to the one obtained via a training set of 36 reactions but has an additional check for a nitro group which was not included in the original model. The lack of any major changes from the model shown in Figure 4.2 indicates that the final model is robust and is able to incorporate new functional groups.

4.3 Experimental

4.3.1 APCI MS method

All experiments were performed using a Thermo Fisher Scientific LTQ XL linear quadrupole ion trap (LQIT) mass spectrometer equipped with an atmospheric pressure chemical ionization (APCI) source and operated in positive ion mode. Sample solutions in methanol were prepared at concentrations ranging from 0.01 to 1 mg/mL. The solutions were injected into the APCI source with a 500 μ L Hamilton syringe at the flow rate of 15 μ L/min. Nitrogen gas was used as the sheath and auxiliary gas with flow rates of 30 and 10 arbitrary units, respectively. The vaporizer and capillary temperatures were 300 °C and 275°C, respectively. The ions generated upon APCI were transferred into the ion trap via the ion optics. The voltages applied to the ion optics were optimized for each protonated analyte via the tune feature of the LTQ Tune Plus interface. Thermo Xcalibur Qual Browser 2.2 SP1.48 was used to process and analyze data.

4.3.2 Ion-molecule reaction conditions

The neutral reagent, MOP, was introduced via a syringe pump operating at a rate of 5 mL/h into helium buffer gas line of an external reagent mixing manifold.^{8,9} To ensure that MOP evaporated completely, the surrounding areas of the syringe port were heated to about 120 °C. MOP was then diluted <with helium? and directed into the ion trap by a constant flow of helium gas, controlled by a leak valve. Protonated analytes in the ion trap were isolated using an isolation width of 2 m/z units and a q value of 0.25 and then allowed to react with MOP in the ion trap for up to 10,000 ms. After this, all ions were detected by ejecting them in a mass-selective manner into two external electron multipliers. The MS^2 spectra measured for the 13 new analytes are given in Figures 4–16 for a specific reaction time. The diagnostic product branching ratio corresponds

to the fraction of $[\text{analyte} + \text{H} + \text{MOP}]^+$ product ions relative to all product ions generated. These values were measured at several reaction times and found to be constant with time as no secondary reactions took place. The reproducibility of these measurements was found to be better than 10%. Other potential product ions are $[\text{MOP} + \text{H}]^+$ and $[\text{analyte} + \text{H} + \text{MOP} - \text{MeOH}]^+$.

The average branching ratios were obtained by calculating the mean of the branching ratios of each product ion tested in different days. The standard deviation of the branching ratios of the most abundant product ion formed in each reaction tested on different days were obtained using the equation shown below:

$$\text{Sample standard deviation} = \sqrt{\frac{1}{N-1} \sum_{i=1}^N (x_i - \bar{x})^2}$$

N : number of days

x_i : the observed branching ratio for the most abundant product ion

\bar{x} : the mean value of the branching ratios for the most abundant product ion

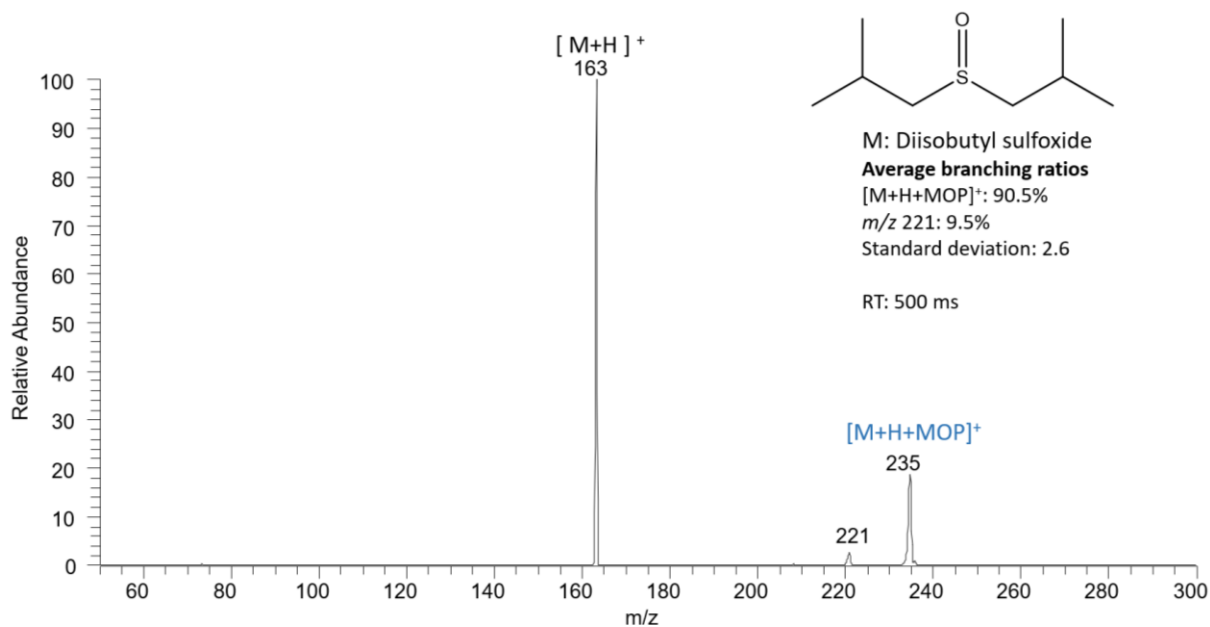


Figure 4.4 MS/MS spectrum measured after 500 ms reaction of protonated diisobutyl sulfoxide with MOP, indicating the formation of a diagnostic addition product ($M+HMOP$).

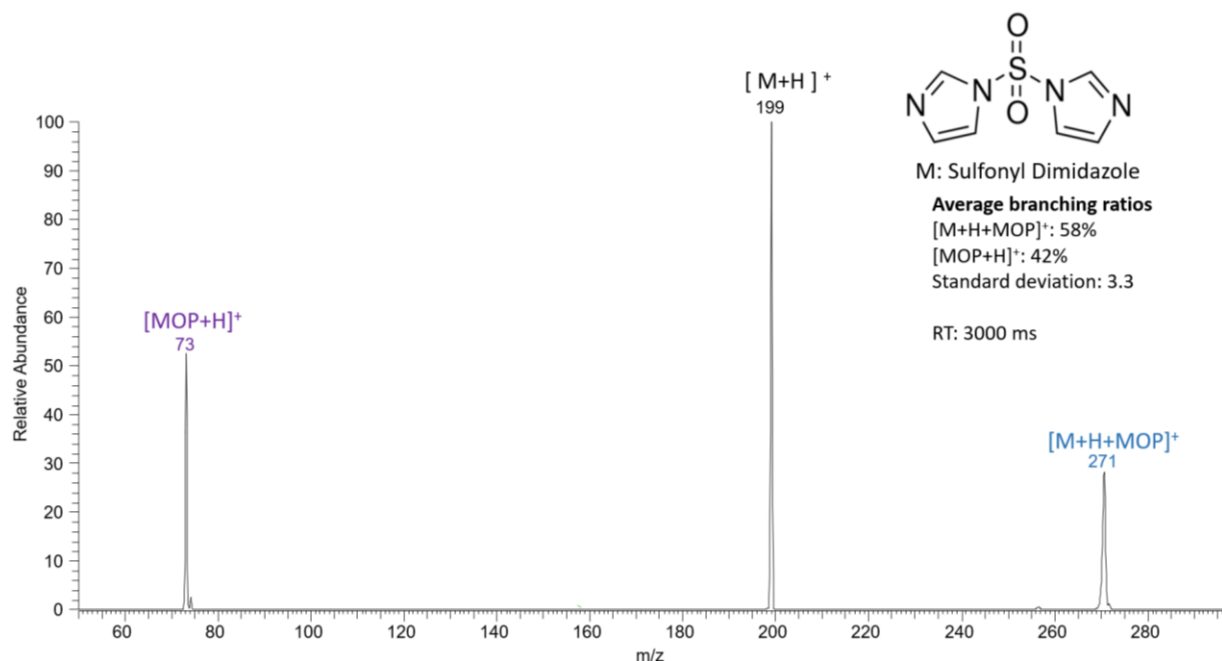


Figure 4.5 MS/MS spectrum measured after 3,000 ms reaction of protonated sulfonyl dimidazole with MOP, indicating the formation of a diagnostic addition product.

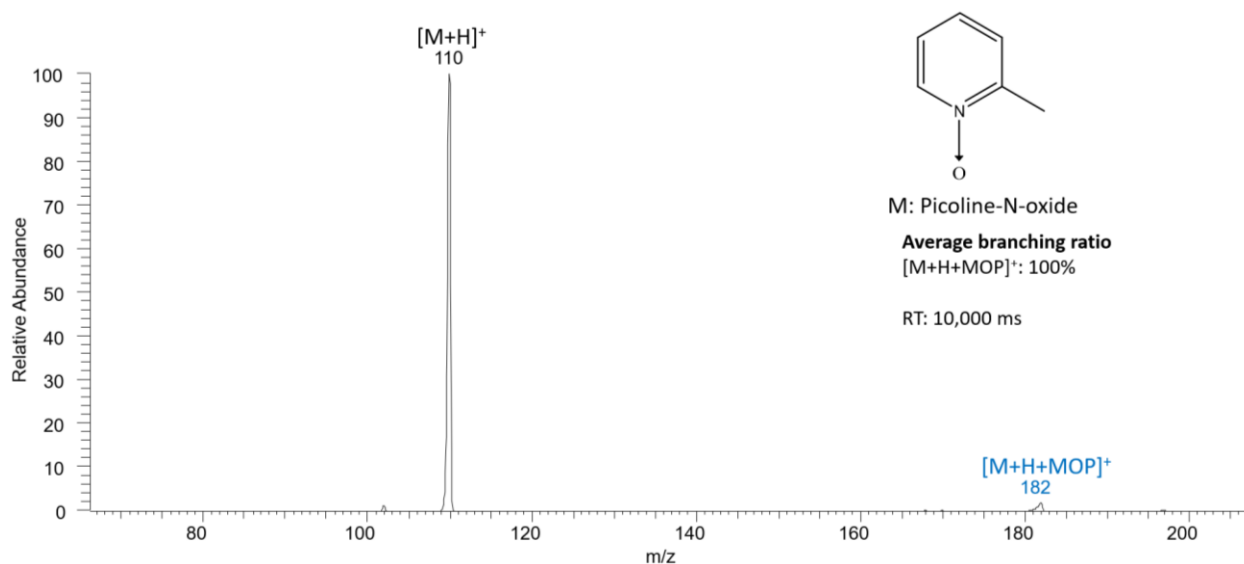


Figure 4.6 MS/MS spectrum measured after 10,000 ms reaction of protonated picoline N-oxide with MOP, indicating the formation of a diagnostic addition product. No proton transfer product was observed.

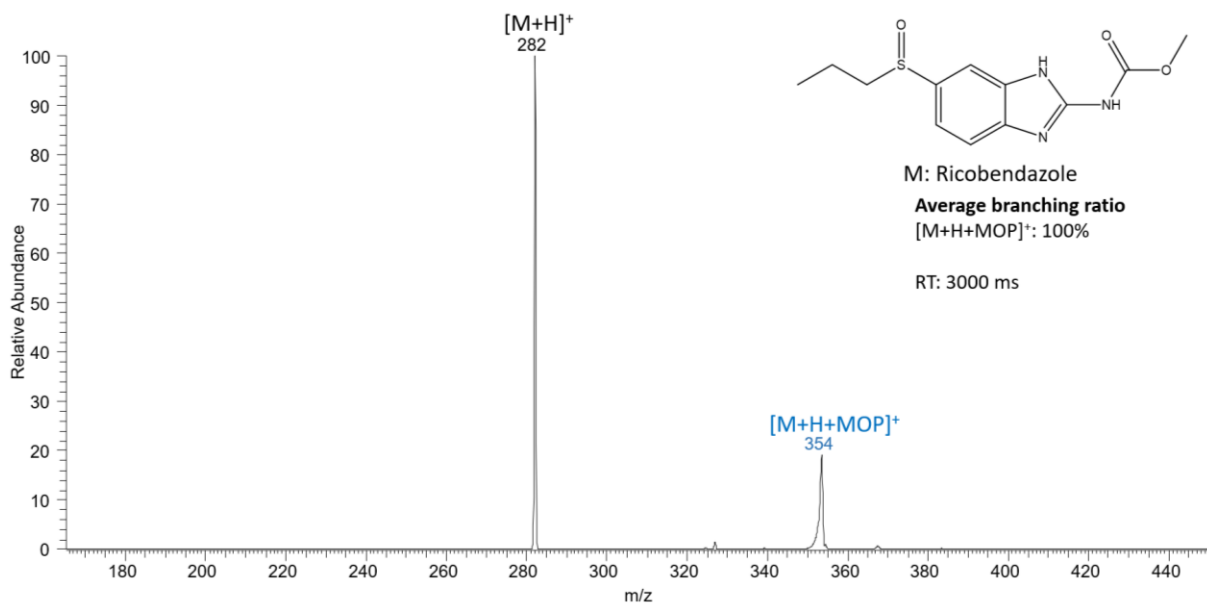


Figure 4.7 MS/MS spectrum measured after 3000 ms reaction of protonated ricobendazole with MOP, indicating the formation of a diagnostic addition product. No proton transfer product was observed.

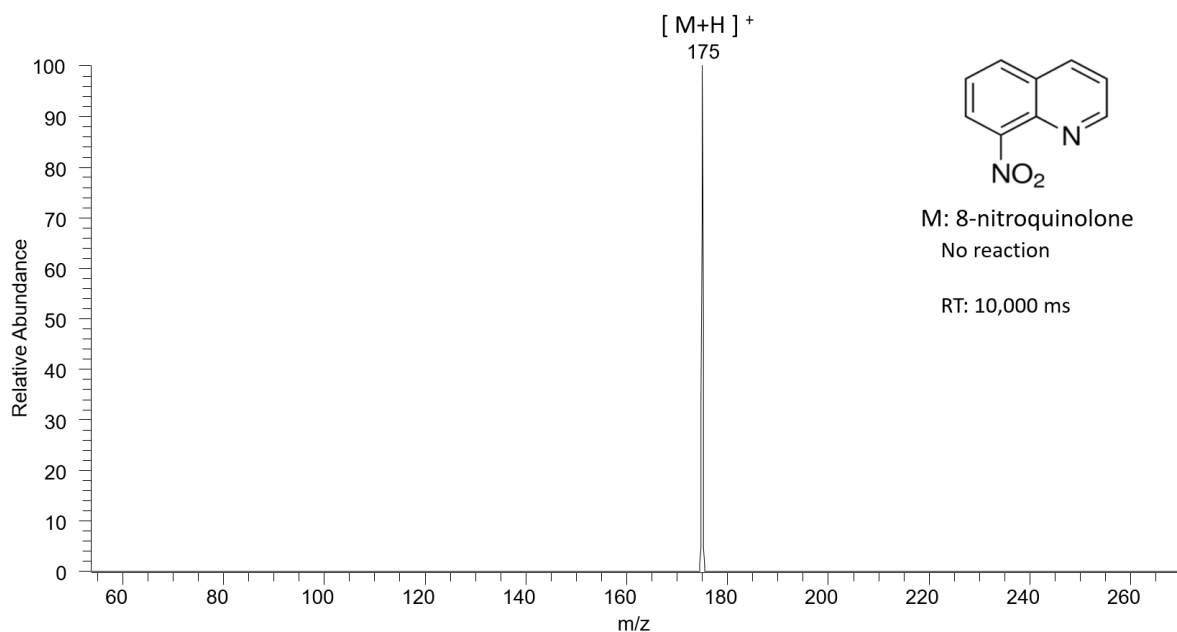


Figure 4.8 MS/MS spectrum measured after 10,000 ms reaction of protonated 8-nitroquinolone with MOP, indicating that no diagnostic addition product was formed. No proton transfer product was formed, either.

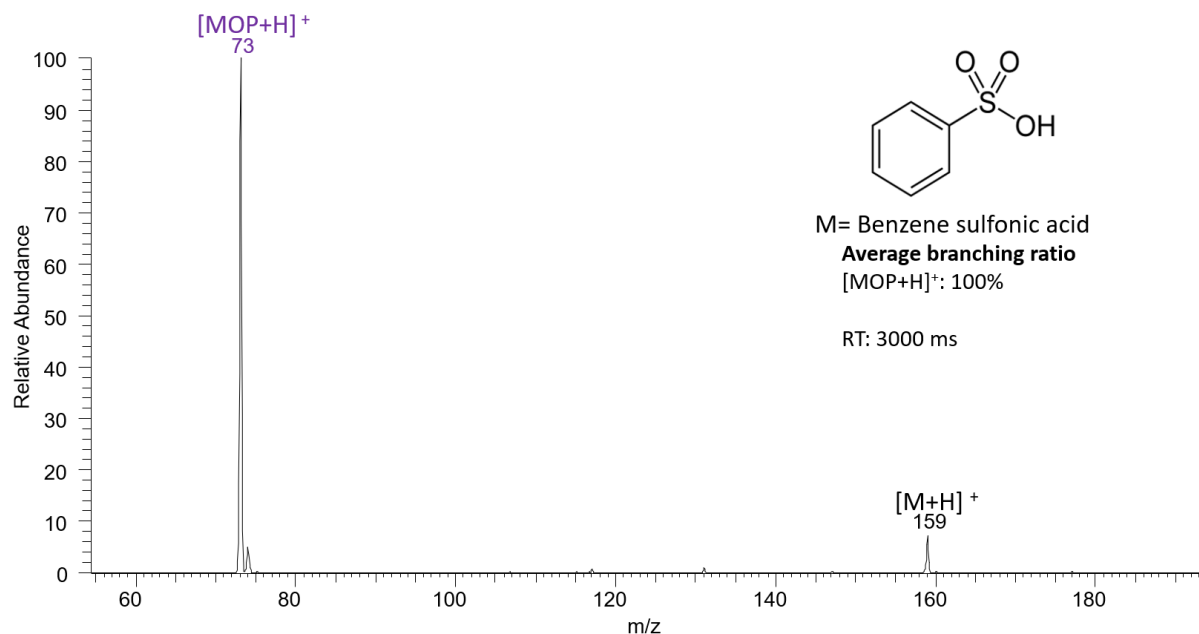


Figure 4.9 MS/MS spectrum measured after 3,000 ms reaction of protonated benzene sulfonic acid with MOP, indicating that a diagnostic addition product was not formed. Instead, a proton transfer product (MOP+H) was observed.

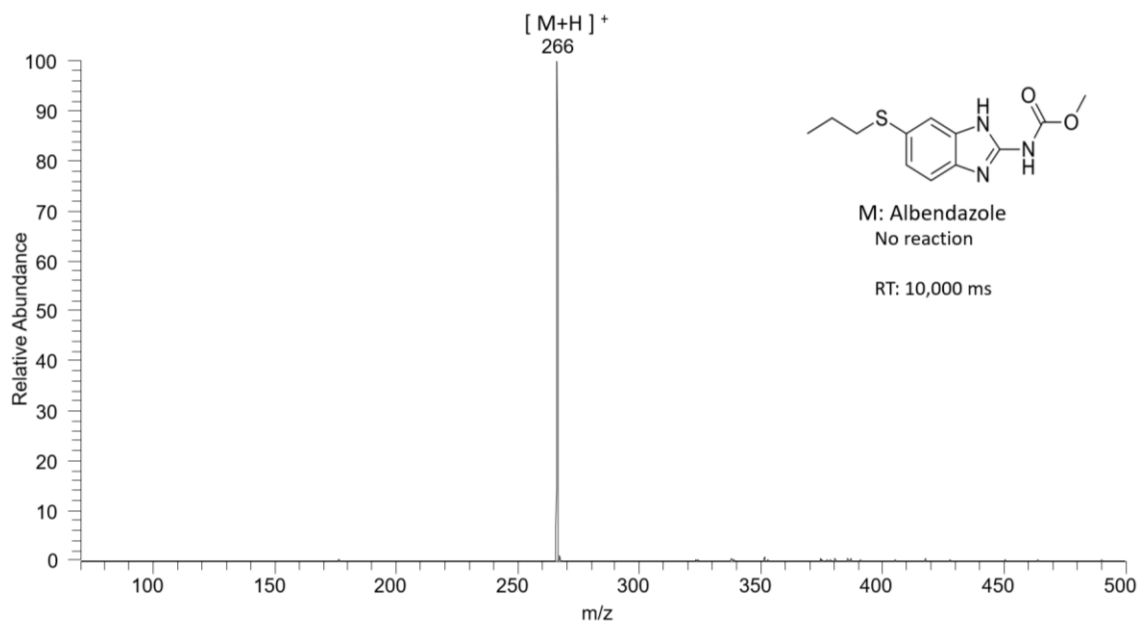


Figure 4.10 MS/MS spectrum measured after 10,000 ms reaction of protonated albendazole with MOP, indicating that a diagnostic addition product was not formed. No proton transfer product was observed, either.

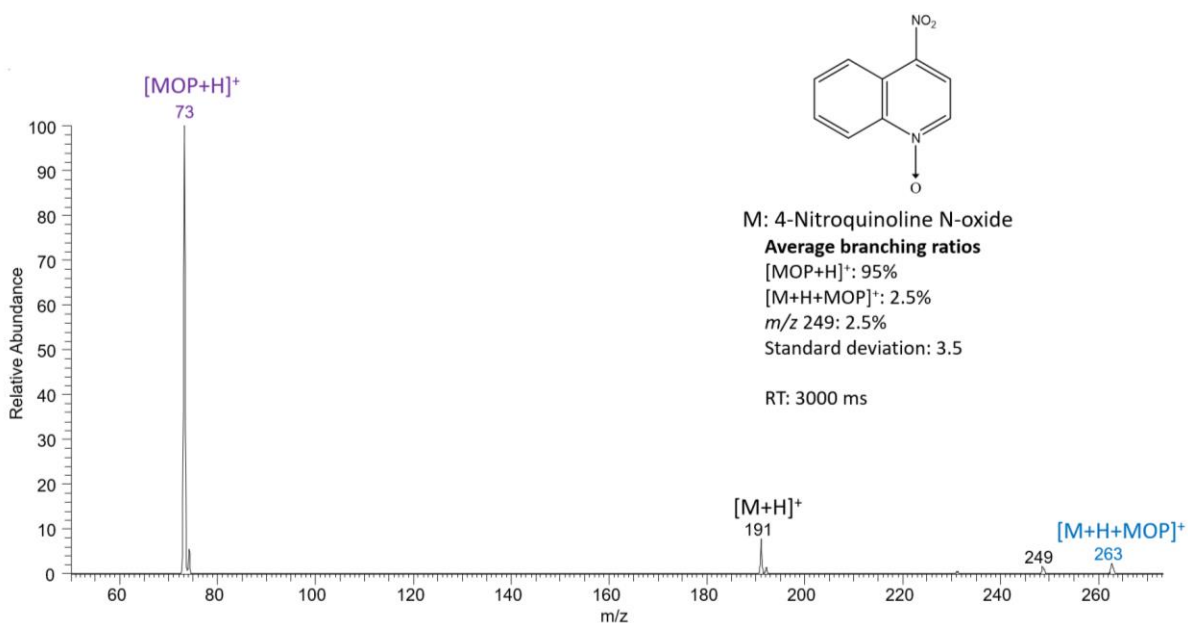


Figure 4.11 MS/MS spectrum measured after 3,000 ms reaction of protonated 4-nitroquinoline N-oxide with MOP. Although evidence of a diagnostic addition product is seen, the presence of a major proton transfer product indicates that this reaction is not suitable for diagnostic applications.

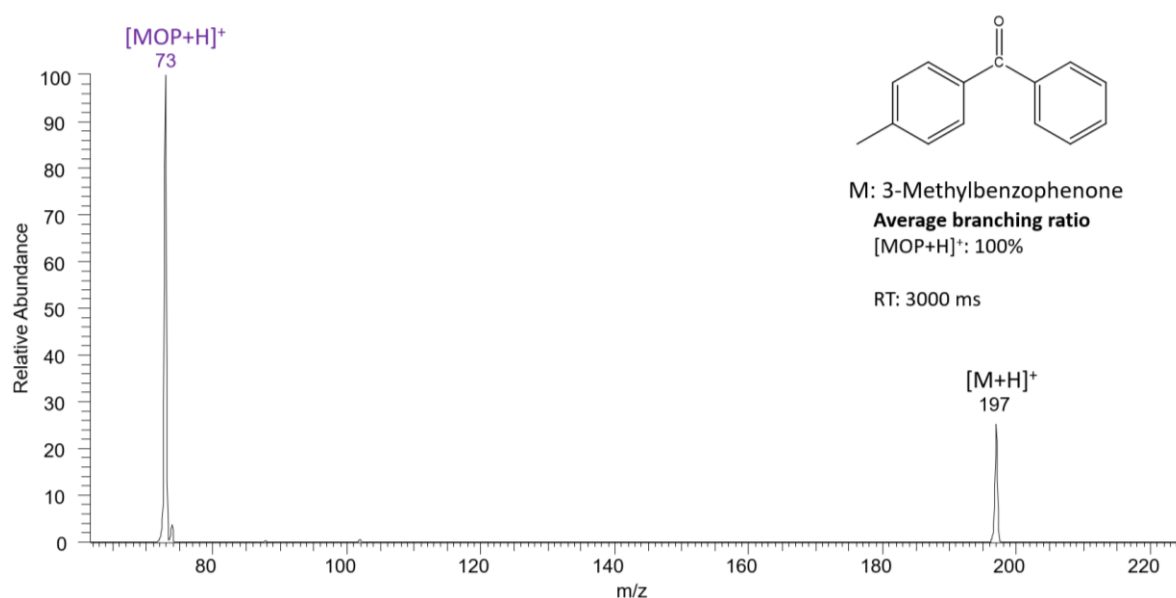


Figure 4.12 MS/MS spectrum measured after 3,000 ms reaction of protonated 3-methylbenzophenone with MOP, indicating that a diagnostic addition product was not formed. Instead, a proton transfer product was observed.

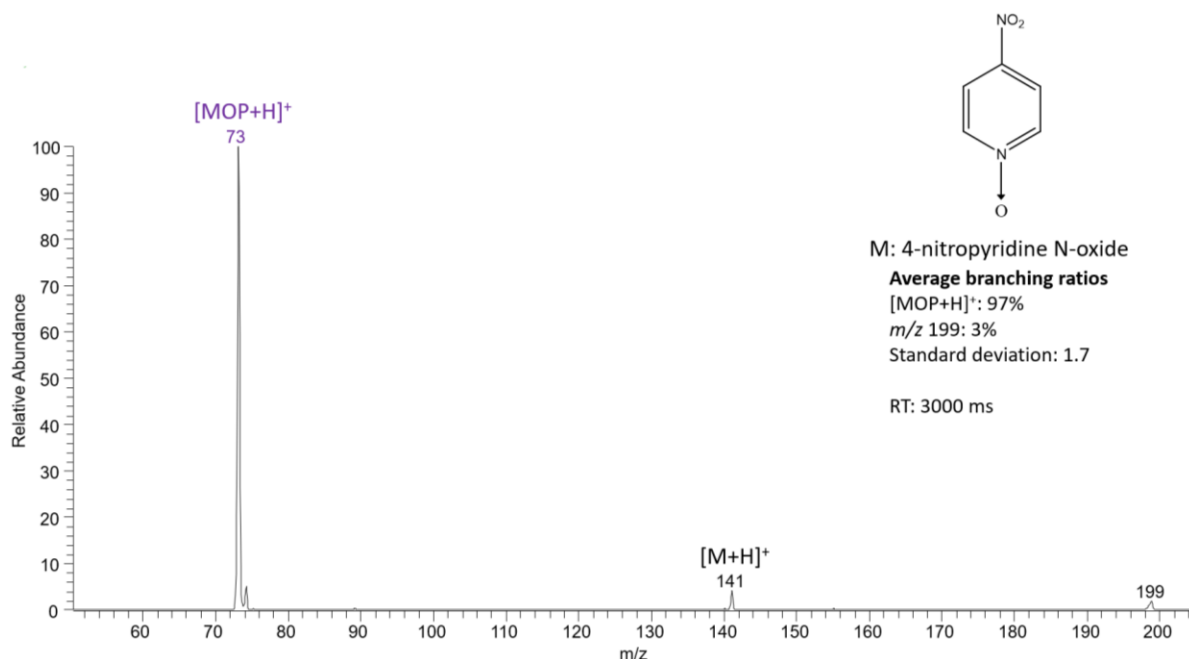


Figure 4.13 MS/MS spectrum measured after 3,000 ms reaction of protonated 4-nitropyridine N-oxide with MOP, indicating that a diagnostic addition product was not formed. Instead, a proton transfer product was observed.

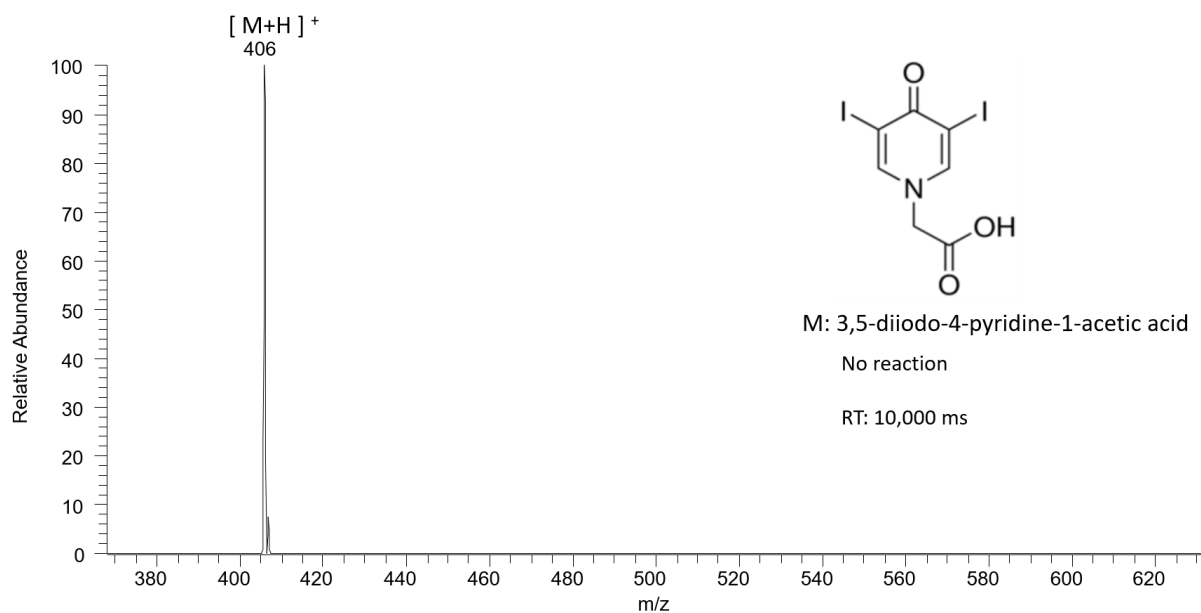


Figure 4.14 MS/MS spectrum measured after 10,000 ms reaction of protonated 3,5-diiodo-4-pyridine-1-acetic acid with MOP, indicating that a diagnostic addition product was not formed. No proton transfer product was observed, either.

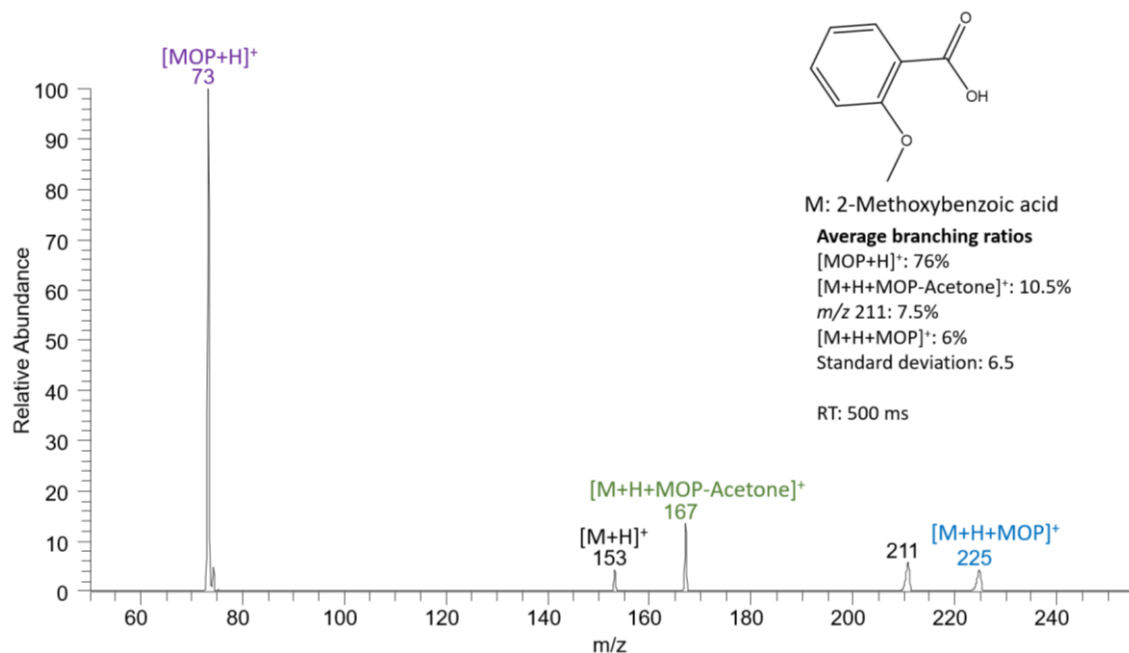


Figure 4.15 MS/MS spectrum measured after 500 ms reaction of protonated 2-methoxybenzoic acid with MOP. Although evidence of a diagnostic addition product is seen, the presence of a major proton transfer product indicates that this reaction is not suitable for diagnostic applications.

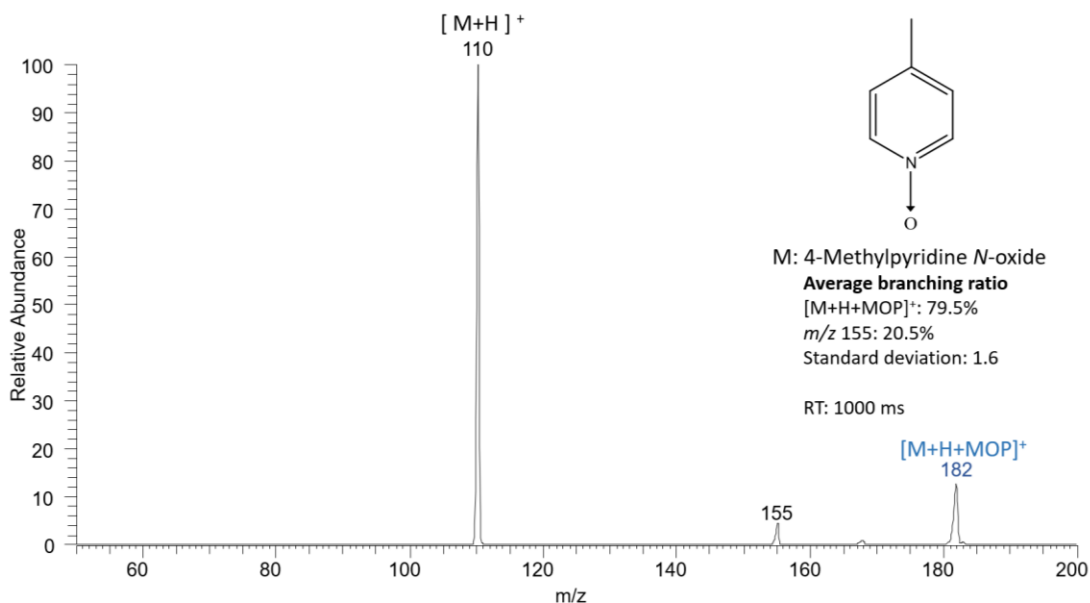


Figure 4.16 MS/MS spectrum measured after 1000 ms reaction of protonated 4-methylpyridine *N*-oxide with MOP, indicating the formation of a diagnostic addition product. No proton transfer product was observed.

4.4 Conclusions

The work presented here demonstrated that a combination of machine learning and tandem mass spectrometry experiments based on diagnostic gas-phase ion-molecule reactions with MOP can be used to predict reaction outcomes for protonated analytes containing specific functional groups in a semiautomated fashion while generating results in a manner readily understandable to chemists. Identification of specific functional groups within an unknown analyte can be facilitated when more machine learning models based on reactions of different neutral reagents have been developed. This decision tree-based machine learning methodology *trained on a relatively small training set of only 36 analytes* was validated using 13 external analytes of unknown experimental outcomes. The model correctly predicted the reactivity for 11 of the 13 analytes present in the test set, and 13 of 13 analytes. In addition, the machine learning based decision tree model is easily interpretable by humans using the chemical reactivity flowcharts shown in this work. Additionally, the inclusion of new data resulted in only minor changes to the model as opposed to the creation of an entirely new model, which suggests a robust selection of chemical features.

Over the years, many different reagents have been developed for the identification of various functionalities in protonated analytes. Chemical diversity in the reagents results in increased reliability of the identification.⁷ In addition to more reagents being developed every year, recent development of an external reagent inlet system composed of nine pulsed valves allows rapid, consecutive introduction of nine reagents to react with each analyte.²¹ This nine-pulsed valve system integrated to a LQIT mass spectrometer can also be coupled to HPLC. Therefore, nine reagents and many analytes can be tested in a single HPLC run.

The methodologies presented herein will pave the way for expanding the above MS2 method to include new diagnostic reactions for the identification of many different functionalities in an easy, accurate, and automated manner. The ultimate goal of this research is to develop

methodology for the fast determination of unknown isomeric drug metabolites via the identification of diagnostic product ions formed upon reactions of the protonated metabolites with selected neutral reagents. In the future, a fully automated pipeline for mixture component identification incorporating multiple models similar to the one presented here will be showcased along with how this methodology can be used to aid in the development of new therapeutics. The detailed output of all machine learning models is given in the **Supporting Information** of the original publication.²⁰

4.5 References

- (1) Belas, F. J.; Blair, I. A. Mass Spectrometry in Pharmaceutical Analysis. *J. Liposome Res.* **2001**, *11* (4), 309–342. <https://doi.org/10.1081/LPR-100108611>.
- (2) Han, X.; Aslanian, A.; Yates, J. R. Mass Spectrometry for Proteomics. *Curr. Opin. Chem. Biol.* **2008**, *12* (5), 483–490. <https://doi.org/10.1016/j.cbpa.2008.07.024>.
- (3) Marshall, A. G.; Rodgers, R. P. Petroleomics: Chemistry of the Underworld. *Proc. Natl. Acad. Sci.* **2008**, *105* (47), 18090–18095. <https://doi.org/10.1073/pnas.0805069105>.
- (4) Niyonsaba, E.; Manheim, J. M.; Yerabolu, R.; Kenttämä, H. I. Recent Advances in Petroleum Analysis by Mass Spectrometry. *Anal. Chem.* **2019**, *91* (1), 156–177. <https://doi.org/10.1021/acs.analchem.8b05258>.
- (5) Kong, J. Y.; Yu, Z.; Easton, M. W.; Niyonsaba, E.; Ma, X.; Yerabolu, R.; Sheng, H.; Jarrell, T. M.; Zhang, Z.; Ghosh, A. K.; Kenttämä, H. I. Differentiating Isomeric Deprotonated Glucuronide Drug Metabolites via Ion/Molecule Reactions in Tandem Mass Spectrometry. *Anal. Chem.* **2018**, *90* (15), 9426–9433. <https://doi.org/10.1021/acs.analchem.8b02083>.
- (6) Zhang, M.; Eismann, R.; Kenttämä, H.; Xiong, H.; Wu, Y.; Burdette, D.; Urbanek, R. Identification of 2-Aminothiazolobenzazepine Metabolites in Human, Rat, Dog, and Monkey Microsomes by Ion-Molecule Reactions in Linear Quadrupole Ion Trap Mass Spectrometry. *Drug Metab. Dispos.* **2015**, *43* (3), 358–366. <https://doi.org/10.1124/dmd.114.061978>.
- (7) Liu, J. K.; Niyonsaba, E.; Alzarini, K. Z.; Boulos, V. M.; Yerabolu, R.; Kenttämä, H. I. Determination of the Compound Class and Functional Groups in Protonated Analytes via Diagnostic Gas-phase Ion-molecule Reactions. *Mass Spectrom. Rev.* **2021**, mas.21727. <https://doi.org/10.1002/mas.21727>.

- (8) Habicht, S. C.; Vinueza, N. R.; Archibold, E. F.; Duan, P.; Kenttämä, H. I. Identification of the Carboxylic Acid Functionality by Using Electrospray Ionization and Ion–Molecule Reactions in a Modified Linear Quadrupole Ion Trap Mass Spectrometer. *Anal. Chem.* **2008**, *80* (9), 3416–3421. <https://doi.org/10.1021/ac800002h>.
- (9) Gronert, S. Estimation of Effective Ion Temperatures in a Quadrupole Ion Trap. *J. Am. Soc. Mass Spectrom.* **1998**, *9* (8), 845–848. [https://doi.org/10.1016/S1044-0305\(98\)00055-5](https://doi.org/10.1016/S1044-0305(98)00055-5).
- (10) Sheng, H.; Williams, P. E.; Tang, W.; Zhang, M.; Kenttämä, H. I. Identification of the Sulfoxide Functionality in Protonated Analytes via Ion/Molecule Reactions in Linear Quadrupole Ion Trap Mass Spectrometry. *The Analyst* **2014**, *139* (17), 4296–4302. <https://doi.org/10.1039/C4AN00677A>.
- (11) Sheng, H.; Tang, W.; Yerabolu, R.; Kong, J. Y.; Williams, P. E.; Zhang, M.; Kenttämä, H. I. Mass Spectrometric Identification of the N-Monosubstituted N-Hydroxylamino Functionality in Protonated Analytes via Ion/Molecule Reactions in Tandem Mass Spectrometry. *Rapid Commun. Mass Spectrom.* **2015**, *29* (8), 730–734. <https://doi.org/10.1002/rcm.7154>.
- (12) Wei, J. N.; Duvenaud, D.; Aspuru-Guzik, A. Neural Networks for the Prediction of Organic Chemistry Reactions. *ACS Cent. Sci.* **2016**, *2* (10), 725–732. <https://doi.org/10.1021/acscentsci.6b00219>.
- (13) Gómez-Bombarelli, R.; Wei, J. N.; Duvenaud, D.; Hernández-Lobato, J. M.; Sánchez-Lengeling, B.; Sheberla, D.; Aguilera-Iparraguirre, J.; Hirzel, T. D.; Adams, R. P.; Aspuru-Guzik, A. Automatic Chemical Design Using a Data-Driven Continuous Representation of Molecules. *ACS Cent. Sci.* **2018**, *4* (2), 268–276. <https://doi.org/10.1021/acscentsci.7b00572>.
- (14) Müller, A. T.; Hiss, J. A.; Schneider, G. Recurrent Neural Network Model for Constructive Peptide Design. *J. Chem. Inf. Model.* **2018**, *58* (2), 472–479. <https://doi.org/10.1021/acs.jcim.7b00414>.
- (15) Liu, B.; Ramsundar, B.; Kawthekar, P.; Shi, J.; Gomes, J.; Luu Nguyen, Q.; Ho, S.; Sloane, J.; Wender, P.; Pande, V. Retrosynthetic Reaction Prediction Using Neural Sequence-to-Sequence Models. *ACS Cent. Sci.* **2017**, *3* (10), 1103–1113. <https://doi.org/10.1021/acscentsci.7b00303>.
- (16) Engkvist, O.; Norrby, P.-O.; Selmi, N.; Lam, Y.; Peng, Z.; Sherer, E. C.; Amberg, W.; Erhard, T.; Smyth, L. A. Computational Prediction of Chemical Reactions: Current Status and Outlook. *Drug Discov. Today* **2018**, *23* (6), 1203–1218. <https://doi.org/10.1016/j.drudis.2018.02.014>.
- (17) Coley, C. W.; Barzilay, R.; Green, W. H.; Jaakkola, T. S.; Jensen, K. F. Convolutional Embedding of Attributed Molecular Graphs for Physical Property Prediction. *J. Chem. Inf. Model.* **2017**, *57* (8), 1757–1772. <https://doi.org/10.1021/acs.jcim.6b00601>.

- (18) Coley, C. W.; Green, W. H.; Jensen, K. F. Machine Learning in Computer-Aided Synthesis Planning. *Acc. Chem. Res.* **2018**, *51* (5), 1281–1289. <https://doi.org/10.1021/acs.accounts.8b00087>.
- (19) Kearnes, S.; McCloskey, K.; Berndl, M.; Pande, V.; Riley, P. Molecular Graph Convolutions: Moving beyond Fingerprints. *J. Comput. Aided Mol. Des.* **2016**, *30* (8), 595–608. <https://doi.org/10.1007/s10822-016-9938-8>.
- (20) Fine, J.; Kuan-Yu Liu, J.; Beck, A.; Alzarini, K. Z.; Ma, X.; Boulos, V. M.; Kenttämä, H. I.; Chopra, G. Graph-Based Machine Learning Interprets and Predicts Diagnostic Isomer-Selective Ion–Molecule Reactions in Tandem Mass Spectrometry. *Chem. Sci.* **2020**, *11* (43), 11849–11858. <https://doi.org/10.1039/D0SC02530E>.
- (21) Kong, J. Y.; Hilger, R. T.; Jin, C.; Yerabolu, R.; Zimmerman, J. R.; Replogle, R. W.; Jarrell, T. M.; Easterling, L.; Kumar, R.; Kenttämä, H. I. Integration of a Multichannel Pulsed-Valve Inlet System to a Linear Quadrupole Ion Trap Mass Spectrometer for the Rapid Consecutive Introduction of Nine Reagents for Diagnostic Ion/Molecule Reactions. *Anal. Chem.* **2019**, *91* (24), 15652–15660. <https://doi.org/10.1021/acs.analchem.9b03768>.

CHAPTER 5. CHEMICAL CHARACTERIZATION OF THE BORON-CENTERED RADICAL DIANION $[\text{B}_{12}\text{I}_{11}]^{2\cdot-}$ IN THE GAS PHASE

5.1 Introduction

Controlled bond formation with highly reactive molecules is challenging but can provide a solution for the conversion of inert chemical waste or abundant feedstock into valuable products.¹⁻⁴ Unfortunately, the stabilization and selective conversion of many highly reactive, short-lived molecules and ions are often not possible through classical condensed phase synthetic methods.⁵ However, in the gas phase, reactive molecular fragments ions can be generated, for example, by collision activated dissociation (CAD).⁶ In the mass spectrometer, these highly reactive fragment ions are isolated in the gas phase and therefore unable to react until they are brought in contact with another reagent. The chemistry of reactive fragment ions has been studied in mass spectrometers for more than half a century.^{7,8} Only recently enhancements in ion currents made it possible to use this chemistry for the preparation of structured multilayered condensed phase materials, using ion soft-landing of mass selected molecular fragment ions.⁹⁻¹¹ Understanding the chemistry of molecular fragment ions constitutes the basis for their preparative use in ion soft-landing and may enable new insights into the role of highly reactive intermediates in classical synthetic reactions.

Closo-dodecaborate anions $[\text{B}_{12}\text{X}_{12}]^{2-}$ (X=halogen, CN) and their derivatives (e.g. carba-*closo*-dodecaborate anions $[\text{HCB}_{11}\text{X}_{11}]^-$) are known for their exceptional electronic and structural stability.¹² Cleavage of a highly stable B-X bonds results in fragments ions of exceptional reactivity. Heterolytic cleavage of one B-X bond in a *closo*- $[\text{B}_{12}\text{X}_{12}]^{2-}$ ion yields the fragment $[\text{B}_{12}\text{X}_{11}]^-$ (pathway a, see **Figure 5.1**), which spontaneously binds to noble gases and saturated alkanes.¹³ The free boron binding site within this singly charged anion is exceptionally

electrophilic, although the overall ion is negatively charged. Exploring the special binding properties of “electrophilic anions” is an emerging field of research. In contrast to the even electron ion $[\text{B}_{12}\text{X}_{11}]^-$, much less is known about the reactivity of radical fragments. $[\text{B}_{12}\text{X}_{12}]^{\bullet-}$ radical anions, formed by single electron oxidation (pathway b, see **Figure 5.1**), are known to be very stable and have been investigated in both gas and condensed phases.¹⁴ The unpaired electron in $[\text{B}_{12}\text{X}_{12}]^{\bullet-}$ is strongly delocalized. In contrast, if a radical substituent X^{\bullet} is abstracted, a free boron binding site in the radical dianion $[\text{B}_{12}\text{X}_{11}]^{2-\bullet}$ forms (pathway c). The radical is found to be localized on the vacant boron atom and high reactivity is expected. Electronically stable, localized radicals in small doubly charged anions are rare and usually prone to autodetachment in the gas phase. Previous studies observed that the ion $[\text{B}_{12}\text{I}_{11}]^{2-\bullet}$ is electronically stable (resistant against electron autodetachment), but very reactive and binds spontaneously with molecular oxygen in mass spectrometric experiments.¹⁵ This reactivity has often been observed for radical cations but remains rare for anions. The goal of this study is to characterize radicals localized on the vertex of an anionic boron icosahedra (localized at a vacant boron atom) and to understand which parameters influence their chemical reactivity. The gas-phase reactivity of $[\text{B}_{12}\text{I}_{11}]^{2-\bullet}$ towards allyl iodide and di-*tert*-butyl nitroxide (DTBN) was explored. Furthermore, to understand the influence of the localized radical binding site, the gas-phase reactivity of two singly charged derivatives, *closo*-dodecaborate anion $[\text{HCB}_{11}\text{I}_{10}]^{\bullet-}$ and carba-*closo*-dodecaborate anion $[\text{CB}_{11}\text{I}_{11}]^{\bullet-}$, towards oxygen, allyl iodide were studied and compared. The goal of this study is to characterize radicals localized on the vertex of an anionic boron icosahedra (localized at a vacant boron atom) and to understand which parameters influence their chemical reactivity.

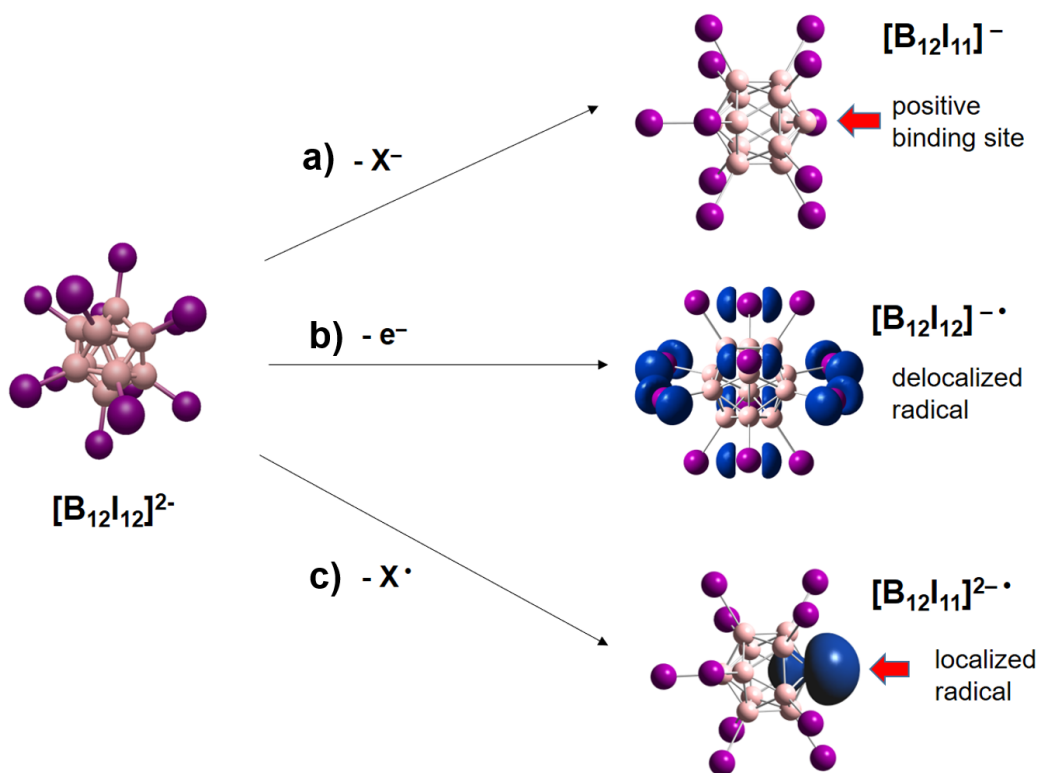


Figure 5.1 (a) Single step fragmentation of $[\text{B}_{12}\text{X}_{12}]^{2-}$ (on the example of $\text{X}=\text{I}$) in which the ion loses a I^- and forms $[\text{B}_{12}\text{I}_{11}]^-$. This pathway can be observable via CAD. (b) Pathway B requires the presence of a strong oxidizer to form the delocalized radical $[\text{B}_{12}\text{I}_{12}]^{2\bullet}$.¹³ (c) Single step fragmentation of $[\text{B}_{12}\text{I}_{12}]^{2-}$ in which the ion loses a I^\bullet and forms $[\text{B}_{12}\text{I}_{11}]^{2\bullet\bullet}$. This pathway can be observable via CAD. Pink circles represent boron atoms. Purple circles represent iodine atoms. Blue shapes represent spin density.

5.2 Results and discussion

As mentioned earlier, the ion $[\text{B}_{12}\text{I}_{11}]^{2\bullet\bullet}$ binds spontaneously with molecular oxygen in mass spectrometric experiments which has often been observed for radical cations but remains rare for anions. To characterize the electrophilic nature of $[\text{B}_{12}\text{I}_{11}]^{2\bullet\bullet}$, the gas-phase reactivity of $[\text{B}_{12}\text{I}_{11}]^{2\bullet\bullet}$ towards allyl iodide was explored first. Allyl iodide was chosen as the reagent for this study due to its high tendency to react with electrophilic radicals which were observed previously.¹⁷ Furthermore, to gain more insight on the influence of the localized radical binding site on electrophilicity of the radical ion, boron binding site radical anion $[\text{HCB}_{11}\text{I}_{10}]^\bullet$ and carbon

binding site radical anion $[\text{CB}_{11}\text{I}_{11}]^{\bullet-}$, towards allyl iodide and the residual O_2 in the ion trap were studied. The experimental results of boron binding site radical anion $[\text{HCB}_{11}\text{I}_{10}]^{\bullet-}$ with carbon binding site radical anion $[\text{CB}_{11}\text{I}_{11}]^{\bullet-}$ was compared with the computational results provided by collaboration partners from Leipzig University. Lastly, the experimental results of $[\text{B}_{12}\text{I}_{11}]^{2-\bullet}$ and $[\text{HCB}_{11}\text{I}_{10}]^{\bullet-}$ with DTBN were explored.

5.2.1 Reactions of $[\text{B}_{12}\text{I}_{11}]^{2-\bullet}$ with allyl iodide

The neutral reagent, allyl iodide reacts with radical ions through two competing pathways.¹⁷ The first reaction pathway is binding via the nucleophilic double bond on the allyl iodide with the radical ion which forms a C_3H_5 abstraction adduct. Previous studies have shown that the formation of C_3H_5 abstraction adduct is the preferred pathway for electrophilic cationic radicals.¹⁷ The second reaction pathway is though radical ions abstracting iodine located on the end of the neutral reagent allyl iodide. **Figure 5.2** shows a reaction mass spectrum of $[\text{B}_{12}\text{I}_{11}]^{2-\bullet}$ with allyl iodide. Pathways forming C_3H_5 and iodine abstraction adduct were both observed in the reaction mass spectrum. However, the formation of the C_3H_5 abstraction adduct is more dominant compared to the formation iodine abstraction adduct based on the relative abundances of the products shown in **Figure 5.2** Both reaction of $[\text{B}_{12}\text{I}_{11}]^{2-\bullet}$ with dioxygen and neutral reagent allyl iodide showed the behaviors that resembles to that of radical cations which demonstrates the electrophilicity of $[\text{B}_{12}\text{I}_{11}]^{2-\bullet}$ despite of its overall negative charge.

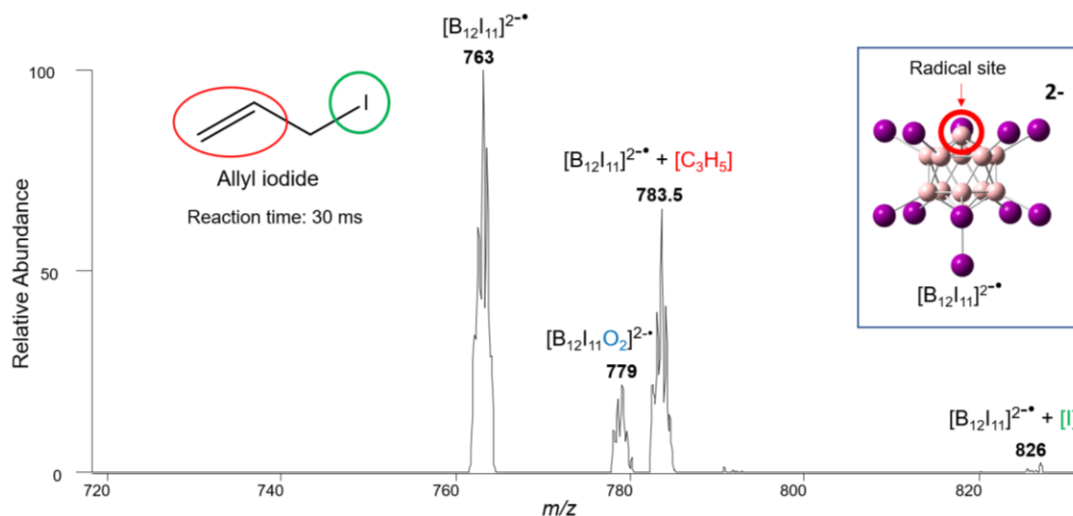


Figure 5.2 MS/MS spectrum measured after 30 ms reaction of $[B_{12}I_{11}]^{2-\bullet}$ with allyl iodide, indicating that a C_3H_5 abstraction adduct with a m/z value of 783.5 was formed in high abundance. Iodine abstraction adduct with a m/z value of 826 and O_2 adduct with a m/z value of 779 was also observed in lower abundances compared to the C_3H_5 abstraction adduct.

5.2.2 Reactions of $[HCB_{11}I_{10}]^{\bullet-}$ and $[CB_{11}I_{11}]^{\bullet-}$ with O_2 and allyl iodide

To gain more insight on the influence of the localized radical binding site on reactivity toward O_2 and allyl iodide, a boron and a carbon as the element at the free radical binding site of singly charged dodecaborates were compared along with the NPA results provided by collaboration partners (see method section).

To ensure the comparison of the two radical binding sites are under very similar structural conditions, the Finze group from University of Würzburg synthesized carborates that specifically produced radical binding site at defined positions of the cluster when subjected to CAD in the ion trap. To produce the free boron radical binding site in para position to the carbon, the carborate, para- $[HCB_{11}I_{10}-C_4H_9]^{\bullet-}$ was synthesized and subjected to CAD cleaving off a $[C_4H_9]^{\bullet}$ neutral radical. To generate a vacant radical binding site on the carbon, synthesized $[I-Hg-CB_{11}I_{11}]^{\bullet-}$ was subjected to CAD and fragmented via the loss of the neutral molecule $[HgI]^{\bullet}$. Comparing the two

radical anions in the **Figure 5.3**, $[\text{HCB}_{11}\text{I}_{10}]^{\bullet-}$ (vacant radical binding site on the boron atom) and $[\text{CB}_{11}\text{I}_{11}]^{\bullet-}$ (vacant radical binding site on the carbon atom) both have the radical binding site situated at the free edge of the icosahedral which is surrounded by five iodine atoms. Therefore, steric factors are expected to play a minor role.

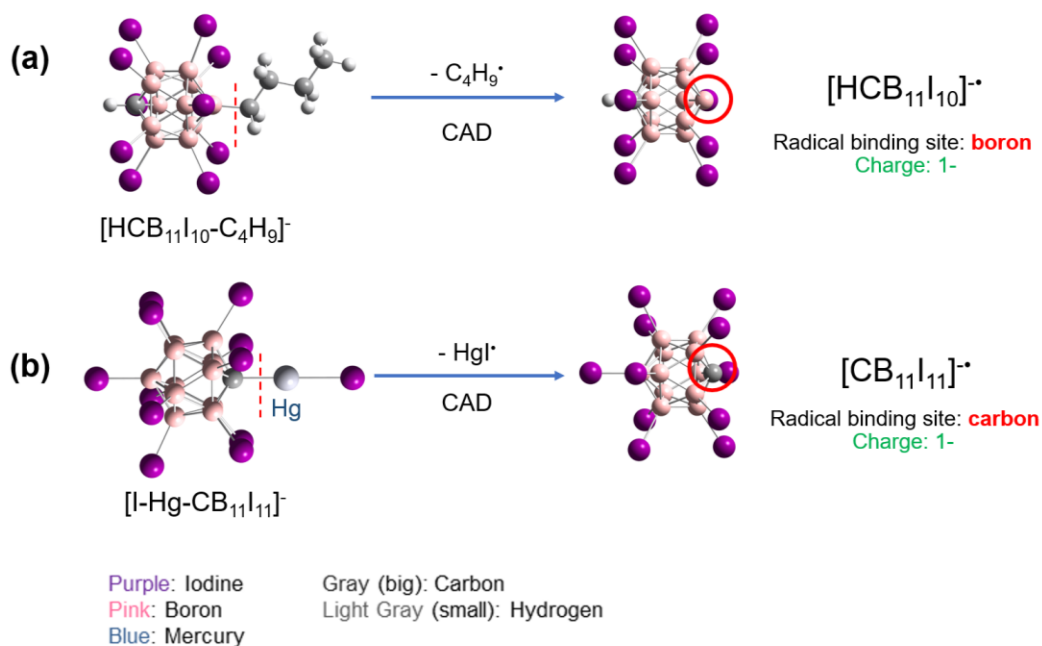


Figure 5.3 (a) Generation of boron free radical binding site carborate $[\text{HCB}_{11}\text{I}_{10}]^{\bullet-}$ from precursor ion para- $[\text{HCB}_{11}\text{I}_{10}\text{-C}_4\text{H}_9]^-$. (b) Generation of carbon free radical binding site carborate $[\text{HCB}_{11}\text{I}_{10}]^{\bullet-}$ from precursor ion $[\text{I-Hg-CB}_{11}\text{I}_{11}]^-$.

The computational results provided by collaboration partners (see experimental section) showed that the free boron binding site on $[\text{HCB}_{11}\text{I}_{10}]^{\bullet-}$ has a natural population analysis (NPA) charge of +0.182, while the negative carbon binding site on $[\text{CB}_{11}\text{I}_{11}]^{\bullet-}$ has a NPA charge of -0.581. This suggested that the localized radical binding site on $[\text{HCB}_{11}\text{I}_{10}]^{\bullet-}$ possesses an electrophilic nature while the localized radical binding site on $[\text{CB}_{11}\text{I}_{11}]^{\bullet-}$ possesses a nucleophilic nature. In **Figure 5.4**, we observed that the positive boron binding site reacted faster than the negative carbon binding site qualitatively by comparing the relative abundances of the O_2 adduct of $[\text{HCB}_{11}\text{I}_{10}]^{\bullet-}$

and $[\text{CB}_{11}\text{I}_{11}]^{\cdot-}$ under the same reaction period and using the relative abundance of the radical precursor ions $[\text{HCB}_{11}\text{I}_{10}]^{\cdot-}$ and $[\text{CB}_{11}\text{I}_{11}]^{\cdot-}$ as a reference (relative abundance :100%).

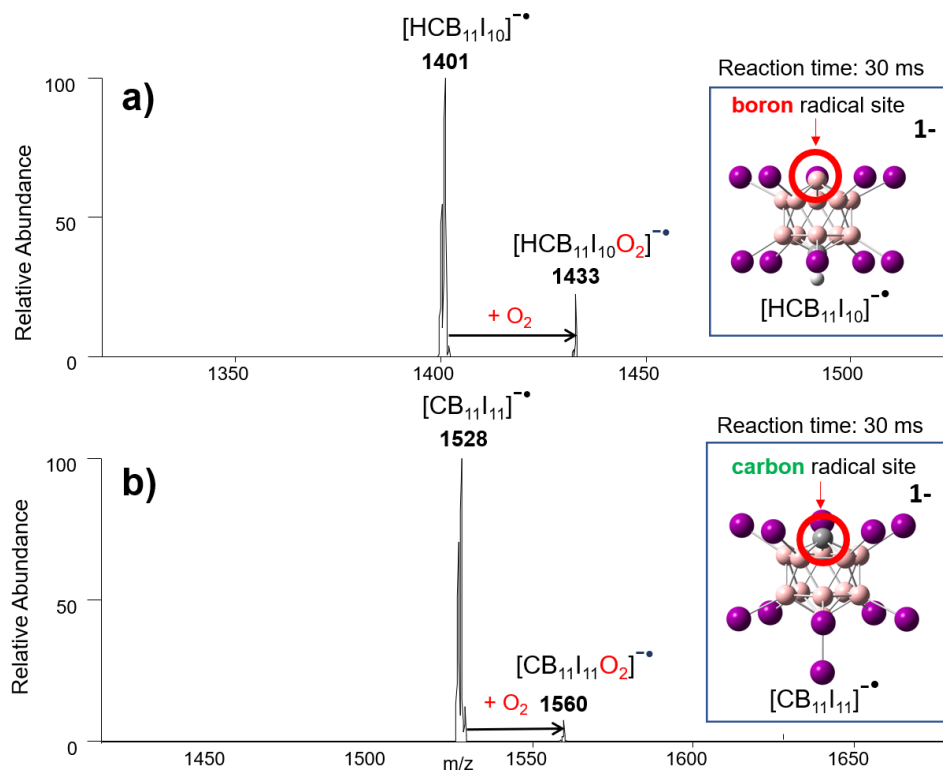


Figure 5.4 (a) MS/MS spectrum measured after 30 ms reaction of $[\text{HCB}_{11}\text{I}_{10}]^{\cdot-}$ with O_2 , indicating that an O_2 adduct with a m/z value of 1433 was formed. (b) MS/MS spectrum measured after 30 ms reaction of $[\text{CB}_{11}\text{I}_{11}]^{\cdot-}$ with O_2 , indicating that an O_2 adduct with a m/z value of 1560 was formed.

The reactivity of $[\text{HCB}_{11}\text{I}_{10}]^{\cdot-}$ and $[\text{CB}_{11}\text{I}_{11}]^{\cdot-}$ towards allyl iodide was compared. **Figure 5.5** shows the reaction mass spectra of $[\text{HCB}_{11}\text{I}_{10}]^{\cdot-}$ and $[\text{CB}_{11}\text{I}_{11}]^{\cdot-}$ with allyl iodide. In **Figure 5.5a**, $[\text{HCB}_{11}\text{I}_{10}]^{\cdot-}$ showed a preference of the formation of a C_3H_5 abstraction adduct, based on the higher abundance of C_3H_5 abstraction adduct observed compared to that of other product ions. The formation of an iodine abstraction product ion is also observed but in low abundance. This resembles the reactivity of $[\text{B}_{12}\text{I}_{11}]^{2\cdot-}$ with allyl iodide since $[\text{HCB}_{11}\text{I}_{10}]^{\cdot-}$ and $[\text{B}_{12}\text{I}_{11}]^{2\cdot-}$ are both boron binding site radical anions. In **Figure 5.5b**, the ion-molecule reaction of $[\text{CB}_{11}\text{I}_{11}]^{\cdot-}$ with

allyl iodide shows also the product ion formed by C_3H_5 abstraction and iodine abstraction. However, a clear preference of C_3H_5 abstraction as typical for electrophilic radicals is not observed. Also, by comparing the relative abundances of the C_3H_5 abstraction product ion of the two carborates with that of the precursor ion under same conditions (relative abundances of both precursor ions are 100% and same reaction period), the product ions formed with $[\text{HCB}_{11}\text{I}_{10}]^{\bullet}$ are significant more abundant. This points to a generally higher electrophilicity of the $[\text{HCB}_{11}\text{I}_{10}]^{\bullet}$ radical. Even though the carborates studied were both singly charged radical anion, the positive boron free binding site of $[\text{HCB}_{11}\text{I}_{10}]^{\bullet}$ were still capable of showing electrophilic characteristics.

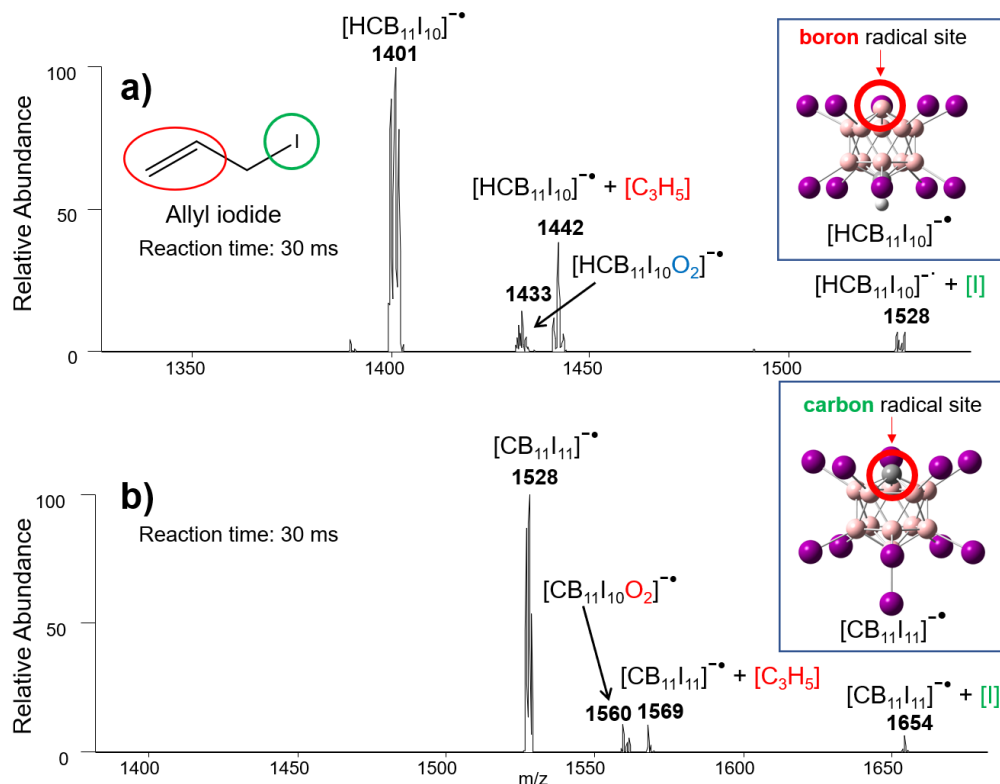


Figure 5.5 (a) MS/MS spectrum measured after 30 ms reaction of $[\text{HCB}_{11}\text{I}_{10}]^{\bullet-}$ with allyl iodide, indicating that a C_3H_5 abstraction adduct with a m/z value of 1442 was formed in high abundance. Iodine abstraction adduct with a m/z value of 1528 and O_2 adduct with a m/z value of 1433 was also observed in lower abundances compared to the C_3H_5 abstraction adduct. (b) MS/MS spectrum measured after 30 ms reaction of $[\text{CB}_{11}\text{I}_{11}]^{\bullet-}$ with allyl iodide, indicating that a C_3H_5 abstraction adduct with a m/z value of 1569, iodine abstraction adduct with a m/z value of 1654 and O_2 adduct with a m/z value of 1560 were formed in similar abundances.

5.2.3 Reactions of $[\text{B}_{12}\text{I}_{11}]^{2-\bullet}$ and $[\text{HCB}_{11}\text{I}_{10}]^{\bullet-}$ with di-*tert*-butyl nitroxide

Previous reactivity studies of radicals with di-*tert*-butyl nitroxide (DTBN) in both gas phase and solution have shown that a H abstraction reaction predominates when electrophilic radicals react with DTBN.^{18,19} The reactivity of two radical anions with a free boron binding site, $[\text{B}_{12}\text{I}_{11}]^{2-\bullet}$ and $[\text{HCB}_{11}\text{I}_{10}]^{\bullet-}$, towards DTBN was explored to evaluate their electrophilicity. **Figure 5.6** shows the reaction mass spectra of $[\text{B}_{12}\text{I}_{11}]^{2-\bullet}$ and $[\text{HCB}_{11}\text{I}_{10}]^{\bullet-}$ with DTBN. Since $[\text{B}_{12}\text{I}_{11}]^{2-\bullet}$ is a doubly charged ion, in the reaction mass spectra (**Figure 5.6a**), the H abstraction product ion

will have a m/z value that is a 0.5 Da addition to that of the isolated radical ion. Therefore, to avoid isolation of isotopic radical ions that are isobaric to the H abstraction product ion (m/z value of 763.5), the mass spectrum of $[B_{12}I_{11}]^{2-\bullet}$ with DTBN (**Figure 5.6a**) was collected using an isolation width of 0.8 m/z units ($\pm 0.4 m/z$) to isolate $[B_{12}I_{11}]^{2-\bullet}$ (m/z value of 763.0). The isolation width of 0.8 m/z units ($\pm 0.4 m/z$) was also applied for the reaction mass spectra of $[HCB_{11}I_{10}]^{-\bullet}$ with DTBN (**Figure 5.6b**). In both mass spectra, the H abstraction product ion was observed in high abundance compared to the other product ions which classifies both radical anions with a free boron binding site, $[B_{12}I_{11}]^{2-\bullet}$ and $[HCB_{11}I_{10}]^{-\bullet}$ as electrophilic radicals.

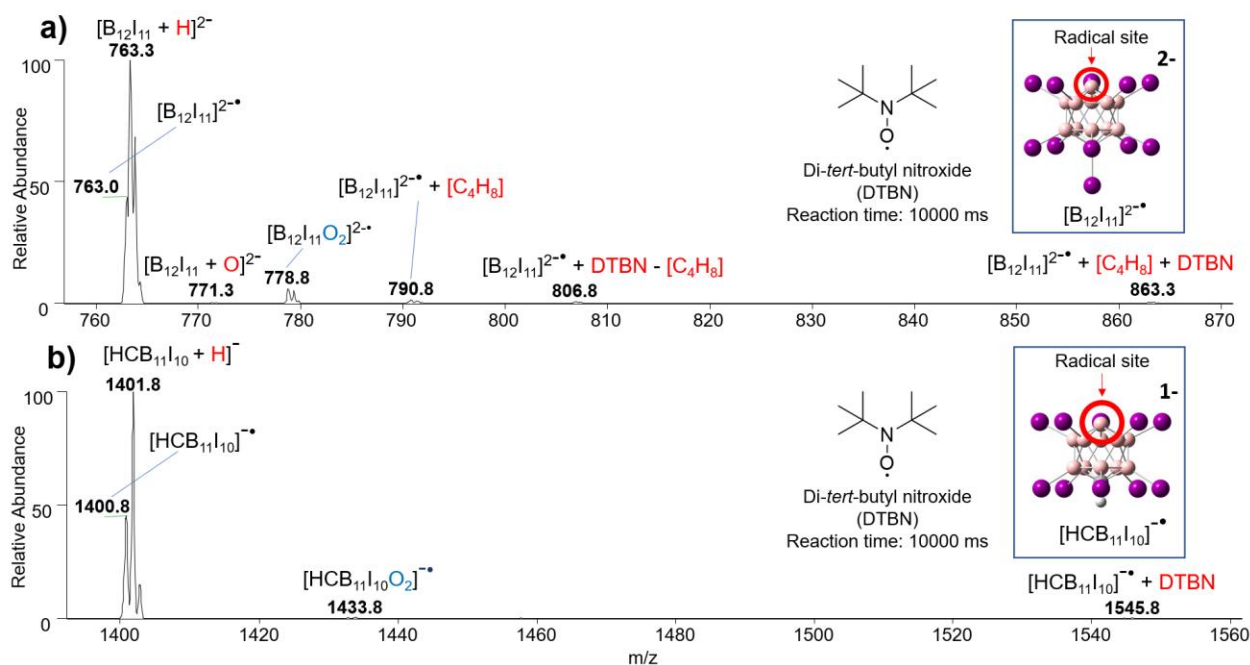


Figure 5.6 (a) MS/MS/MS spectrum measured after 10000 ms reaction of $[B_{12}I_{11}]^{2-\bullet}$ with DTBN, indicating that a H abstraction adduct with a m/z value of 763.3 was formed in high abundance. O abstraction adduct ($m/z=771.3$), O_2 adduct ($m/z=778.8$), C_4H_8 adduct ($m/z=790.8$), adduct followed by a loss of C_4H_8 moiety ($m/z=806.8$) and adduct with an addition of C_4H_8 ($m/z=863.3$) were observed in lower abundances compared to the H abstraction adduct. (b) MS/MS/MS spectrum measured after 10000 ms reaction of $[HCB_{11}I_{10}]^{-\bullet}$ with DTBN, indicating that a H abstraction adduct with a m/z value of 1401.8 was formed in high abundance. O_2 adduct ($m/z=1433.8$) and adduct ($m/z=1545.8$), were observed in lower abundances compared to the H abstraction adduct.

5.2.4 Comparing the reactivity of $[B_{12}I_{11}]^{2\bullet}$ and $[HCB_{11}I_{10}]^{\bullet}$ towards allyl iodide

A comparison between the reaction mass spectra of the vacant radical boron binding site of the doubly charged anion $[B_{12}I_{11}]^{2\bullet}$ (**Figure 5.2**) and the singly charged anion $[HCB_{11}I_{10}]^{\bullet}$ (**Figure 5.4a and 5.5a**) shows strong qualitative similarities towards O_2 and allyl iodide. Computational results provided by collaboration partners showed that the NPA charge for the vacant boron of $[B_{12}I_{11}]^{2\bullet}$ is +0.065 which is slightly less positive than that of $[HCB_{11}I_{10}]^{\bullet}$ (NPA: +0.182). This computational result suggested that both of the boron radical binding sites adopted electrophilic nature, regarding the overall negative charge for both clusters. However, the reaction mass spectra of $[B_{12}I_{11}]^{2\bullet}$ and $[HCB_{11}I_{10}]^{\bullet}$ showed that $[B_{12}I_{11}]^{2\bullet}$, although slightly less positive, reacted faster than the carborate $[HCB_{11}I_{10}]^{\bullet}$ with allyl iodide to form the C_3H_5 abstraction adduct (**Figure 5.7**). Although both boron sites of $[B_{12}I_{11}]^{2\bullet}$ and $[HCB_{11}I_{10}]^{\bullet}$ are chemically similar, the difference in the physical charge state is affecting the kinetics of ion molecule reactions. $[B_{12}I_{11}]^{2\bullet}$ has an overall charge of 2-, while $[HCB_{11}I_{10}]^{\bullet}$ has an overall charge of 1-. The possible explanation for their kinetic differences in the reaction with allyl iodide is taking ion induced dipole interaction into account. Ion induced dipole interaction between a doubly charged ion and the neutral reagent is larger than for a monoanion. This phenomenon increases the collision rate and overcompensates the slightly smaller positive charge on the site of the doubly charged ion $[B_{12}I_{11}]^{2\bullet}$ resulting in a faster reaction kinetics.

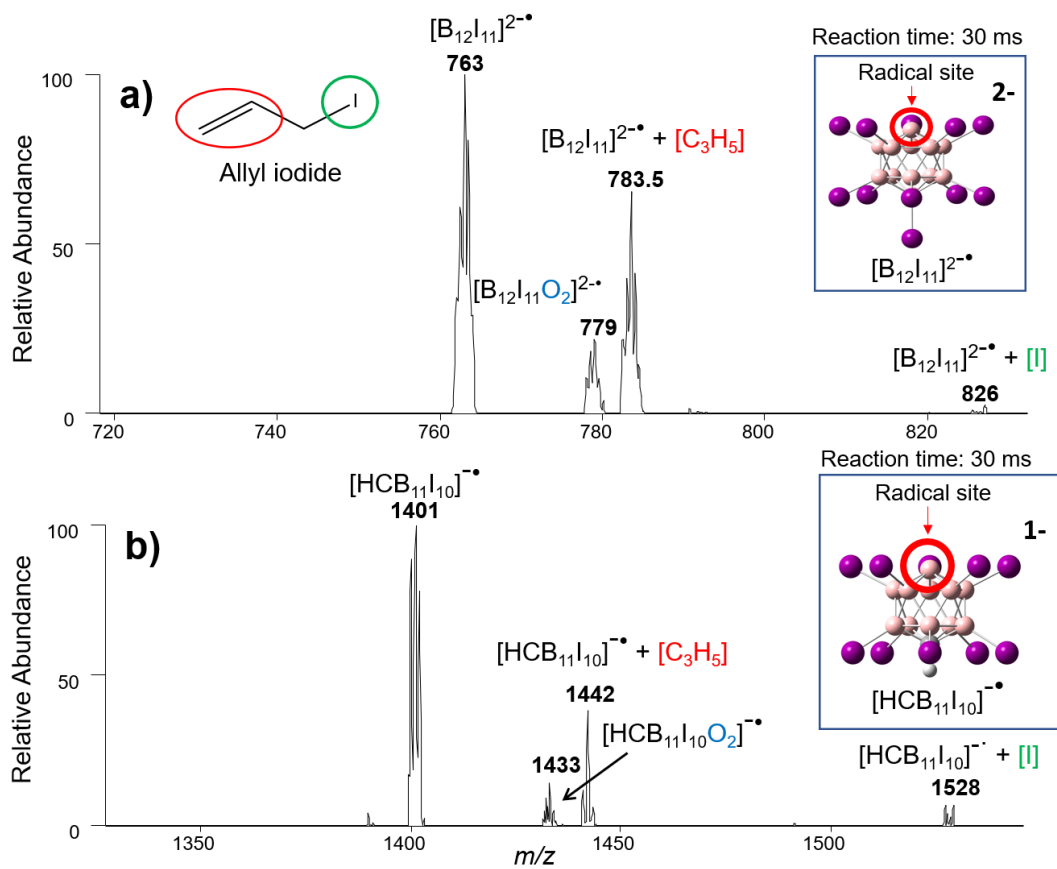


Figure 5.7 (a) MS/MS spectrum measured after 30 ms reaction of $[B_{12}I_{11}]^{2-\bullet}$ with allyl iodide, indicating that a C_3H_5 abstraction adduct with a m/z value of 783.5 was formed in high abundance. Iodine abstraction adduct with a m/z value of 826 and O_2 adduct with a m/z value of 779 was also observed in lower abundances compared to the C_3H_5 abstraction adduct. (b) MS/MS spectrum measured after 30 ms reaction of $[HCB_{11}I_{10}]^{\bullet-}$ with allyl iodide, indicating that a C_3H_5 abstraction adduct with a m/z value of 1442, iodine abstraction adduct with a m/z value of 1528 and O_2 adduct with a m/z value of 1433 were formed in similar abundances.

5.3 Experimental

5.3.1 ESI MS/MS method

All mass spectrometry experiments were performed using a Thermo Scientific LTQ linear quadrupole ion trap (LQIT) equipped with an electrospray ionization (ESI) source operated in negative mode. The *closo*-dodecaborate anions and carba-*closo*-dodecaborate anions sample solutions were prepared in methanol at analyte concentrations of roughly 1 mg/mL and delivered

at a flow rate of 15 $\mu\text{L}/\text{min}$ through a syringe pump into the ESI source. Nitrogen gas was used as the sheath and auxiliary gas with flow rates of 30 and 10 arbitrary units, respectively. The capillary temperature was set to 275°C. The ions generated upon ESI were transferred into the ion trap via the ion optics. The voltages applied to the ion optics were optimized for each protonated analyte via the tune feature of the LTQ Tune Plus interface. The analyte ions were isolated with a window of 2 m/z units and subjected to CAD (collision energy 80 arbitrary units) using helium as collision gas to obtain desired radical anions.

5.3.2 Ion molecule reactions with O₂

The desired radical anions were stored in the ion trap for 10-100 ms to react with the residual O₂ present in the ion trap. To ensure the amount of O₂ are roughly the same in the ion trap, O₂ binding experiments between different radical anions were done on the same day.

5.3.3 Ion-molecule reaction with allyl iodide

Neutral reagent allyl iodide was purchased from Sigma Aldrich and used as is. Allyl iodide is introduced directly into the ion trap through an external reagent mixing manifold. Allyl iodide was injected via a syringe pump at a flow rate of 5 $\mu\text{L}/\text{h}$. With the boiling point of 102 °C, allyl iodide was vaporized by heating the surrounding helium gas line to around 110 °C. The neutral reagents were diluted and delivered into the ion trap through a helium buffer gas line and introducing a controlled amount of helium as a carrier gas. The desired radical ion, generated as described previously, was isolated and allowed to react with neutral reagents in the ion trap up to 10000 ms. The reaction product ion was then isolated and subjected to CAD for additional structural information.

5.3.4 Computational studies

Computational studies were provided by a collaboration partner, Mark Rohdenburg. Experimental details for the computational studies and Natural Population Analysis (NPA) can be found in previous published articles from our collaboration partners at Leipzig University.^{14,16}

5.4 Conclusion

The *closo*-dodecaborate ion $[\text{B}_{12}\text{I}_{12}]^{2-}$ has a highly stable icosahedral structure. A homolytic cleavage of one B-I bond in this $[\text{B}_{12}\text{I}_{12}]^{2-}$ ion in the gas phase results in the formation of the radical dianion $[\text{B}_{12}\text{I}_{11}]^{2-\bullet}$. $[\text{B}_{12}\text{I}_{11}]^{2-\bullet}$ reacted with residual O_2 gas in a LQIT MS— a reaction typically observed for radical cations. The gas-phase reactivity of $[\text{B}_{12}\text{I}_{11}]^{2-\bullet}$ toward allyl iodide and DTBN, has been studied in LQIT MS to characterize the chemical nature of this atypical radical dianion containing a localized radical site in the icosahedral boron core. Remarkably, $[\text{B}_{12}\text{I}_{11}]^{2-\bullet}$ reacted efficiently with electron-rich neutral reagents, such as allyl iodide, that usually react rapidly with electrophilic cations. In addition, $[\text{B}_{12}\text{I}_{11}]^{2-\bullet}$ reacted with DTBN to predominately form a H abstraction product ion, that is usually observed for electrophilic radicals. Furthermore, the reactivity of two singly charged carborate radicals, $[\text{HCB}_{11}\text{I}_{10}]^\bullet$ (with the radical site localized on a boron atom) and $[\text{CB}_{11}\text{I}_{11}]^\bullet$ (with the radical site localized on a carbon atom) were examined. Product ions were compared qualitatively and have shown consistently that the radical anion with the binding site on boron has a greater reactivity than that with the binding site on carbon. Natural population analysis revealed that the boron binding site carries a positive charge in both $[\text{HCB}_{11}\text{I}_{10}]^\bullet$ and $[\text{B}_{12}\text{I}_{11}]^{2-\bullet}$, while less reactive carbon binding site in $[\text{CB}_{11}\text{I}_{11}]^\bullet$ has a negative charge. This finding indicates that the radical anions with vacant boron atoms investigated here may be classified as electrophilic radicals, although they are anions.

5.5 References

- (1) Paunović, V.; Hemberger, P.; Bodi, A.; López, N.; Pérez-Ramírez, J. Evidence of Radical Chemistry in Catalytic Methane Oxybromination. *Nat. Catal.* **2018**, *1* (5), 363–370. <https://doi.org/10.1038/s41929-018-0071-z>.
- (2) Wang, Y.; Cao, H.; Chen, L.; Chen, C.; Duan, X.; Xie, Y.; Song, W.; Sun, H.; Wang, S. Tailored Synthesis of Active Reduced Graphene Oxides from Waste Graphite: Structural Defects and Pollutant-Dependent Reactive Radicals in Aqueous Organics Decontamination. *Appl. Catal. B Environ.* **2018**, *229*, 71–80. <https://doi.org/10.1016/j.apcatb.2018.02.010>.
- (3) Huang, C. P.; Dong, C.; Tang, Z. Advanced Chemical Oxidation: Its Present Role and Potential Future in Hazardous Waste Treatment. *Waste Manag.* **1993**, *13* (5–7), 361–377. [https://doi.org/10.1016/0956-053X\(93\)90070-D](https://doi.org/10.1016/0956-053X(93)90070-D).
- (4) Kaupp, G.; Schmeyers, J.; Boy, J. Waste-Free Solid-State Syntheses with Quantitative Yield. *Chemosphere* **2001**, *43* (1), 55–61. [https://doi.org/10.1016/S0045-6535\(00\)00324-6](https://doi.org/10.1016/S0045-6535(00)00324-6).
- (5) Werst, D. W.; Trifunac, A. D. Study of Radical Ions in the Condensed Phase by Fluorescence-Detected Magnetic Resonance. *J. Phys. Chem.* **1991**, *95* (9), 3466–3477. <https://doi.org/10.1021/j100162a007>.
- (6) Barlow, C. K.; Wright, A.; Easton, C. J.; O’Hair, R. A. J. Gas-Phase Ion-Molecule Reactions Using Regioselectively Generated Radical Cations to Model Oxidative Damage and Probe Radical Sites in Peptides. *Org. Biomol. Chem.* **2011**, *9* (10), 3733–3745. <https://doi.org/10.1039/c0ob01245a>.
- (7) Henis, J. M. S. Ion Cyclotron Resonance Study of Ion-Molecule Reactions in Methanol. *J. Am. Chem. Soc.* **1968**, *90* (4), 844–851. <https://doi.org/10.1021/ja01006a003>.
- (8) Abramson, F. P.; Futrell, J. H. Mass-Spectrometric Investigation of Ion-Molecule Reactions in Cyclohexane. *J. Phys. Chem.* **1967**, *71* (12), 3791–3796. <https://doi.org/10.1021/j100871a012>.
- (9) Warneke, J.; Mayer, M.; Rohdenburg, M.; Ma, X.; Liu, J. K. Y.; Grellmann, M.; Debnath, S.; Azov, V. A.; Apra, E.; Young, R. P.; Jenne, C.; Johnson, G. E.; Kenttämä, H. I.; Asmis, K. R.; Laskin, J. Direct Functionalization of C–H Bonds by Electrophilic Anions. *Proc. Natl. Acad. Sci.* **2020**, *117* (38), 23374–23379. <https://doi.org/10.1073/pnas.2004432117>.
- (10) Yang, F.; Behrend, K. A.; Knorke, H.; Rohdenburg, M.; Charvat, A.; Jenne, C.; Abel, B.; Warneke, J. Anion–Anion Chemistry with Mass-Selected Molecular Fragments on Surfaces. *Angew. Chem. Int. Ed.* **2021**, *60* (47), 24910–24914. <https://doi.org/10.1002/anie.202109249>.
- (11) Samayoa-Oviedo, H. Y.; Behrend, K.-A.; Kawa, S.; Knorke, H.; Su, P.; Belov, M. E.; Anderson, G.; Warneke, J.; Laskin, J. Design and Performance of a Soft-Landing Instrument for Fragment Ion Deposition. *Anal. Chem.* **2021**, *93* (43), 14489–14496. <https://doi.org/10.1021/acs.analchem.1c03009>.

- (12) Warneke, J.; Hou, G.-L.; Aprà, E.; Jenne, C.; Yang, Z.; Qin, Z.; Kowalski, K.; Wang, X.-B.; Xantheas, S. S. Electronic Structure and Stability of $[B_{12}X_{12}]^{2-}$ (X = F–At): A Combined Photoelectron Spectroscopic and Theoretical Study. *J. Am. Chem. Soc.* **2017**, *139* (41), 14749–14756. <https://doi.org/10.1021/jacs.7b08598>.
- (13) Rohdenburg, M.; Azov, V. A.; Warneke, J. New Perspectives in the Noble Gas Chemistry Opened by Electrophilic Anions. *Front. Chem.* **2020**, *8*, 580295. <https://doi.org/10.3389/fchem.2020.580295>.
- (14) Boere, R. T.; Derendorf, J.; Jenne, C.; Kacprzak, S.; Keßler, M.; Riebau, R.; Riedel, S.; Roemmele, T. L.; Ruhle, M.; Scherer, H.; Vent-Schmidt, T.; Warneke, J.; Weber, S. On the Oxidation of the Three-Dimensional Aromatics $[B_{12}X_{12}]^{2-}$ (X=F, Cl, Br, I). *Chem Eur. J.* **2014**, *20*, 4447–4459. <https://doi.org/10.1002/chem.201304405>.
- (15) Warneke, J.; Rohdenburg, M.; Liu, J. K. Y.; Johnson, E.; Ma, X.; Kumar, R.; Su, P.; Aprà, E.; Wang, X.-B.; Jenne, C.; Finze, M.; Kenttämä, H. I.; Laskin, J. Gas Phase Fragmentation of Adducts between Dioxygen and Closo-Borate Radical Anions. *Int. J. Mass Spectrom.* **2019**, *436*, 71–78. <https://doi.org/10.1016/j.ijms.2018.11.005>.
- (16) Mayer, M.; van Lessen, V.; Rohdenburg, M.; Hou, G.-L.; Yang, Z.; Exner, R. M.; Aprà, E.; Azov, V. A.; Grabowsky, S.; Xantheas, S. S.; Asmis, K. R.; Wang, X.-B.; Jenne, C.; Warneke, J. Rational Design of an Argon-Binding Superelectrophilic Anion. *Proc. Natl. Acad. Sci.* **2019**, *116* (17), 8167–8172. <https://doi.org/10.1073/pnas.1820812116>.
- (17) Petzold, C. J.; Nelson, E. D.; Lardin, H. A.; Kenttämä, H. I. Charge-Site Effects on the Radical Reactivity of Distonic Ions. *J. Phys. Chem. A* **2002**, *106* (42), 9767–9775. <https://doi.org/10.1021/jp025521i>.
- (18) Heidbrink, J. L.; Amegayibor, F. S.; Kenttämä, H. I. Gas-Phase Radical–Radical Recombination Reactions of Nitroxides with Substituted Phenyl Radicals. *Int J Chem Kinet* **2004**, *36*, 216–229. <https://doi.org/10.1002/kin.10189>.
- (19) Singh, H.; Tedder, J. M. Interconversion of Carbocations, Free Radicals and Carbanions in Nitroxide Solutions. *J. Chem. Soc. Chem. Commun.* **1981**, No. 3, 70-71. <https://doi.org/10.1039/c39810000070>.

LIST OF PUBLICATIONS

- (1) Fine, J.; Kuan-Yu Liu, J.; Beck, A.; Alzarieni, K. Z.; Ma, X.; Boulos, V. M.; Kenttämä, H. I.; Chopra, G. Graph-Based Machine Learning Interprets and Predicts Diagnostic Isomer-Selective Ion–Molecule Reactions in Tandem Mass Spectrometry. *Chem. Sci.* **2020**, *11* (43), 11849–11858. <https://doi.org/10.1039/D0SC02530E>.
- (2) Liu, J. K.; Niyonsaba, E.; Alzarieni, K. Z.; Boulos, V. M.; Yerabolu, R.; Kenttämä, H. I. Determination of the Compound Class and Functional Groups in Protonated Analytes via Diagnostic Gas-phase Ion-molecule Reactions. *Mass Spectrom. Rev.* **2021**, mas.21727: 1-17. <https://doi.org/10.1002/mas.21727>.
- (3) Niyonsaba, E., Easton, M., Liu, J.K.Y., Yu, Z., Sheng, H., Kong, J., Zhang, Z., Easterling, L., Milton, J. and Kenttämä, H.I., Identification of Protonated Primary Carbamates by Using Gas-Phase Ion-Molecule Reactions Followed by Collision-activated Dissociation in Tandem Mass Spectrometry Experiments, *Org. Process Res. Dev.* **2019**, *236*, 1159–1166. <https://doi.org/10.1021/acs.oprd.9b00080>
- (4) Warneke, J., Rohdenburg, M., Liu, J.K.Y., Johnson, E., Ma, X., Kumar, R., Su, P., Apra, E., Wang, X., Jenne, C., Finze, M., Kenttämä, H.I. and Laskin, J., Gas-Phase Fragmentation of Adducts of Dioxygen and closo-Borate Radical Anions, *Int. J. Mass Spectrom.* **2019**, *436*, 71–78. <https://doi.org/10.1016/j.ijms.2018.11.005>
- (5) Warneke, J., Mayer, M., Rohdenburg, M., Ma, X., Liu, J.K.Y., Grellmann, M., Debnath, S., Azov, V.A., Apra, E., Young, R.P., Jenne, C., Johnson, G.E., Kenttämä, H.I., Asmis, K. R. and Laskin, J., Direct Functionalization of C–H Bonds by Electrophilic Anions, *Proc. Natl. Acad. Sci. U.S.A.* **2020**, *117*, 23374–23379. <https://doi.org/10.1073/pnas.2004432117>